

Mechanical Characterization and Computational Modeling of Snap-cure Epoxy

by

Yu Zeng

A thesis
presented to the University Of Waterloo
in fulfilment of the
thesis requirement for the degree of
Master of Applied Science
in
Mechanical and Mechatronics Engineering

Waterloo, Ontario, Canada, 2020

© Yu Zeng 2020

AUTHOR'S DECLARATION

I hereby declare that I am the sole author of this thesis. This is a true copy of the thesis, including any required final revisions, as accepted by my examiners.

I understand that my thesis may be made electronically available to the public.

Abstract

Owing to their high specific mechanical properties and excellent energy absorption characteristics, high-performance carbon fiber-reinforced plastic (CFRP) composite materials are regarded as viable candidates for improving the fuel economy of petroleum-fueled passenger vehicles and increasing the driving range of electric vehicles through lightweighting. The recent development of snap curing epoxy resins, low-cost carbon fiber fabrics, and automated rapid processing technologies provides a promising opportunity to increase usage of CFRP materials in high-volume production vehicles. For these CFRP materials, characterizing the impact performance and strain rate dependent response, which is governed by the properties and local failure characteristics of the matrix material, is required for use in energy absorbing vehicle structures to protect occupants in the event of a crash.

The current study investigated and modeled the constitutive behaviour of a three-part snap-cure epoxy matrix material that was formulated for CFRP composites manufactured with rapid resin transfer molding processes. The deformation response of the epoxy under tensile, compressive, and shear loading conditions over a range of strain rates was assessed (i.e., 10^{-4} to 10^3 s^{-1}). The experimental results revealed that the tensile elastic modulus increased by 34% and the yield strength increased by 31% over the range of strain rates investigated. In contrast, the compressive elastic modulus was not sensitive to the change in strain rates; however, the compressive yield strength increased by 81%, demonstrating a strong dependence on strain rate. The pressure-dependent plastic deformation of the investigated epoxy was identified by a clear difference in yield strengths between compression and tension when the material was loaded at a similar rate, where the compressive yield strength was noticeably higher than the tensile yield strength. The tensile specimens exhibited moderate ductile deformation at quasi-static strain rates, while all the tensile specimens fractured in a brittle manner at all strain rates, determined through optical observations of the specimen fracture surfaces. The deformation of the compressive specimens exhibited higher strain to failure in comparison with the tensile specimens, where classical elastic, plastic flow, strain-softening, and strain re-hardening deformation stages were observed. The shear specimens demonstrated elastic deformation, plastic flow, and strain-softening deformation stages, which were similar to the deformation response in the tensile tests at the quasi-static strain rates. Due to the limitation of the shear specimen geometry and mode of failure, only quasi-static and low intermediate strain rate testing was undertaken for the current study.

Based on the material characterization results, a Johnson-Cook plasticity constitutive model was used to represent the mechanical response of the snap-cure epoxy material. The constitutive model parameters were calibrated to the measured experimental data and verified using single element simulations in a commercial

finite element code (Abaqus). The model was able to describe the deformation responses and the strain rate dependence of the studied epoxy material under tensile and shear loading conditions over a range of strain rates (quasi-static, intermediate, and high strain rates). However, the current constitutive model assumes symmetry in tension and compression, thus the model did not accurately represent the strain rate dependence in compression. The proposed constitutive material model parameters were validated by comparing the results of independent experiments on test specimens under complex stress conditions with that of a computational model that incorporated the calibrated constitutive model. Captured strain maps from the experiments revealed that the investigated constitutive model was able to describe the overall strain response and to locate the locations of critical stresses of the tested specimen. Overall, this study provides much needed mechanical characterization and constitutive model parameters for a snap-cure epoxy material. The results provide support for the development of a robust high-fidelity virtual multiscale-modeling framework aimed at predicting the performance of CFRP materials and energy-absorbing structures.

Acknowledgements

First, I would like to express my gratitude to Dr. John Montesano and Dr. Duane Cronin, my research supervisors, for their useful guidance and warm encouragement, which helped me all the time during my research and writing of this thesis. Even when the road got tough, they convincingly guided and encouraged me to be professional and do the right thing. Without their persistent help, the goal of this project would not have been realized.

I would also like to extend my thanks to all the group members in the Composites Research Group (CRG) and the Impact Mechanics and Material Characterization (IMMC) research groups, as well as technicians in the forming and crash lab at the University of Waterloo, for their support throughout my master's research. Especially thanks to Dr. Luis Trimino Rincon, Brock Watson, and Tom Gawel, for their helps in the lab.

With many thanks to the industrial sponsors (Honda R&D Americas, Hexion Inc., Zoltek Corporation, and LAVAL International) and Natural Science and Engineering Research Council of Canada (NSERC), for providing the funding and helping to the project, as well as Ontario Graduate Scholarship (OGS) to financially support my research work.

Last but not least, I would like to thank my wife and parents, for supporting me spiritually throughout my research and my life, as well as my lovely Benjamin and Chloe, who bring in happiness to help me walk through all challenges.

Table of Contents

| | |
|--|-----|
| List of Figures | ix |
| List of Tables | xiv |
| Chapter 1 Introduction | 1 |
| 1.1 Composite Materials in the Automotive Industry | 1 |
| 1.2 Research Objectives..... | 4 |
| 1.3 Thesis Outline | 5 |
| Chapter 2 Background and Literature Review..... | 6 |
| 2.1 Epoxy Materials | 6 |
| 2.1.1 Polymerization and Uncured Epoxy Resin Properties | 7 |
| 2.1.2 Curing Process for Epoxies..... | 11 |
| 2.1.3 Epoxy Additives..... | 14 |
| 2.1.4 Glass Transition Temperature (T_g) of Cured Epoxy..... | 15 |
| 2.1.5 Snap-Cure epoxy..... | 16 |
| 2.1.6 Mechanical Properties of Cured Epoxy | 17 |
| 2.2 Mechanical Characterization of Epoxy Materials under Multiple Loading Rates..... | 22 |
| 2.2.1 Mechanical Characterization of the Strain Rate Sensitivity of Epoxy Resins | 22 |
| 2.2.2 Characterization Techniques for Epoxy Materials across a Wide Range of Strain Rates..... | 24 |
| 2.2.3 Limitations of Previous Epoxy Characterization Studies | 30 |
| 2.3 Constitutive Models in Commercial FE Software | 31 |
| 2.3.1 Constitutive Models for Glassy Polymers..... | 33 |
| 2.3.2 Limitation of Developed Epoxy Constitutive Models | 37 |
| Chapter 3 Experimental Methods | 39 |
| 3.1 Epoxy Material..... | 39 |
| 3.2 Material Processing..... | 40 |
| 3.2.1 HP-RTM Panel Processing | 40 |
| 3.2.2 Hand Cast Cylindrical Sample Processing..... | 44 |
| 3.3 Test Specimen Preparation..... | 46 |
| 3.3.1 Test Specimen for Dynamic Mechanical Analysis (DMA) | 46 |
| 3.3.2 Quasi-Static and Intermediate Strain Rate Uniaxial Tension Test Specimen | 47 |
| 3.3.3 Quasi-Static and Intermediate Strain Rate Uniaxial Shear Test Specimen..... | 48 |
| 3.3.4 Quasi-static and Intermediate Uniaxial Compression Test Specimen | 49 |
| 3.3.5 Tensile Polymeric Split-Hopkinson Pressure Bar (T-PSHPB) Test Specimen..... | 50 |

| | |
|---|----|
| 3.3.6 Compressive Polymeric Split-Hopkinson Pressure Bar (C-PSHPB) Test Specimen | 51 |
| 3.3.7 Test Specimens for Validation of Material Constitutive Model | 52 |
| 3.4 Mechanical Epoxy Characterization Test Equipment and Setup..... | 54 |
| 3.4.1 Dynamic Mechanical Analysis (DMA) | 55 |
| 3.4.2 Quasi-Static and Intermediate Strain Rate Uniaxial Tensile Tests | 56 |
| 3.4.3 Quasi-Static and Intermediate Strain Rate Uniaxial Shear Tests..... | 59 |
| 3.4.4 Quasi-Static and Intermediate Strain Rate Uniaxial Compression Tests..... | 60 |
| 3.4.5 Tensile Polymeric Split-Hopkinson Pressure Bar (T-PSHPB) Apparatus: High Deformation Rate Tension Testing..... | 62 |
| 3.4.6 Compressive Polymeric Split-Hopkinson Pressure Bar (C-PSHPB) Apparatus: High Deformation Rate Compressive Testing..... | 64 |
| 3.4.7 Validation Tests for Computational Model..... | 65 |
| Chapter 4 Epoxy Characterization Test Results..... | 66 |
| 4.1 DMA Test Results..... | 66 |
| 4.2 Uniaxial Tensile Test Results | 69 |
| 4.2.1 Quasi-static Strain Rate Tensile Test Results | 69 |
| 4.2.2 Intermediate Strain Rate Tensile Test Results | 70 |
| 4.2.3 High Strain Rate Tensile Test Results | 71 |
| 4.2.4 Summary of the Tensile Test Results..... | 74 |
| 4.3 Uniaxial Compression Test Results | 77 |
| 4.3.1 Quasi-static Strain Rate Compression Test Results..... | 77 |
| 4.3.2 Intermediate Strain Rate Compression Test Results..... | 78 |
| 4.3.3 High Strain Rate Compression Test Results | 80 |
| 4.3.4 Summary of the Compression Test Results | 82 |
| 4.4 Uniaxial Shear Test Results | 84 |
| 4.4.1 Quasi-static Strain Rate Shear Test Results | 84 |
| 4.4.2 Intermediate Strain Rate Shear Test Results..... | 85 |
| 4.4.3 Summary of the Shear Test Results | 86 |
| 4.5 Fracture Surface Investigation | 87 |
| Chapter 5 Epoxy Constitutive Modeling Fitting and Validation | 90 |
| 5.1 Material Model Identification for the Epoxy | 90 |
| 5.2 Calibration Method for the Constitutive Material Model | 93 |
| 5.3 Verification and Validation Methods for the Material Constitutive Model..... | 96 |

| | |
|---|-----|
| 5.3.1 Single Element Material Constitutive Model Verification | 96 |
| 5.3.2 Material Constitutive Model Validation | 98 |
| 5.4 Calibration Results of the Constitutive Modelling Results | 99 |
| 5.5 Single Element Material Model Verification Results | 102 |
| 5.6 Material Model Validation Results | 104 |
| Chapter 6 Discussion | 108 |
| 6.1 Mechanical Characterization..... | 108 |
| 6.2 Constitutive Modeling | 111 |
| Chapter 7 Conclusions and Future Work..... | 114 |
| 7.1 Conclusions..... | 114 |
| 7.2 Future work..... | 115 |
| Bibliography | 116 |
| Appendices..... | 128 |
| Appendix A - DMA Test Setup | 128 |
| A.1 DMA Strain Sweep | 128 |
| A.2 DMA Temperature Sweep | 128 |
| Appendix B - T-PSHPB and C-PSHPB Calibrations | 129 |
| B.1 Static Bar-calibration for T-PSHPB and C-PSHPB | 129 |
| B.2 Dynamic Bar-calibration for T-PSHPB and C-PSHPB..... | 130 |
| B.3 End-to-end Dynamic Calibration for C-PSHPB..... | 132 |

List of Figures

| | |
|---|----|
| Figure 1.1. The target values of global fuel efficiency standards for passenger vehicles using U.S. CAFE cycle equivalent (update May 2020) [1]. | 1 |
| Figure 1.2. Schematic of a bottom-up (hierarchical models) multiscale modeling approach. | 3 |
| Figure 2.1. Basic chemical structure of the epoxide function group, where R and R' represent other functional groups [20]. | 6 |
| Figure 2.2. Synthesis of monomeric DGEBA, the first commercial epoxy resin [14]. | 7 |
| Figure 2.3. Simple form of epoxidation of an olefin [14]. | 7 |
| Figure 2.4. Synthesis of the higher-molecular-weight DGEBA [14]. | 8 |
| Figure 2.5. (a) The viscosity-time/temperature profile of a typical curing process for an epoxy, adapted from Strong [29], and (b) isothermal viscosity-time profiles for typical snap-cure resins. | 11 |
| Figure 2.6. A typical curing process of an epoxy resin and an amine hardener: (a) schematic of the formation of a highly cross-linked amorphous molecular network, and (b) the chemical reaction formula for the curing process [22]. | 12 |
| Figure 2.7. Typical variation of specific volume and modulus with temperature for a cured epoxy material. | 15 |
| Figure 2.8. A typical compressive stress-strain curve for highly cross-linked epoxy resins and many glassy polymers. | 17 |
| Figure 2.9. The decomposition of stress for a glassy plastic proposed by Haward and Thackray [62], taken and adapted from Morelle [10]. | 19 |
| Figure 2.10. Schematic of strain rate and temperature dependent deformation response of glassy polymers under compressive loading. | 20 |
| Figure 2.11. Typical stress-strain curves in compression at various pressures for a glassy polymer. Taken and adapted from Pae and Bhateja [66]. | 20 |
| Figure 2.12. Strain rate regions with corresponding test equipment and characteristics. Adapted from Kuhn and Medlin [72]. | 24 |
| Figure 2.13. Schematic of a typical compressive SHPB apparatus. | 26 |
| Figure 2.14. Incident, Transmitted and Reflected waveforms for a typical SHPB test. | 26 |
| Figure 2.15. Schematic of a compressive SHPB apparatus: (a) elastic waveforms of the bars and bar-end velocities (arrows denoted the direction of the wave transmission and the direction of bar-end velocities); (b) compressive forces acting on the specimen. | 26 |
| Figure 2.16. The use of a material constitutive model in a commercial FE model. | 31 |

| | |
|--|----|
| Figure 2.17. A semi-empirical and one-dimensional elastic-viscoplastic model for glassy polymers. Adapted from Haward and Thackray [44]. | 34 |
| Figure 2.18. Overview of previously developed constitutive models for glassy polymers [10]. | 35 |
| Figure 3.1. Schematic of a typical HP-RTM process. | 41 |
| Figure 3.2. Images of the HP-RTM setup: (a) the hydraulic press along with the main tooling base, and (b) the lower mold insert. | 42 |
| Figure 3.3. Epoxy panel manufactured using the HP-RTM setup (top), and half panel where edge curvature and porosity are observed (bottom). | 43 |
| Figure 3.4. Edge view of a neat epoxy panel fabricated using the HP-RTM setup: (a) after demolding and prior to flattening (b) after flattening. | 44 |
| Figure 3.5. Custom-designed mold to manufacture the hand-cast samples. | 45 |
| Figure 3.6. A hand-cast neat epoxy cylinder. | 45 |
| Figure 3.7. DMA test specimen: (a) dimensions, and (b) image. | 46 |
| Figure 3.8. The dog-bone specimen dimensions for uniaxial tension tests at quasi-static and intermediate strain rates [113]. | 47 |
| Figure 3.9. The custom fixture for machining dog-bone tension specimens. | 48 |
| Figure 3.10. The specimen for uniaxial shear tests at quasi-static and intermediate strain rates. | 48 |
| Figure 3.11. The specimen for compression tests at quasi-static and intermediate strain rates. | 49 |
| Figure 3.12. The specimen and dimensions for the T-PSHPB tests. | 50 |
| Figure 3.13. Custom clamping fixture for the SHTB specimens. | 51 |
| Figure 3.14. Specimen dimensions for the C-PSHPB tests. | 52 |
| Figure 3.15. Geometrically symmetric specimen for validation of the material model for tensile and compressive stress states. | 53 |
| Figure 3.16. Geometrically asymmetric specimen for validation of the material model for shear stress states. | 53 |
| Figure 3.17. TA Instruments DMA Q800 and the specimen setup. | 55 |
| Figure 3.18. MTS servo-hydraulic test frame used for quasi-static tension tests. | 57 |
| Figure 3.19. HISR test apparatus for intermediate strain rate tests. | 57 |
| Figure 3.20. Custom-built 20,000 lb servo-hydraulic test frame used for the quasi-static and intermediate strain rate compression tests. | 61 |
| Figure 3.21. Carbide plates mounted between platens and epoxy specimen. | 61 |
| Figure 3.22. Schematic of T-PSHPB apparatus. | 62 |
| Figure 3.23. Image of the T-PSHPB apparatus. | 63 |

| | |
|---|----|
| Figure 3.24. Image of the C-PSHPB apparatus. | 65 |
| Figure 4.1. The strain sweep test result for the DMA test (HP-RTM specimen)..... | 66 |
| Figure 4.2. The results of temperature sweep DMA tests for the HP-RTM specimens..... | 68 |
| Figure 4.3. The results of the temperature sweep DMA tests for the hand-cast specimens..... | 68 |
| Figure 4.4. Uniaxial tensile engineering stress-strain curves for quasi-static strain rates of: (a) 0.00033 s^{-1} , and (b) 0.0035 s^{-1} . Note, five repeated tests were performed for each strain rate. | 70 |
| Figure 4.5. Uniaxial tensile engineering stress-strain curves for intermediate strain rates of: (a) 3.2 s^{-1} , and (b) 23.9 s^{-1} . Note, five repeated tests were performed for each strain rate..... | 71 |
| Figure 4.6. The force-time profiles measured from the incident end (two-wave) and transmitter bars (one-wave) for the T-SHPB test. | 72 |
| Figure 4.7. (a) A gauge section image of the T-SHPB test specimen indicating three sections analyzed using DIC, and (b) strain-time plots for three indicated sections. | 72 |
| Figure 4.8. Strain profiles calculated by the CHSB software and captured by the DIC method for the T-SHPB test. | 73 |
| Figure 4.9. Uniaxial tensile engineering stress-strain curves for a strain rate of 300 s^{-1} by CHSB software). Note, three repeated tests were performed at this strain rate. | 74 |
| Figure 4.10. Average stress-strain response of the epoxy material at the different tensile loading strain rates. | 75 |
| Figure 4.11. The increase of tensile elastic modulus associated with increased strain rate. | 76 |
| Figure 4.12. The increase of 0.3% offset strength associated with increased strain rate. | 76 |
| Figure 4.13. Uniaxial compressive engineering stress-strain curves for quasi-static strain rates of: (a) 0.0008 s^{-1} , and (b) 0.008 s^{-1} . Note, five repeated tests were performed for each strain rate. | 78 |
| Figure 4.14. Barreling of a cylindrical specimen at the different strains during a quasi-static compression test (0.008 s^{-1}). | 78 |
| Figure 4.15. Strain versus time for an intermediate strain rate compression tests (1.56 s^{-1}). | 79 |
| Figure 4.16. Uniaxial compressive engineering stress-strain curves at the intermediate strain rate (1.56 s^{-1}). Note, five repeated tests were performed for this strain rate. | 79 |
| Figure 4.17. The barreling of a cylindrical specimen at the different strains during one intermediate strain rate compression test (1.56 s^{-1}). | 80 |
| Figure 4.18. The force-time profiles from the incident end (two-wave) and transmitter bars (one-wave) for a C-PSHPB tests. | 81 |
| Figure 4.19. A comparison of strain calculated by the CHSB software and captured by the DIC method for a C-PSHPB test. | 81 |

| | |
|--|-----|
| Figure 4.20. Uniaxial compressive engineering stress-strain curves for the high strain rate of 550 s^{-1} . Note, three repeated tests were performed for this strain rate. | 82 |
| Figure 4.21. Average stress-strain response of the epoxy material at the different compression strain rates. | 83 |
| Figure 4.22. The increase of the yield strength associated with increased strain rates under compression. | 83 |
| Figure 4.23. Engineering shear stress-strain curves for quasi-static strain rates of: (a) 0.0013 s^{-1} , and (b) 0.012 s^{-1} . Note, five repeated tests were performed for each strain rate. | 84 |
| Figure 4.24. The DIC captured shear strain field for a shear specimen analysed at the quasi-static strain rate of 0.0013 s^{-1} (load axis in the x-direction). | 85 |
| Figure 4.25. Shear engineering stress-strain curves for intermediate strain rates of: (a) 16.8 s^{-1} , and (b) 28.4 s^{-1} . Note, five repeated tests were performed for each strain rate. | 86 |
| Figure 4.26. Average shear stress-strain response of the epoxy material at the different shear strain rates. | 87 |
| Figure 4.27. Representative specimens tested until failure: (a) quasi-static strain rate tensile test; (b) high strain rate tensile test; (c) intermediate strain-rate shear test; and (d) quasi-static compression test. | 88 |
| Figure 4.28. Fracture surface images for the quasi-static strain rate tensile test specimen (0.00033 s^{-1}). .. | 89 |
| Figure 4.29. Fracture surface images for the high strain rate tensile test specimen (300 s^{-1}) .. | 89 |
| Figure 5.1. Diagram of a general calibration procedure for an elastic-plastic material model. | 94 |
| Figure 5.2. Strain rate dependent of the true plastic stress-strain curves. | 95 |
| Figure 5.3. Tensile single element and its boundary conditions. | 97 |
| Figure 5.4 Shear single element and its boundary conditions. | 97 |
| Figure 5.5. A rigid-body-pin constrains the outer half of the pin-hole surface to the center reference point in the FEA model for the symmetric specimen (Solid element with 0.2 mm mesh size, 655,006 elements). | 98 |
| Figure 5.6. The true yield stress versus true plastic strain average experimental data for the tensile tests at different strain rates. | 99 |
| Figure 5.7. A comparison between the Johnson-Cook plasticity model (excluding rate dependence) and the corresponding experimental data (0.00033 s^{-1}). | 100 |
| Figure 5.8. Sum of three coefficients of determination for fitting the three curves (strain rates of 0.0035, 3.2, and 23.9 s^{-1}) versus the strain rate-dependent parameter C. | 101 |

| | |
|---|-----|
| Figure 5.9. Comparisons of true stress and true plastic strain data from the Johnson-Cook plasticity rate dependent model and the corresponding experiments: (a) the strain rate of 0.0035 s^{-1} ; (b) the strain rate of 3.2 s^{-1} ; (c) the strain rate of 23.9 s^{-1} | 102 |
| Figure 5.10. Comparisons of true stress-strain data for the single-element simulations with corresponding experiments: (a) tensile strain rate of 0.0035 s^{-1} ; (b) tensile strain rate of 3.2 s^{-1} ; (c) tensile strain rate of 23.9 s^{-1} ; (d) tensile strain rate of 300 s^{-1} ; (e) shear strain rate of 0.0013 s^{-1} | 103 |
| Figure 5.11. The critical area of the specimen used for the mesh sensitivity study..... | 104 |
| Figure 5.12. The true average strain values at different x-locations from the critical area of the specimen using different mesh sizes: (a) mesh sizes of 0.2 to 1 mm at 0.2 mm increment; (b) mesh sizes of 0.2 to 0.4 mm at 0.1 mm increment. | 105 |
| Figure 5.13. Comparisons of the strain field of the symmetric specimens for validation tests and the FE models simulations: (a) ϵ_{yy} of the FE model simulation; (b) ϵ_{yy} of the validation test (DIC); (c) ϵ_{xy} of the FE model simulation; (d) ϵ_{xy} of the validation test (DIC)..... | 106 |
| Figure 5.14. Comparisons of the strain field of the asymmetric specimens for validation tests and the FE models simulations: (a) ϵ_{yy} of the FE model simulation; (b) ϵ_{yy} of the validation test (DIC); (c) ϵ_{yy} of the FE model simulation; (d) ϵ_{yy} of the validation test (DIC)..... | 107 |
| Figure 6.1. Average true stress-strain plots for all the compressive and tensile tests at different strain rates. | 108 |
| Figure 6.2. Representative true stress-strain plots of all the compression and tensile tests at different strain rates (up to 10% strain)..... | 109 |
| Figure 6.3. Representative true stress-strain plots for all the tensile experiments and single element tests at different strain rates. | 112 |
| Figure 6.4. Five basic loading modes for UD composites | 113 |
| Figure B.1. An image of the CHSB software window showing calibration parameters..... | 129 |
| Figure B.2. A schematic diagram of the static bar-calibration. | 130 |
| Figure B.3. A schematic diagram of the dynamic C-PSHPB bar-calibration. | 131 |
| Figure B.4. Images of the CHSB software window showing the wave propagations | 131 |
| Figure B.5. A schematic diagram of the end-to-end dynamic calibration for the C-PSHPB apparatus. .. | 132 |
| Figure B.6. Images of the CHSB software window showing the result of an end-to-end dynamic calibration | 133 |

List of Tables

| | |
|--|----|
| Table 1.1. Typical mass reduction potential, specific properties, and cost of candidate lightweighting materials (relative to mild steel). Adapted from Elmarakbi [4]. | 2 |
| Table 2.1. Structure and characteristics of common epoxy resins [20, 28]. | 10 |
| Table 2.2. Summary of the common categories of curing agents [20, 24]. | 13 |
| Table 2.3. Summary of the common categories of modifiers [20, 23]. | 14 |
| Table 2.4. Several snap-cure epoxies for vehicle BIW structures [33, 34, 35]. | 16 |
| Table 2.5. Summary of the test methods for cured epoxy materials. | 21 |
| Table 2.6. Summary of some experimental strain-rate sensitivity studies for the glassy polymers. | 23 |
| Table 2.7. Survey of common material constitutive models for solid polymers [92]. | 32 |
| Table 3.1. EPIKOTE™ 06150 epoxy system (Hexion Inc.) [111]. | 39 |
| Table 3.2. Reported properties of cured EPIKOTE™ 06150 epoxy material (Hexion Inc.) [111]. | 40 |
| Table 3.3. Epoxy system part composition and conditioning parameters for the HP-RTM metering unit. | 41 |
| Table 3.4. The force profile of the hydraulic press and the mold temperature used for fabricating the neat epoxy panel. | 43 |
| Table 3.5. Summary of tools used and machining parameters for the DMA specimens. | 46 |
| Table 3.6. Summary of tools and machining parameters used for the quasi-static and intermediate strain rate tensile specimens. | 48 |
| Table 3.7. Summary of tools and parameters used for the CNC machining of quasi-static and intermediate strain rate shear specimens. | 49 |
| Table 3.8. Summary of tools and machining parameters used for the quasi-static and intermediate strain-rate compression specimens. | 49 |
| Table 3.9. Summary of tools used and machining parameters for the SHTB specimens. | 51 |
| Table 3.10. Summary of tools and machining parameters used for the C-PSHPB specimens. | 52 |
| Table 3.11. Summary of tools and parameters used for machining the validation specimens. | 53 |
| Table 3.12. Summary of the material characterization tests performed in this study. | 54 |
| Table 3.13. Summary of camera settings for the tension tests conducted at quasi-static and intermediate strain rates. | 58 |
| Table 3.14. Summary of camera settings for shear tests conducted at quasi-static and intermediate strain rates. | 59 |
| Table 3.15. Summary of the camera settings for compression tests performed at quasi-static and intermediate strain rates. | 62 |

| | |
|---|-----|
| Table 3.16. The specifications for the T-PSHPB components..... | 63 |
| Table 3.17. Parameters for the performed T-PSHPB tests..... | 63 |
| Table 3.18. The specifications of the C-PSHPB components..... | 64 |
| Table 3.19. Parameters for the performed C-PSHPB tests. | 65 |
| Table 3.20. Summary of the camera settings for validation tests performed at a quasi-static strain rate. .. | 65 |
| Table 4.1. Tg for HP-RTM and hand-cast specimens (95% CI and T-test) obtained using DMA. | 69 |
| Table 4.2. Summary of mechanical properties for tensile tests at different strain rates (95% CI) | 75 |
| Table 4.3. Summary of mechanical properties for compression tests at different strain rates (95% CI).... | 83 |
| Table 4.4. Summary of mechanical properties for shear tests at different strain rates (90% CI). | 87 |
| Table 5.1. A summary of assumptions for the material model. | 90 |
| Table 5.2. Summary of the plasticity models in Abaqus [98]..... | 92 |
| Table 5.3. Summary of plasticity hardening laws in Abaqus [98]..... | 93 |
| Table 5.4. Summary of the period setup for the tensile single-element tests..... | 97 |
| Table 5.5. The curve fitting method and results of Johnson-Cook material parameters for the basic curve. | 99 |
| Table 5.6. Strain rate-dependent parameters for the Johnson-Cook plasticity model..... | 101 |
| Table A.1. Test parameters used for the strain sweep tests. | 128 |
| Table A.2. Test parameters used for the temperature sweep tests. | 128 |

Chapter 1 Introduction

1.1 Composite Materials in the Automotive Industry

Over the last decade, as new fuel efficiency standards have been legislated in the major auto markets, including Canada, China, European Union (EU), Japan, and the United States (US) [1], there has been increased pressure for automakers to significantly improve the fuel efficiency of high-volume production passenger vehicles (PVs) (Figure 1.1). There are several methods to improve the fuel efficiency of a vehicle, including but not limit to drivetrain improvement, aerodynamics enhancement, and weight reduction. Out of these methods, reducing the weight of automotive body-in-white (BIW) structures has been regarded as an efficient way to improve vehicle fuel efficiency and reduce vehicle CO₂ emissions [2]. In general, reducing vehicle weight by 10% can improve the fuel efficiency of a conventional petroleum-fueled vehicle by 6-8% without sacrificing the vehicle performance, while the driving range of an electric vehicle can be increased by 13.7% without increasing the battery capacity [3]. Owing to their high specific mechanical properties, high-performance carbon fiber-reinforced plastic (CFRP) composite materials are regarded as a viable option for achieving the fuel economy targets for PVs and increasing the range of electric vehicles (Table 1.1) [4]. CFRP composite materials also exhibit excellent energy absorption characteristics [5], which is important for crashworthiness of automotive structures.

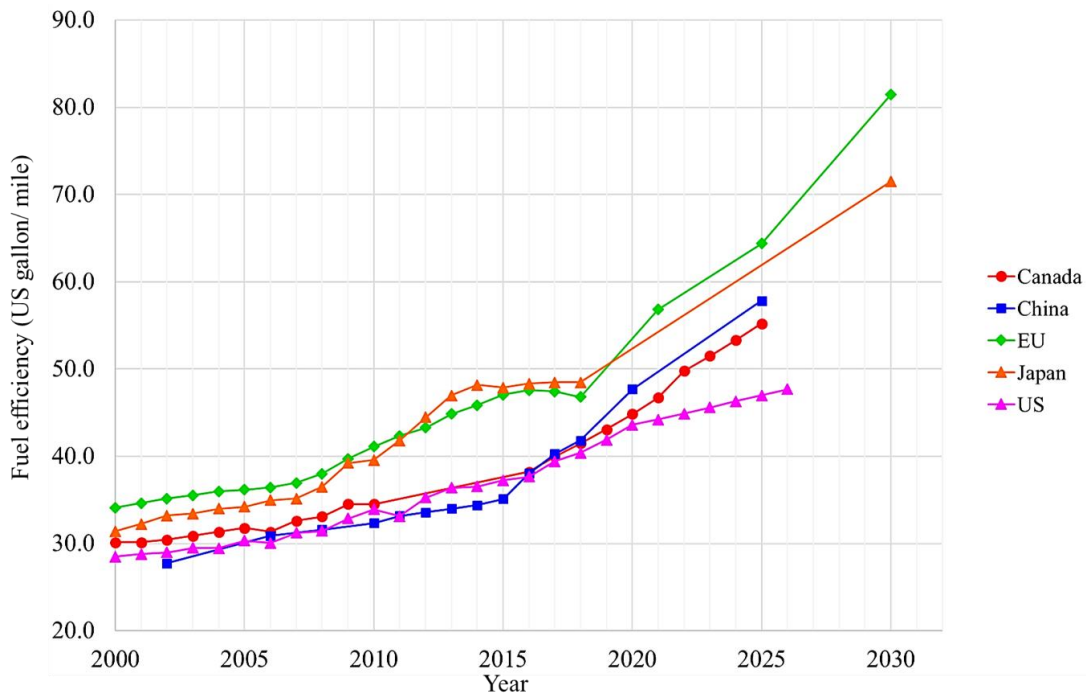


Figure 1.1. The target values of global fuel efficiency standards for passenger vehicles using U.S. CAFE cycle equivalent (update May 2020) [1].

Table 1.1. Typical mass reduction potential, specific properties, and cost of candidate lightweighting materials (relative to mild steel). Adapted from Elmarakbi [4].

| Material | Strength/ density | Modulus/ density | cost | Mass reduction potential (%) |
|--------------------------|----------------------|---------------------|-----------|---------------------------------|
| Mild steel | 1 | 1 | 1 | 0 |
| Carbon fiber composites | 18.3× | 1.93× | 1.5-5.0× | 50-90 |
| High strength steel | 1.86× | 1.00× | 0.9-1.2× | 0-10 |
| Adv. high strength steel | 2.25× | 1.00× | 0.8-1.5× | 0-30 |
| Aluminum | 3.95× | 1.02× | 1.3-2.0× | 30-60 |
| Magnesium | 3.66× | 1.02× | 1.5-2.5× | 30-70 |
| Titanium | 4.73× | 0.98× | 1.5-10.0× | 40-55 |
| Metal matrix composites | 3.81× | 1.45× | 1.5-3.0× | 30-70 |
| Plastics | 0.82× | 0.08× | 0.7-3.0× | 20-50 |
| Sheet molding compound | 4.39× | 1.16× | 0.5-1.5× | 20-30 |
| Glass fiber composites | 4.74× | 0.50× | 0.9-1.5× | 25-35 |

Despite several advantages, to date the applications of CFRP composite materials in BIW vehicle structures have been limited to luxury vehicles or supercars with low to medium production volumes, such as the sixth generation BMW 7-Series [6], the McLaren P1 and the Lamborghini Huracán EVO [7]. CFRP materials have not been widely integrated into the BIW structures of high-volume production vehicles due to the inherently high cost and long cycle times for fabricating CFRP materials with conventional processes [4]. The recent development of snap curing epoxy resins, low-cost carbon fiber fabrics, and automated rapid processing technologies like high pressure resin transfer molding (HP-RTM) [8], provide a promising opportunity to increase usage of CFRP materials in high-volume production vehicles. One niche application for these new CFRP materials is for energy absorbing vehicle structures and vehicle crashworthiness. Thus, characterizing the impact performance and strain rate dependent response of these CFRP materials, which is governed by the properties and local failure characteristics of the matrix material, is required. For impacted metallic components, energy is dissipated through plastic deformation, material hardening, and adiabatic heat loss. For CFRP laminate components, the impact energy is absorbed primarily through the formation of cracks, including matrix cracks, matrix/fiber interface debonding cracks, fiber fractures and delamination [9]. Due to the complexity of the material microstructure, the energy absorption characteristics of CFRP composite materials are affected by several factors, including the fiber and matrix material

properties, fiber volume fraction, fibre architecture, trigger, component geometry, loading speed, and loading direction [9].

A key characteristic of CFRP composite materials is the ability to tailor the material composition and mechanical properties, and ultimately the performance for a specific structural component. However, due to the complexity of the microstructure of CFRP composite materials, tailoring CFRPs to suit the vehicle requirements remains a challenge for automakers. Currently, a test-and-build approach which is expensive and time-consuming is used to optimize CFRP composite materials for structural components [10]. Thus, there is a demand for developing a virtual testing computational framework to predict the performance of CFRPs and reduce the extent of physical testing. A multiscale modeling strategy is favorable since it can align with the multiscale nature of composite materials and aid in assessing damage evolution and failure of CFRP materials. The material response at various length scales can be assessed, including the microscale where individual fibers and the surrounding matrix are considered, the mesoscale and macroscale where homogenized plies or a laminate containing multiple plies are represented, respectively, and the structural scale where components or an assembly of components are accounted for (Figure 1.2).

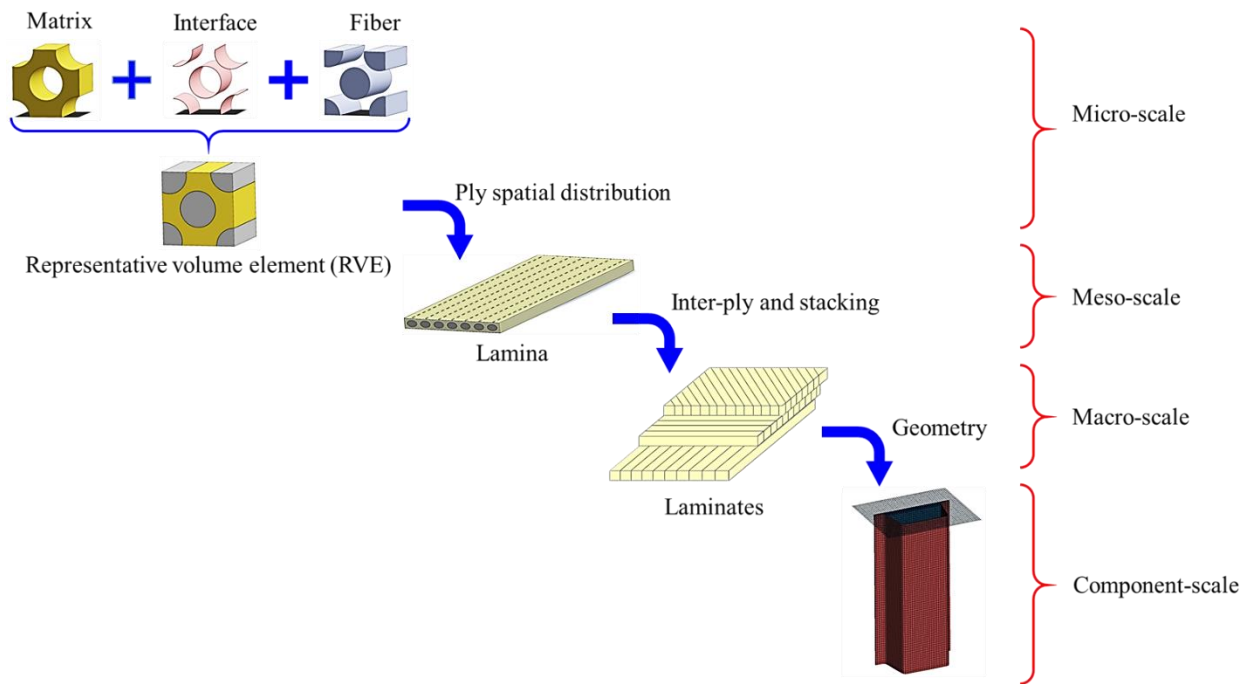


Figure 1.2. Schematic of a bottom-up (hierarchical models) multiscale modeling approach.

There are two main approaches for the computational multiscale analysis of heterogeneous materials: the top-down (global-to-local) approach and the bottom-up (hierarchical) approach [11], [12]. For the top-

down approach, normally, a finite-element analysis is first used to analyze the entire structure of interest and identify the local critical regions where the damage may occur. Further detailed analyses are then performed on those regions using lower length scale models [11]. The limitations of this method are the requirement of a large number of costly experiments and limited capabilities to predict different damage states [10]. On the other hand, the bottom-up approach begins the analysis from the scale of the material microstructure by considering the properties of the fibers and matrix. The homogenized constitutive response of the microstructure is passed up to the next length scale model to predict the mechanical response of composite materials (Figure 1.2) [13]. This bottom-up approach provides a better connection between different scales of entities, allowing better physical representation and fewer physical experiments [10]. In collaboration with other techniques, the bottom-up approach was a preferred method toward the virtual testing of composite materials.

To utilize a bottom-up multiscale approach, reliable constituent mechanical properties, including the matrix constitutive model, are critical for developing the micromechanical model. For the case of crashworthiness of CFRP structures, the strain rate dependent response of the matrix material is a critical element to support the development a material micromechanical model.

1.2 Research Objectives

The overarching goal of this study was to support the development of a robust high-fidelity virtual micromechanical tool to be used within a multiscale modeling framework for predicting the performance of CFRP materials and energy absorbing structures. The main research objectives comprised: *(i)* characterizing the mechanical properties of a new snap-cure epoxy material under different applied strain rates and modes of loading, *(ii)* identifying and calibrating a suitable constitutive model, and *(iii)* assessing the properties and constitutive model using an independent set of experimental data. A series of uniaxial mechanical tests were conducted to characterize the strain rate dependent stress-strain behaviour of the epoxy material under a variety of strain rates, ranging from quasi-static to dynamic strain rates. Based on the mechanical characterization results, an existing constitutive model in the commercial finite element software Abaqus (Dassault Systèmes, Vélizy-Villacoublay, France) was assessed to verify suitability for the studied epoxy material.

1.3 Thesis Outline

The remainder of the thesis is comprised of six chapters. Chapter 2 provides the theoretical background for epoxy resins and a review of the literature on mechanical characterization and constitutive modelling techniques for epoxy materials. In Chapter 3, the characterization methods used to study the mechanical response of the studied epoxy material is described. Chapter 4 presents the results of the mechanical characterization tests, including Dynamic Mechanical Analysis (DMA), tensile, compressive and shear tests at different strain rates, and the fracture surface investigation. Chapter 5 demonstrates the constitutive modeling of the studied epoxy material, covering the constitutive model identification and calibration, as well as model verification and validation. Chapter 6 discusses the overall mechanical deformation response of the studied epoxy material and the prediction capability of the investigated constitutive model, focusing on the strain rate dependent response. Finally, Chapter 7 concludes the thesis by summarizing the main findings and proposing recommendations for future work.

Chapter 2 Background and Literature Review

In this chapter, relevant background information for epoxy materials is first provided. Previous studies related to the mechanical characterization of epoxy materials are presented, and the limitations of these studies are discussed. Finally, a review of constitutive models for epoxy materials is presented.

2.1 Epoxy Materials

Epoxy materials or epoxies are classified as thermosetting polymers or thermosets. Owing to their unique properties, epoxies are widely used as coatings, adhesives, and in structural applications when reinforced with fibers (e.g., fiber-reinforced plastic (FRP) composites). The term “epoxy” comes from the epoxide functional group (e.g., ethylene oxide or oxirane), which is a highly reactive three-membered ring structure containing one oxygen and two carbon atoms from a hydrocarbon (Figure 2.1) [14]. Any material that contains a molecular structure with an epoxide group can be classified as an epoxy. Different compounds that react with epoxide groups result in a variety of epoxy materials, and the common non-epoxide parts of an epoxy molecular structure can be aromatic, cycloaliphatic, and aliphatic hydrocarbons. With a variety of molecular structures that can be generated using similar chemical processes, epoxies are commercially successful because of their diversity of functionalities. Moreover, the base epoxy molecule or monomer can be easily modified to suit a wide range of applications by combining with the different types of curing agents and appropriate modifiers, which are discussed in the following sections. Extensive studies that focused on the characteristics and properties of different classes of epoxies have been undertaken and reported [15, 16, 17, 18, 19].

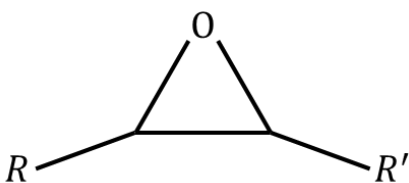


Figure 2.1. Basic chemical structure of the epoxide function group, where R and R' represent other functional groups [20].

Monomers are single molecules that can be reacted to form polymers that consist of many monomers. Two types of processes have been commonly used to commercially prepare epoxy monomers: by dehydrohalogenation of the chlorohydrin intermediate prepared by the reaction of epichlorohydrin with a suitable di- or polyhydroxyl (Figure 2.2.) and by the reaction of olefins with oxygen-containing compounds

such as peroxides or per-acids (Figure 2.3.) [14]. The former process is more widely used to produce a variety of epoxy monomers [20].

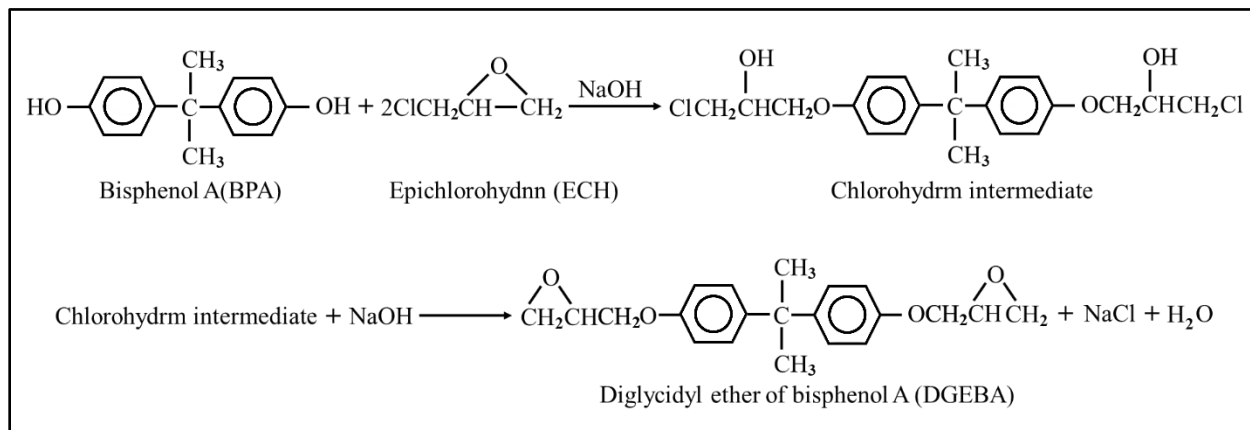


Figure 2.2. Synthesis of monomeric DGEBA, the first commercial epoxy resin [14].

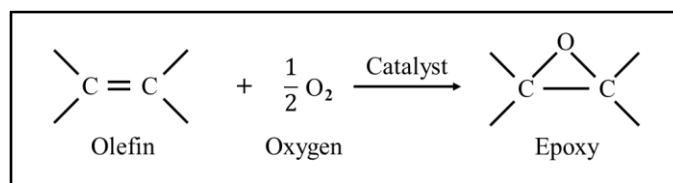


Figure 2.3. Simple form of epoxidation of an olefin [14].

2.1.1 Polymerization and Uncured Epoxy Resin Properties

Polymerization is a chemical reaction in which monomers are synthesized to form chain-like polymer macromolecules that contain many monomers. Polymerization may occur if monomers have the appropriate functionalities or number of reactive sites to promote covalent bonding with other molecules [21]. Conventionally, the polymerization process can be differentiated as addition polymerization and condensation polymerization. For addition polymerization or chain polymerization, all the monomers react and become part of the polymer without the creation of a by-product during the process. For condensation polymerization or step polymerization, part of the monomer molecule forms a by-product (normally a low-molecular-weight molecule like water or hydrochloric acid) during the polymerization process [22]. For example, higher-molecular-weight DGEBA can be synthesized in the presence of excess caustic and BPA to form an epoxy resin (Figure 2.4). The degree of polymerization (DP) (i.e., average number of repeating units in the polymer molecular chains) of synthesized DGEBA can vary from 1 to 20, and the state of the compound can differ from a low viscous liquid ($n < 2.5$) to a high melting point solid ($n > 14$) [21]. With

the DP of the oligomers in the range of $1 \leq n \leq 4$, the polymerization process is known as a ‘Taffy’ process, while the production process of the higher-molecular-weight polymers (DP in the range $3 \leq n \leq 20$) is known as a ‘fusion’ or ‘chain extension’ process [23]. Generally, as the degree of polymerization increases, the fluidity of an epoxy resin decreases. Most uncured epoxies used to fabricate composite materials are liquids or soft gels at room temperature, thus the DP for common epoxy resins is normally < 5 to allow for ease of processability [24].

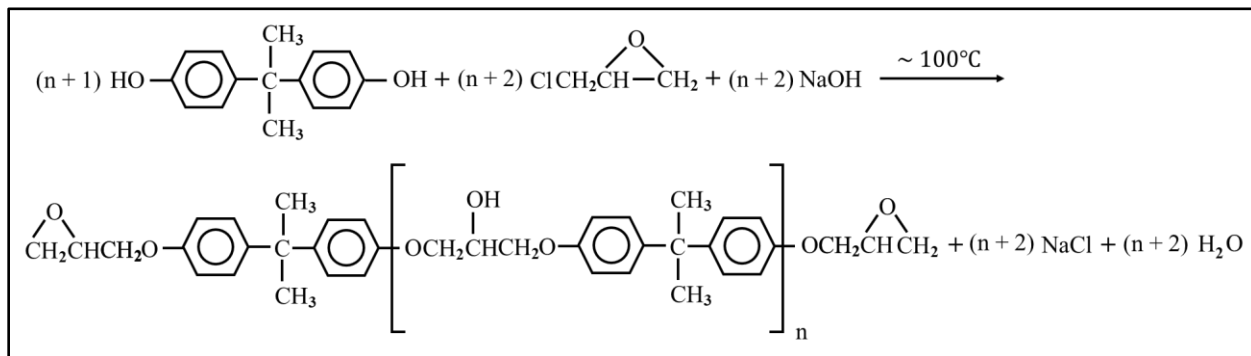


Figure 2.4. Synthesis of the higher-molecular-weight DGEBA [14].

Many properties can be used to describe the characteristics of uncured epoxy resins, including but not limited to density, viscosity, epoxy equivalent weight (EEW), functionality, molecular weight, degree of polymerization, softening point, hydroxyl equivalent weight, iodine number, molecular weight distribution, colour, specific gravity, refractive index, and chlorine content [14]. The viscosity of liquid resins is a rheological parameter that defines the resistance of a liquid to flow, which is typically temperature dependent. Resin viscosity is an important parameter when processing epoxies or fiber-reinforced/epoxy composites since it will influence the fiber wet-out process and therefore the quality of the fabricated part. The common methods to measure the viscosity of a liquid include orifice viscometer (e.g., ford viscosity cup), falling ball viscometer (e.g., Hoesppler viscometer), capillary viscometer, rotational viscometer, and ultrasonic method [25]. Functionality and DP are characteristics that influence the molecular chain cross-linking process during curing (Section 2.1.2). The functionality of epoxy resins describes the number of reactive sites per epoxy molecule, where higher functionalities allow for a higher degree of cross-linking during cure. The DP also directly influences the cross-linking process and is directly related to the molecular weight (M) through the relationship described by Equation 2.1, where M_0 is the formula weight of the repeating group.

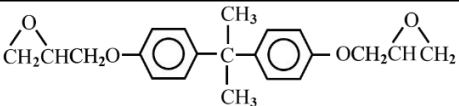
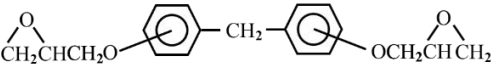
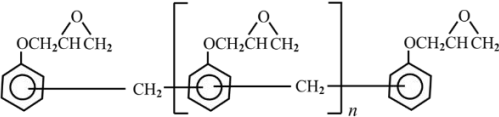
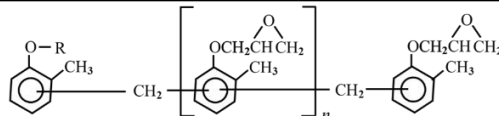
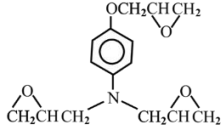
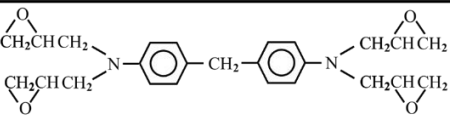
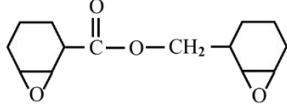
$$M = (DP)M_0 \quad (2.1)$$

Epoxy equivalent weight (EEW) is another key property that influences the processability of resin. The definition of the EEW of an epoxy resin is the weight of resin in grams which contains one mole of epoxy, and it can be estimated volumetrically using aqueous concentrated hydrochloric acid with dioxane [24]. EEW can be used to determine the stoichiometric ratio between the epoxy resin and curing agent for curing optimization.

Uncured polymerized epoxy resins can be classified as DGBEA, diglycidyl ether of bisphenol-F (DGBEF), Novolac, Aliphatic, and Glycidyl amine (Table 2.1). DGEBA resins were the first commercial epoxy resins, which are still widely used for the formulation of adhesives, coatings, and composites. The presence of the phenol glycidyl group increases the processability of DGEBA resins but limits their thermal resistance. The glass transition temperature (T_g) of cured DGEBA epoxy is typically less than 120°C, which limits use for high-temperature applications [26]. The major difference between different grades of DGEBA resins is the viscosity at 25°C, which varies from 5 to 20 Pa • s (Table 2.1) and is directly proportional to the molecular weight. Higher molecular weight DGEBA resins can be used to adjust the resin viscosity and to prevent the low molecular weight resins crystallization during storage [20]. DGEBA resins typically have lower viscosity, improved mechanical properties, and superior chemical resistance than DGEBA resins. Unlike DGEBA resins that have a wide range of molecular weights, the DGEBA resins rarely have high molecular weights. The DGEBA/F or glycidyl ether epoxide resins can be formulated into snap-curing resin systems when combining with an aliphatic polyether curing agent and metal salt catalysts [27].

Two additional classes of polymerized epoxy resins include phenol and cresol novolac. Either phenol or cresol is combined with formaldehyde to form a polyphenol, which then reacts with epichlorohydrin to yield epoxy [20]. In comparison to the cured DGEBA/F resins, the cured novolac epoxy resins normally have higher T_g values due to their higher functionality number, allowing for high-temperature application. Glycidyl amine epoxy resins are produced by the reaction of epichlorohydrin and amine. One of the most important resins in this class is tetraglycidyl methylene dianiline (TGMDA), which has superior high-temperature performance and excellent mechanical properties, ideal for advanced composites for aerospace applications. Cycloaliphatic epoxy resins that contain an epoxy group in the ring structure rather than external or pendant are special types of aliphatic epoxies, and these classes of epoxies are characterized by low viscosity and relatively high thermal-mechanical performance.

Table 2.1. Structure and characteristics of common epoxy resins [20, 28].

| Diglycidyl Ether of Bisphenol A (DGEBA) Functionality: 2 | |  | |
|---|-----------|---|--|
| Epoxy equivalent weight (g/eq) | Form | Viscosity at 25 °C Pa·Sec (cP) | Comments |
| 171 - 200 | Liquid | 3.5 – 19 (3,500 – 19,000) | May crystallize on storage. Can contain small amount of higher polymer to prevent crystallization. |
| Diglycidyl Ether of Bisphenol F (DGEBF) Functionality: 2 | |  | |
| Epoxy equivalent weight (g/eq) | Form | Viscosity at 25 °C Pa·Sec (cP) | Comments |
| 158 - 165 | Liquid | 5.0 – 8.0 (5,000 – 8,000) | Isomeric mixture that will not crystallize on storage. |
| Polyglycidyl Ether of Phenol-Formaldehyde Novolac Functionality: 2.2-3.6 | |  | |
| Epoxy equivalent weight (g/eq) | Form | Viscosity at 52 °C Pa·Sec (cP) | Comments |
| 172 - 181 | Semisolid | 1.1 – 50.0 (1,100 – 50,000) | Uses for high temperature applications |
| Polyglycidyl Ether of <i>o</i> -Cresol-Formaldehyde Novolac Functionality: 2.7-5.4 | |  | |
| Epoxy equivalent weight (g/eq) | Form | Melting Point (°C) | Comments |
| 200 - 235 | Semisolid | 35 - 99 | Used for high-temperature application; R represents chlorohydrins, glycols, and/or polymeric ethers. |
| Triglycidyl <i>p</i> -Aminophenol (TGAP) Functionality: 3 | |  | |
| Epoxy equivalent weight (g/eq) | Form | Viscosity at 50 °C Pa·Sec (cP) | Comments |
| 95-107 | Liquid | 0.55 – 0.85 (550 – 850) | Used extensively for preregs and adhesives. |
| <i>N,N,N',N'</i> - Tetraglycidyl Methylene dianiline (TGMDA) Functionality: 4 | |  | |
| Epoxy equivalent weight (g/eq) | Form | Viscosity at 50 °C Pa·Sec (cP) | Comments |
| 117-133 | Liquid | 10.0 – 15.0 (10,000 – 15,000) | Used for preregs |
| 3,4 epoxy cyclohexylmethyl – 3,4 – epoxy cyclohexane carboxylate Functionality: 2 | |  | |
| Epoxy equivalent weight (g/eq) | Form | Viscosity at 50 °C Pa·Sec (cP) | Comments |
| 131-143 | Liquid | 0.25 – 0.45 (250 – 450) | Offers high temperature performance and UV resistance. |

2.1.2 Curing Process for Epoxies

The state of epoxy resins can change from liquid to solid, often without a change in temperature or the creation of by-products, through a process called curing or cross-linking. The curing process involves mixing the epoxy resin with a reacting compound known as a curing agent or hardener. The curing agent can either react with the epoxy resin to synthesize a co-monomer, or act as a catalyst to initiate the epoxy resin homo-polymerization process. The chemical reactions that occur during the resin curing process involve the creation of strong covalent bonds between the polymer chains or macromolecules (i.e., crosslinking) [24]. During the processing of fiber-reinforced/epoxy composites, the epoxy resin/curing agent mixture is typically exposed to an elevated temperature for a predetermined time. The first stage involves heating the mixture to reduce the resin viscosity for ease of fiber wet-out, while during the second stage the crosslink density (i.e., degree of cure) increases with time at constant temperature causing the viscosity of the mixture to increase [29] (Figure 2.5). Once the crosslink density reaches a threshold, known as the gel point, the viscosity rapidly increases, and the mixture transitions from a liquid to a soft solid gel state [29]. With additional time the crosslink density continues to increase eventually reaching a second threshold, known as the vitrification point, where the epoxy transitions from a soft gel to a hard solid. It is beyond the vitrification point that the highly cross-linked amorphous molecular network that is characteristic of epoxy materials is formed (Figure 2.6 a) [22]. The degree of cure achieved at the end of the curing process directly influences the glass transition temperature, T_g , of the epoxy material [20]. As an example, the cross-linking process for an epoxy resin and an amine-curing agent is shown (Figure 2.6 b).

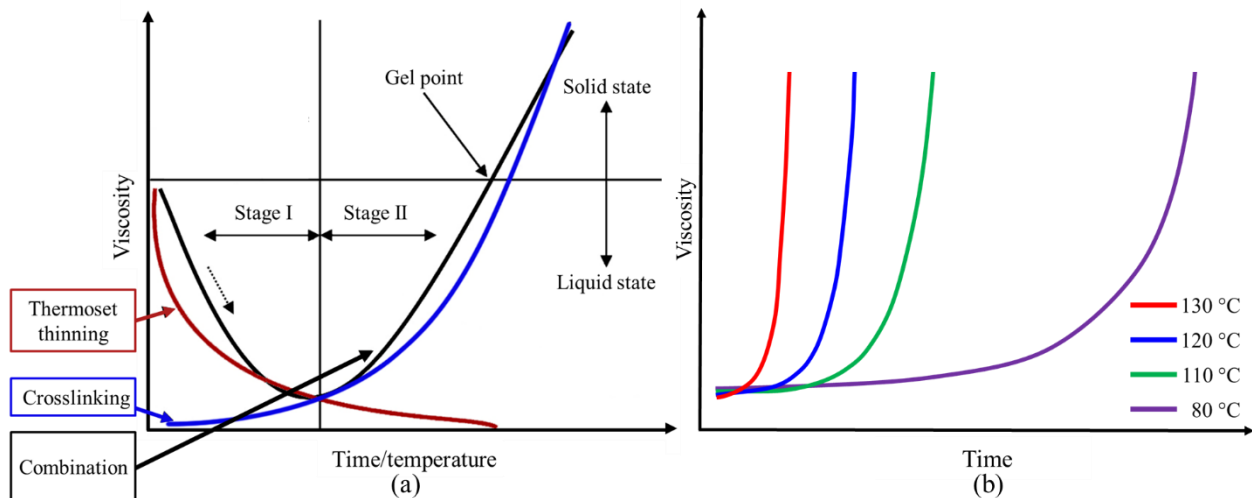
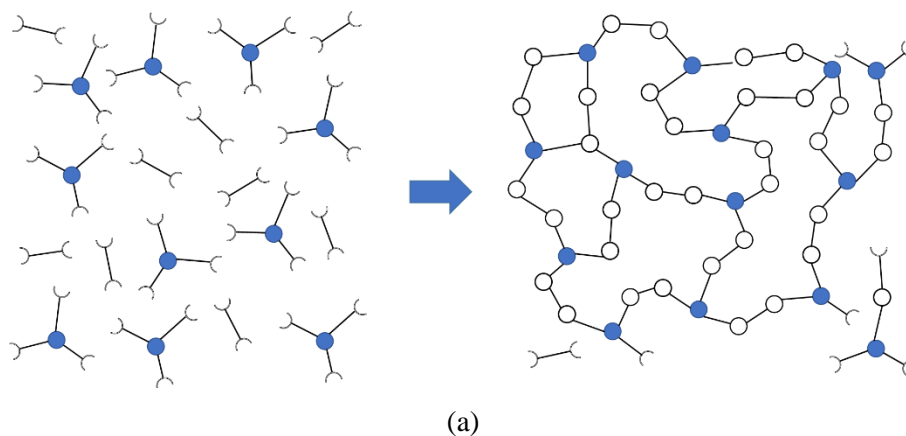
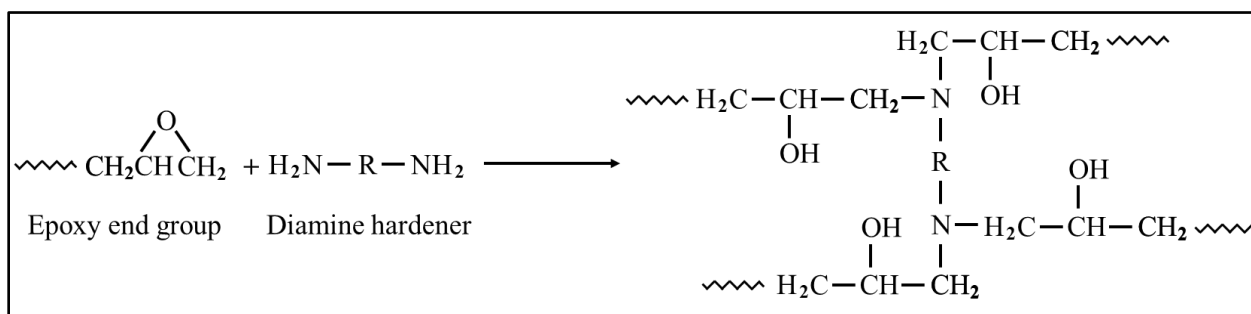


Figure 2.5. (a) The viscosity-time/temperature profile of a typical curing process for an epoxy, adapted from Strong [29], and (b) isothermal viscosity-time profiles for typical snap-cure resins.



(a)



(b)

Figure 2.6. A typical curing process of an epoxy resin and an amine hardener: (a) schematic of the formation of a highly cross-linked amorphous molecular network, and (b) the chemical reaction formula for the curing process [22].

Combining epoxy resins with different curing agents allows for many distinct types of cured epoxy materials to meet different characteristic requirements, including material stability, curing temperature and time, physical properties, thermal and mechanical performance, chemical resistance, toxicological tolerance, environmental requirement, and cost. A variety of chemical compounds containing active hydrogen atoms can be used as curing agents, including aliphatic and aromatic amines, amidoamines, boron-trifluoride (BF₃)-amine complexes, imidazoles, and anhydrides (Table 2.2). The choice of curing agent can significantly influence the curing process and the thermo-mechanical properties of epoxy materials. For example, by combining epoxy resins with different curing agents, the cure time can vary from seconds to hours; the cure temperature can be set from below room temperature to more than 200 °C; the cured epoxy can be soft or rigid; the T_g of the cured epoxy can range from below room temperature to more than 300 °C; the mechanical properties can greatly vary [20]. In general, for the same epoxy resin, the aromatic curing agents are likely to produce cured epoxies that have superior stiffness and strength in comparison with the aliphatic curing agents. However, aromatic curing agents require higher curing

temperatures since higher energy is needed to properly position the reactive end groups [28]. The cross-linked density of the cured epoxy is an important parameter, which is affected by the different combinations of epoxy and curing agents. A reduction of the crosslink density can reduce the shrinkage of the epoxy resins during cure and allow for more elongation of the cured material before failure; however, this can lower the strength and stiffness of the cured epoxy [28]. An increase of the crosslink density will increase the heat distortion temperature (HDT) and T_g of the cured epoxy, while also lowering the strain-to-failure (i.e., more brittle). If the crosslink density is held, replacing the aromatic molecules with aliphatic or cycloaliphatic molecules results in greater flexibility and extensibility for the cured epoxy [28].

Table 2.2. Summary of the common categories of curing agents [20, 24].

| Curing Temperature | Curing agents | Description |
|--------------------|---|---|
| Room | Aliphatic amines | Most common curing agents for epoxy resins. For these curing agents, the primary and secondary amino-epoxy reactions occur during the curing process. |
| | Polyamides | Less reactive than most polyamines. Provide good adhesion and toughness, but introduce dark color to the end products. |
| | Amidoamines | Contain both amide and amine groups, which promote higher T_g . These curing agents offer better moisture resistance than aliphatic polyamines. |
| Room or elevated | Boron trifluoride (BF ₃) -amine complexes | Can be used for resin castings and coatings with T_g as high as 200 °C. |
| | Imidazoles | Normally employed as curing accelerators when combined with other agents, but they can also be highly effective as sole curing agents. |
| Elevated | Aromatic amines | Often used in high-performance composites. They usually require high cure temperature to achieve superior T_g and greater chemical resistance than the same epoxy-aliphatic amines combination. |
| | Anhydrides | Anhydrides can offer low viscosity, noncritical mix ratios, and long pot life. |

2.1.3 Epoxy Additives

In addition to the resin and curing agent, modifiers or additives are often used during the epoxy curing process. Modifiers may be employed to provide epoxies with specific physical or mechanical properties, for both uncured and cured form. Commonly used classifications of modifiers include diluents, fillers, resinous modifiers, elastomeric modification, thermoplastics, internal mold release agents, flame retardants, and pigments (Table 2.3).

Table 2.3. Summary of the common categories of modifiers [20, 23].

| Modifiers | Description |
|--------------------------|--|
| Diluents | Non-reactive or reactive diluents are usually used for reducing the viscosity of resins to improve processability of composite materials by improving fiber wetting. Can also be combined with other modifiers. |
| Fillers | Fillers are the most common modifiers used with epoxy resins as extenders and reinforcements to modify the characteristics of cured and uncured epoxy. The filler types can be categorized as minerals, metals, glass, carbon, and miscellaneous organics. |
| Resinous modifiers | There are many resinous modifiers for epoxy resins. Nylons, polysulphides, and polyvinyl formal/ butyral are used to improve the material toughness; phenolic and bismaleimide pre-polymers enhance higher temperature capability; fluorinated polymers offer hydrophobic characteristics; silicones are used as release agents to improve processability. |
| Elastomeric modification | Elastomeric modifiers can dramatically improve the toughness of epoxies with mild reductions of other mechanical properties. |
| Thermoplastics | Thermoplastics can be included in epoxy formulations to increase the fracture toughness of the cured product. |
| Flame retardants | Normally, flammability is driven by the number of carbon and hydrogen atoms in a polymer system. The halogens and char-forming aromatics can be used to decrease the flammability of epoxy. |
| Pigments and dyes | Color can be introduced into the epoxy resins by using a variety of pigments and dyes, where the difference between the pigments (insoluble particles) and dyes (soluble organic molecules) is the solubility. |

2.1.4 Glass Transition Temperature (T_g) of Cured Epoxy

The glass transition temperature, T_g , is the temperature at which the deformation response of a glassy polymer (e.g., a highly cross-linked cured epoxy material) changes from a glassy to rubbery state or vice versa (Figure 2.7). When an oscillating load is applied to a polymer in the glassy state, the microstructure of the polymer only undergoes vibrational motion, and the molecular chains exhibit increased mobility as the temperature of the polymer increases. As the glassy polymer is heated to a temperature above the T_g (rubbery state), the Young's modulus is usually much lower than when below the T_g (Figure 2.7). In other words, the glassy polymer softens when heated above the T_g due to the increased mobility of the molecular chains, resulting in an increased viscous response. The value of T_g primarily depends on the molecular structure of the material, including the crosslink density and the composition of the molecular chains [20]. Normally, the crosslink density or degree of cure governs the T_g when an epoxy system has fixed resin, curing agent, additive type, and the stoichiometric ratio [30].

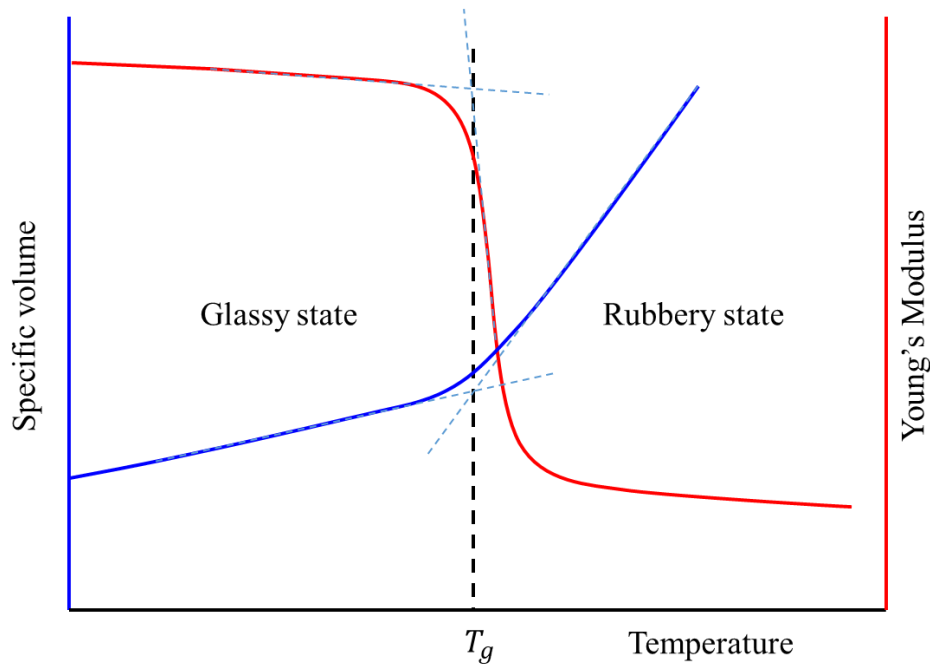


Figure 2.7. Typical variation of specific volume and modulus with temperature for a cured epoxy material.

2.1.5 Snap-Cure epoxy

CFRP composite parts are commonly fabricated in a closed two-part mold using liquid resin processes such as resin transfer molding (RTM) or wet compression molding (WCM). Liquid resin processes involve placing the dry reinforcing fibers into the mold cavity and infusing the fibers with the thermosetting resin. The resin is then allowed to cure at elevated temperature for a predefined time. Thus, the curing time of the resin directly affects the production speed of CFRP parts and equipment utilization. Conventional epoxy resins typically have long curing times, thus resin-based CFRP composites have limited application in mass production vehicles [31]. During the last decade, new snap-cure epoxies have been specifically formulated for automotive CFRP parts where rapid fabrication cycle times are required (Table 2.4). Advances in polymer chemistry has enabled a significant reduction in the cure times of epoxy resins, making the production speed of snap-cure resin-based CFRP parts comparable to that of stamped steel. Although the formulations of snap-cure epoxy systems have not been fully disclosed, the common approaches to achieving a fast curing cycle for an epoxy system were to use particular hardeners (e.g., polyethylene-tetraamine) and adding catalysts or accelerators [27, 32]. One important consideration for snap-cure epoxy systems is the thermal latency. The viscosity of typical snap-cure epoxies can increase rapidly during the fabrication process (Figure 2.5), which may inhibit a full wet-out of the reinforcement fibers during a liquid resin CFRP fabrication process. Thus, special additives can be added to the snap-cure epoxy to delay the initial viscosity increase [32]. Another important consideration is the T_g of the cured epoxy material, and thus the CFRP material. The T_g of the epoxy should be high enough to ensure adequate mechanical performance in an elevated temperature environment.

Table 2.4. Several snap-cure epoxies for vehicle BIW structures [33, 34, 35].

| Supplier | Trade name | Cure time / temperature (° C) | Processes | T_g (° C) |
|----------|--|-----------------------------------|-------------|-------------|
| Hexion | EPIKOTE™ EP TRAC 06150/ EK TRAC 06150/ HA TRAC 06805 | 5 – 10 min / 110 – 120 ° C | WCM/ RTM | 110 – 120 |
| Hexion | EPIKOTE™ EP TRAC 06170/ EK TRAC 06170/ HA TRAC 06805 | 45 sec – 3 min / 115 – 145 ° C | WCM/ RTM | 120 – 135 |
| Huntsman | Araldite® LY 3585/ Aradur® 3475 | 1 – 2 min / 115 – 140 ° C | WCM/ RTM | 120 – 130 |
| Huntsman | Araldite® LY 3031/ Aradur® 3032 | 30 sec / 140 ° C | WCM/ RTM | 120 – 130 |
| Dow | VORAFORCE™ 5300 | 30 sec – 3 min / 115 – 145 ° C | WCM/ RTM | 120 |

WCM- wet compression molding; RTM-resin transfer molding

2.1.6 Mechanical Properties of Cured Epoxy

Epoxies are one of the most widely used material systems for fabricating composite materials and for use as a structural adhesive; thus, the stress-strain behaviour of epoxy materials have been widely reported in the literature [36, 37]. The mechanical properties of cured epoxy resins depend on many internal factors, including the chemical structure of the epoxy and curing agent, the stoichiometric ratio of the epoxy and amino, and the crosslink density [30, 37, 38, 39]. A representative stress-strain curve for a highly cross-linked epoxy material under quasi-static uniaxial compressive loading reveals the four typical deformation stages of the material (Figure 2.8): elastic (linear elastic and viscoelastic); onset of plastic flow; strain-softening; and strain hardening or re-hardening [40].

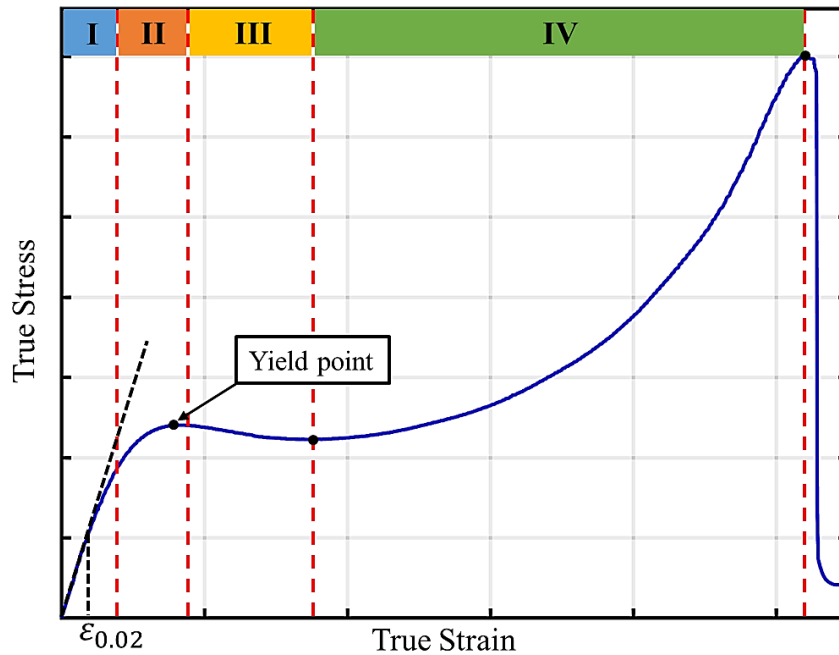


Figure 2.8. A typical compressive stress-strain curve for highly cross-linked epoxy resins and many glassy polymers.

The first stage of deformation is elastic, where a combination of linear elastic and viscoelastic deformation occurs simultaneously as the strain increases (Figure 2.8, stage I). The linear region of the deformation response typically only spans 1-2 % strain [41]. With increasing strain, the glassy polymer exhibits a nonlinear stress-strain response due to the increase of the nonlinear viscoelastic or anelastic deformation. Some researchers (Chen et al. [42] and Hasan [43]) divided this region into linear elastic and nonlinear elastic. In this region, the exhibited deformation was a result of minor intermolecular interaction and side group mobility [44, 45], and the anelastic part of deformation was dominated by the delayed

movement of local amorphous chains (causing stress relaxation) [10]. For glassy polymers, the deformation response of the material in this stage can be influenced by the strain rate and temperature due to the viscoelastic effects [40].

The onset of plastic flow occurs during the second deformation stage where a transition from elastic to plastic deformation occurs (Figure 2.8, stage II). The classical definition of the yield point (yield stress) is the stress value at which the material deformation is not fully reversible. However, for many polymers, the distinctions between elastic and plastic deformation are typically not obvious [46]. By convention, the yield point can be defined as the point at which the stress does not increase with the increase of the strain (i.e., local stress maximum) [47]. In this strain region, plastic deformation is mainly governed by the irreversible cross-linked molecular structure reconfiguration caused by movement of the molecular chains. Argon [48] proposed a double-kinks deformation model to explain the mechanism of plastic deformation for a glassy polymer, which showed excellent agreement with the experimental results for several glassy polymers. Many studies indicated that the yield behaviour of glassy polymers is largely affected by the hydrostatic pressure, strain rate, temperature in this stage [36, 40, 42, 49, 50, 51, 52, 53, 54, 55].

The third deformation stage constitutes strain softening immediately after the yield point (Figure 2.8, stage III). There is no general agreement on the origin of the softening. If strain-localization or necking occurs, the softening behaviour is associated with the evolution of the macroscopic shear bands [40]. In many cases, micro-shear bands occur within the specimen rather than external macro-shear bands. In these situations, some researchers proposed that the yield and softening were determined by the initiation, evolution, and merger of the shear transformation zone (STZ) [37, 43]. Some researches suggested that the rearrangement of the free volume is the cause of the strain softening [56, 57].

The final deformation stage consists of strain hardening or re-hardening of the material (Figure 2.8, stage IV), where the stress begins to rise again as the strain increases. This phenomenon can be described by a rubbery elastic response of the entangled cross-linked molecular network, where the orientation and the stretching of the molecular chains are confined by the network. This concept was first proposed by Haward and Thackray [44] (Figure 2.9), and was widely accepted by many successful material models that describe the mechanical response of glassy polymers [43, 58, 59]. The material response in this stage is primarily affected by the cross-link density and secondly by the temperature and strain rate. For the same test condition, the strain hardening behaviour of one glassy polymer can be different because of the difference in entropic resistance of molecular chain reconfiguration [60, 61].

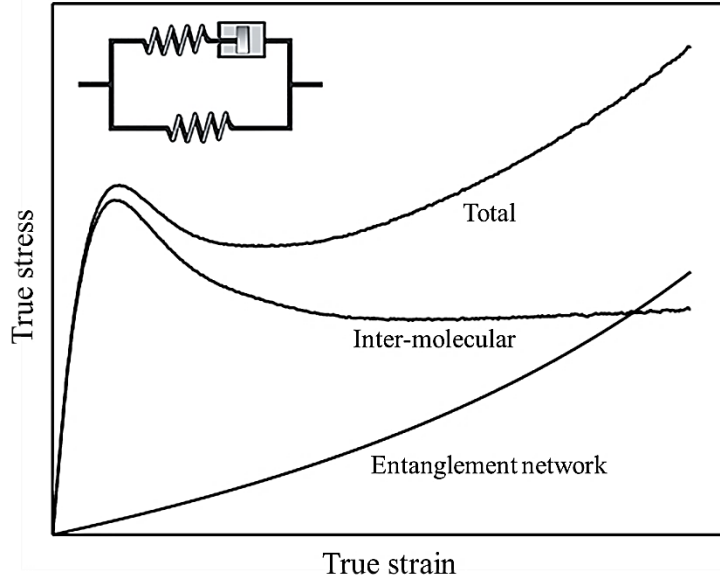


Figure 2.9. The decomposition of stress for a glassy plastic proposed by Haward and Thackray [62], taken and adapted from Morelle [10].

These four compressive deformation stages are mainly reported for glassy polymers that fail at large strains (normally 30 – 50% strain to failure), and many material models have been developed based on these behaviours. Since the mechanical deformation of highly cross-linked epoxies share many similar responses with the glassy polymers under large deformation, the fundamental mechanism of the elastic, plastic flow, strain-softening, and strain re-hardening can apply to epoxy [63].

Other than the molecular structure of the material, the deformation rate, the material temperature, and the hydrostatic pressure can also influence the deformation behaviour of epoxy materials. Normally, for compressive deformation, the nonlinear elastic and plastic regions show strain rate dependence, and higher yield strengths are associated with higher strain rates (Figure 2.10) [54]. The influence of temperature on the deformation response is opposite to that of strain rate, where lower yield strengths are related with higher temperatures (Figure 2.10) [52, 64]. Unlike many crystalline materials in which shear deformations are independent of hydrostatic pressure, the shear stress-strain behaviour of most polymer materials can be significantly affected by their hydrostatic stress [65]. The presence of compressive normal stresses normally increases the elastic modulus and yield strength of the polymer materials (Figure 2.11) [66]. This pressure-dependent behaviour of deformation can be explained as that the compressive pressure can reduce the free volume of the polymer material, thus increasing the resistance to molecular mobility [67].

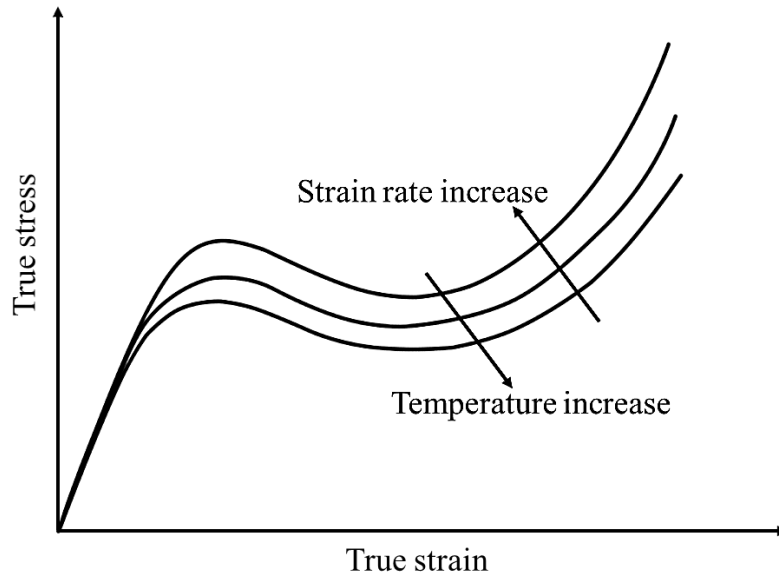


Figure 2.10. Schematic of strain rate and temperature dependent deformation response of glassy polymers under compressive loading.

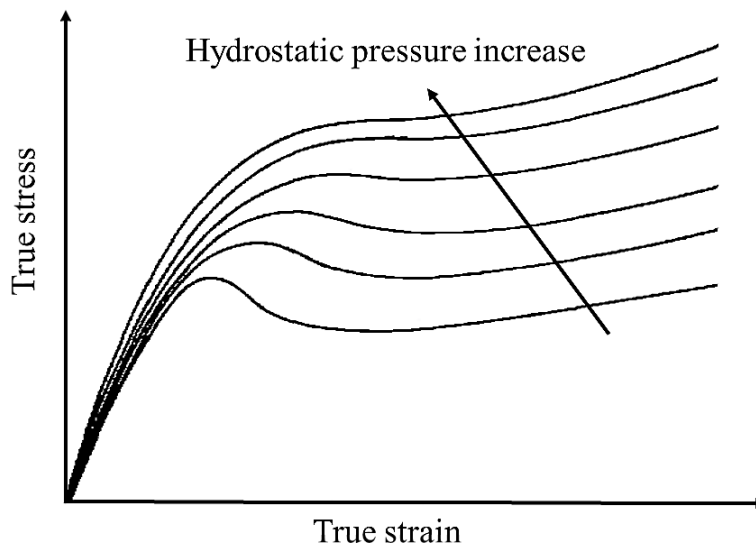


Figure 2.11. Typical stress-strain curves in compression at various pressures for a glassy polymer. Taken and adapted from Pae and Bhateja [66].

There are various test standards available to characterize the properties of cured epoxy materials (Table 2.5). However, those test standards do not provide guidance for characterizing the strain rate, temperature, and hydrostatic pressure dependencies of glass polymers.

Table 2.5. Summary of the test methods for cured epoxy materials.

| Property | | ASTM | ISO and Others |
|---|----------|-------------|------------------------|
| Density | | D792, D1505 | DIN 53479 A, ISO1183-2 |
| Chemical resistance | | D543 | |
| Water absorption | | D570 | ISO 62:2008 |
| Light and water exposure | | D1499 | |
| Glass transition temperature | | D696 | DSC, DMA |
| Coefficient of thermal linear expansion | | D696 | ISO 11359 |
| Coefficient of thermal conductivity | | C177 | ISO/TR 22007 |
| Tension | | D638 | ISO 527 |
| Compression | | D695 | ISO 604 |
| Flexure | | D790 | ISO 178 |
| Impact resistance | | D256 | ISO 179 |
| Fracture toughness | | D5045 | ISO 17281 |
| Flexural fatigue | | D671 | |
| Hardness | Rockwell | D785 | ISO 2039-2 |
| | Barcol | D2583 | |
| | Shore | D1706 | DIN 53505-D |

2.2 Mechanical Characterization of Epoxy Materials under Multiple Loading Rates

Extensive studies have reported the thermal and mechanical properties of various epoxy systems; however, studies related to characterizing the strain rate dependent stress-strain behaviour of snap cured epoxy materials are limited. In this section, the previous research on the characterization techniques and the constitutive modelling of glassy polymers at different strain rates are presented, and the limitations of the previous studies and test methods are summarized.

2.2.1 Mechanical Characterization of the Strain Rate Sensitivity of Epoxy Resins

Since Kolsky's pioneering work on the characterization of the impact response of plastics, there have been many early studies on investigating the mechanical strain rate sensitivity of glassy polymers [68, 69]. Walley et al. [69] reported the compressive response of several glassy polymers (thermoplastics) at a wide range of strain rates, including the strain hardening response at large strains. Walley's compression test results showed that many glassy polymers exhibited a notable strain rate dependence, especially in the plastic deformation region. The early studies of the strain rate sensitivity of glassy polymers were primarily focused on thermoplastic materials due to the earlier development of the structural thermoplastics (e.g., Polymethylmethacrylate (PMMA)) [70]. Over the last 20 years, as the popularity of epoxy materials has increased for structural applications, characterization of the strain rate sensitivity of epoxies has been reported in many studies at strain rates of 10^{-5} to 10^5 s^{-1} (Table 2.6).

Most epoxies exhibit a notable strain-rate dependent mechanical response, including rate dependent elastic modulus, yield strength, and post-yield behaviour [36, 42, 51, 53, 54, 71]. For the same epoxy material, different mechanical responses are observed at different strain rates, where the deformation responses may change from ductile plastic to linear elastic due to the differences in failure strains, particularly when loaded in tension [42, 51, 71]. Additionally, the fracture surfaces of the glassy polymers typically demonstrate brittle fracture at all strain rates [51].

Table 2.6. Summary of some experimental strain-rate sensitivity studies for the glassy polymers.

| Authors | Material and strain rate range(s) | Remarks |
|------------------------|--|--|
| Walley et al. [69] | <ul style="list-style-type: none"> • Tested materials: N6, N66, PC, Noryl, PBT, and PVDF. • Compression strain rates: $10^{-2} - 10^4 \text{ s}^{-1}$. | <ul style="list-style-type: none"> • Strain-rate dependence of the material was observed, with yield strength increasing with strain-rate. • Strength increase laid between 5 -15 MPa per decade increase of strain rate over the range of $10^{-2} - 10^3 \text{ s}^{-1}$. |
| Chen et al. [42] | <ul style="list-style-type: none"> • Tested materials: Epon 828/T-403 epoxy and PMMA. • Compression strain rates: $10^{-5} - 10^4 \text{ s}^{-1}$. • Tensile strain rates: $10^{-4} - 10^3 \text{ s}^{-1}$. | <ul style="list-style-type: none"> • For both tested materials, the strain-rate dependent behavior was significant for both tensile and compressive loading, particular in the plastic deformation regions. • In tension, the specimens deformed in a moderately ductile manner at the quasi-static strain rate and in a linear manner at the dynamic strain rate. |
| Gilat et al. [71] | <ul style="list-style-type: none"> • Tested materials: E-862 and PR-520 epoxies. • Tensile strain rates: $10^{-5} - 10^3 \text{ s}^{-1}$. • Shear strain rates: $10^{-5} - 10^3 \text{ s}^{-1}$. | <ul style="list-style-type: none"> • For both tested materials, the tensile strength at the high strain rate increased approximately 100% from the low strain rate case. • For shear tests, the maximum shear strain for E-862 decreased with increasing strain rate, while the maximum strain for PR-520 remained a constant. |
| Jordan et al. [53] | <ul style="list-style-type: none"> • Tested material: Epon 826/DEA epoxy • Compression strain rates: $10^{-4} - 10^4 \text{ s}^{-1}$. | <ul style="list-style-type: none"> • The compression result revealed a clear strain rate dependence for the plastic region of the material. • There was no notable difference in the elastic region of the material at different strain rates. |
| Gerlach et al. [51] | <ul style="list-style-type: none"> • Tested material: Hexcel RTM-6 epoxy • Compression strain rates: $10^{-2} - 10^4 \text{ s}^{-1}$. • Tensile strain rates: $10^{-3} - 10^4 \text{ s}^{-1}$. | <ul style="list-style-type: none"> • For compression, a noticeable increase of yield and flow stress and elastic modulus were associated with the increasing strain rate. • For tension, a noteworthy increase of failure strength and elastic modulus with the increase of strain rate was reported. |
| Werner and Daniel [54] | <ul style="list-style-type: none"> • Tested material: 3501-6 epoxy. • Compression strain rates: $10^{-5} - 10^3 \text{ s}^{-1}$. • Combined compression and shear strain rates: $10^{-4} - 10^{-1} \text{ s}^{-1}$. | <ul style="list-style-type: none"> • The compressive stress-strain curves showed similar overall shape for all strain rates, and only the nonlinear response exhibited a strain rate dependence. • The yield strength for different strain rates showed a linear logarithmic relation. |
| Tamrakar et al. [36] | <ul style="list-style-type: none"> • Tested material: DER 353 epoxy. • Compression strain rates: $10^{-3} - 10^4 \text{ s}^{-1}$. | <ul style="list-style-type: none"> • The compression test results indicated that a noticeable increase of yield and flow stress was associated with the increase of strain rates, as well as a clear increase for elastic modulus. |

2.2.2 Characterization Techniques for Epoxy Materials across a Wide Range of Strain Rates

Different techniques and apparatus have been used to characterize the response of polymers at different applicable strain rates. A general classification of strain rate regions for material characterization is demonstrated, along with some common test equipment and test conditions (Figure 2.12). As an example, in the work by Walley et al. [69], six different types of thermoplastic (N6, N66, PC, Noryl, PBT, and PVDF) were characterized under compression at the strain rates of 10^{-2} , 10^3 , and 10^4 s^{-1} using three different types of apparatus. A servo-hydraulic mechanical testing machine was used to conduct quasi-static compression tests. High strain rate tests were performed using a custom-built drop weight apparatus that used toughened glass as anvils to enable the high-speed imaging of the axis view of the specimens. A Kolsky or split-Hopkinson bars machine was used for the compression tests at ultra-high strain rates. All tested specimens were cylindrical disks with different thicknesses. After Walley's work, similar characterization apparatus and methods were adopted by several research groups to study the strain rate sensitivity of different types of epoxy resins.

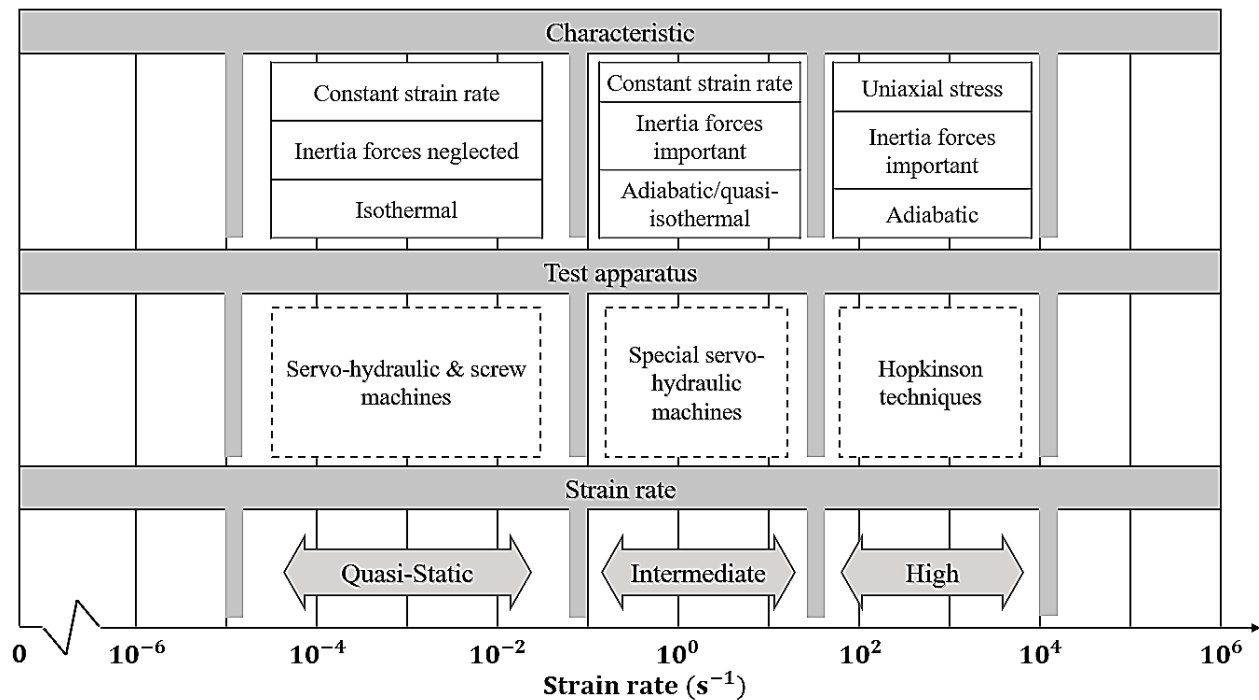


Figure 2.12. Strain rate regions with corresponding test equipment and characteristics. Adapted from Kuhn and Medlin [72].

Based on the test methods and equipment used in the studies listed in Table 2.6, generally accepted methods used to characterize the strain rate dependence of glassy polymers can be deduced. For characterizing the response of epoxies under quasi-static strain rates (i.e., tension, compression and shear at strain rates $< 10^{-1} \text{ s}^{-1}$), commercially available servo-hydraulic and screw-driven testing machines were commonly used. The specimen geometries were typically cylindrical or rectangular dog-bone shape for tensile tests [42, 51, 54, 71], cylindrical or rectangular blocks for compressive tests [36, 42, 51, 53, 54, 69], and hollow cylindrical dog-bone shape for shear tests [54, 71]. The specimen dimensions were determined by the mechanical properties of the tested material as well as the gripping requirements. Characterizing the response of epoxy materials under intermediate strain rates ($10^{-1} - 10^2 \text{ s}^{-1}$) is challenging since the frequency of experimental data acquisition can be close to the natural frequency of the loading device, which may cause signal oscillations [63]. The most widely used testing device has been a closed-loop drop weight hydraulic machine; however, the main issue with drop weight machines was that the inertial effects of the apparatus might influence the results [69, 70]. Long split Hopkinson pressure bars (LSHPB) have also been reported to use for characterizing soft polymers at intermediate strain rates [73]. The geometries of the test specimens for intermediate strain rate tests have often been the same as the quasi-static strain rate tests. Characterizing the response of epoxies at high strain rates ($10^2 - 10^4 \text{ s}^{-1}$) poses the greatest technical challenge. The split Hopkinson Pressure Bar (SHPB) or Kolsky bar has become a widely used testing apparatus for the high strain rate characterization of epoxies and other low impedance materials [36, 42, 51, 53, 54, 69, 71]. A typical SHPB apparatus consists of a transmitter bar, an incident bar, a striker bar, two strain gauges and a high-frequency data acquisition system (Figure 2.13). The two strain gauges located at the center of the transmitter and incident bars are used to record wave propagation during the test. During a SHPB test, the striker bar impacts the end of the incident bar, and the elastic wave generated by the impact propagates along the incident bar (i.e., incident wave). Once the wave reaches the interface of the specimen and incident bar, one part of the wave reflects back along the incident bar (i.e., reflected wave) due to the bar/specimen material and geometric impedance difference. Another part of the wave transmits through the specimen into the transmitter bar (i.e., transmitted wave). The waveforms, amplitude, and timing of the waves are important for analyzing the material stress-strain behaviour (Figure 2.14). However, elastic wave propagation in the bars and tested material can be complex, inertial effects may also be notable, and capturing data at high sampling frequencies may pose additional difficulties [74]. Different techniques were developed to meet the SHPB test requirements and to improve the quality of test results, which are discussed in the subsequent paragraphs.

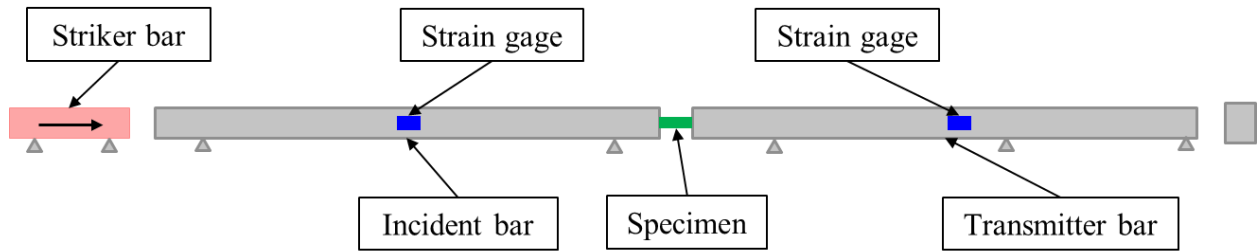


Figure 2.13. Schematic of a typical compressive SHPB apparatus.

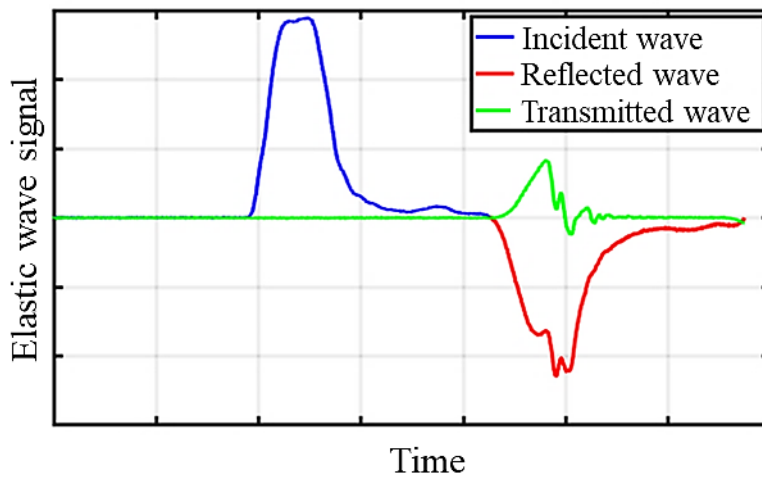


Figure 2.14. Incident, Transmitted and Reflected waveforms for a typical SHPB test.

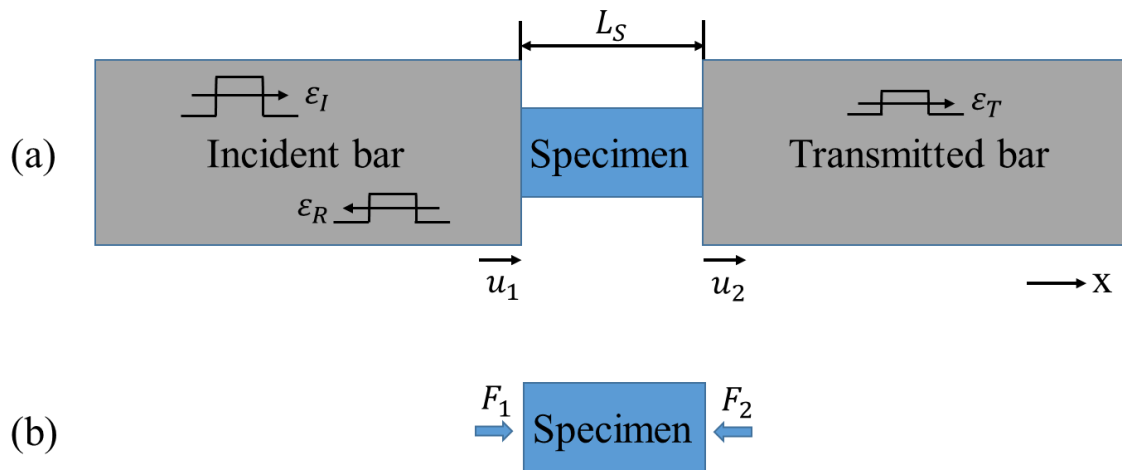


Figure 2.15. Schematic of a compressive SHPB apparatus: (a) elastic waveforms of the bars and bar-end velocities (arrows denoted the direction of the wave transmission and the direction of bar-end velocities); (b) compressive forces acting on the specimen.

During an SHPB test, the strain rate and stress exhibited by the specimen can be determined by analyzing the three elastic waves and employing one-dimensional wave analysis [74]. The forces at the ends of the test specimen are denoted as F_1 and F_2 , while the incident, reflected, and transmitted strains are ε_I , ε_R , and ε_T , respectively (Figure 2.15.). The displacements on specimen ends are expressed as u_1 (incident bar and specimen interface) and u_2 (specimen and transmitted bar interface).

Based on the elastic wave theory [75], the governing wave equation can be written as:

$$\frac{\partial^2 u}{\partial x^2} = \frac{1}{c_b^2} \frac{\partial^2 u}{\partial t^2} \quad (2.2)$$

where x is the position along the bars, t is time and c_b is the elastic longitudinal wave speed along the axis of the bars. The general solution of the incident bar-specimen end displacement can be express as:

$$u_1 = f(x - c_b t) + g(x + c_b t) = u_I + u_R \quad (2.3)$$

Assuming the bars deform under small elastic strains, the one-dimensional strain can be written as:

$$\varepsilon = \frac{\partial u_1}{\partial x} = f' + g' = \varepsilon_I + \varepsilon_R \quad (2.4)$$

The derivative of Equation 2.3 with respect to time yields:

$$\dot{u}_1 = c_b(-f' + g') = c_b(-\varepsilon_I + \varepsilon_R) \quad (2.5)$$

For the transmitted bar, the general solution of the transmitted bar-specimen end displacement can be express as:

$$u_2 = h(x - c_b t) \quad (2.6)$$

The time derivative of the Equation 2.6 yields:

$$\dot{u}_2 = -c_b \varepsilon_T \quad (2.7)$$

The strain rate in the test specimen can be calculated as:

$$\dot{\varepsilon} = \frac{(\dot{u}_1 - \dot{u}_2)}{L_s} = \frac{c_b(-\varepsilon_I + \varepsilon_R + \varepsilon_T)}{L_s} \quad (2.8)$$

Assuming Hooke's Law is valid, the forces at the end of the specimen are defined as:

$$F_1 = A_b E (\varepsilon_I + \varepsilon_R) \quad (2.9)$$

$$F_2 = A_b E \varepsilon_T \quad (2.10)$$

where A_b and E are the cross-sectional area and the elastic modulus of the bars, respectively.

The key assumptions for the SHPB test analysis method is that the test specimen reaches dynamic force equilibrium after an initial transition period and deforms homogeneously. In general, a specimen reaches dynamic equilibrium once the impact wave has time to propagate in the specimen for more than four reflections before failure [76]. Assuming the dynamic force equilibrium is reached, then:

$$F_1 = F_2 \quad (2.11)$$

Substituting Equation 2.9 and Equation 2.10 into Equation 2.11, yields:

$$\varepsilon_I + \varepsilon_R = \varepsilon_T \quad (2.12)$$

Substituting Equation 2.12 into Equation 2.8, the strain rate at time t can now be determined as:

$$\dot{\varepsilon}(t) = \frac{2c_b \varepsilon_R(t)}{L_s} \quad (2.13)$$

The total specimen uniaxial strain at time t can be calculated as the integration of the strain rate over a period of time, and is given by:

$$\varepsilon(t) = \int_0^t \dot{\varepsilon}(t) dt \quad (2.14)$$

Substituting Equation 2.14 into Equation 2.10, the engineering stress of the sample at time t can be calculated as:

$$\sigma_e(t) = \frac{A_b E \varepsilon(t)}{A_s} \quad (2.15)$$

where A_s is the original cross-sectional area of the specimen.

For an incompressible solid where a constant volume under deformation is assumed:

$$A_i L_i = A_s L_s \quad (2.16)$$

where A_i is the instantaneous cross-sectional area of the specimen, and L_i is the instantaneous length. Substituting Equation 2.16 into Equation 2.15, the true stress at time t of the specimen can be expressed as:

$$\sigma_t(t) = \frac{A_b E \varepsilon(t)}{A_i} = \frac{A_b E \varepsilon(t)}{A_s} (1 - \varepsilon(t)) \quad (2.17)$$

The incompressible material assumption allows the calculation of true stress, and Equation 2.17 becomes invalid without this assumption.

For SHPB apparatus, there are many challenges that must be considered. First, the stress wave propagation in the bars can be dispersive, especially for a viscoelastic polymeric bar [77, 78, 79, 80]. Wave dispersion can change the overall shape of the waveform and increase the rise time and the degree of oscillations. Several methods were reported to correct the wave dispersion for SHPB analytically and experimentally [77, 81, 82, 83]. Salisbury [76] developed a method to correct the wave dispersion and attenuation using a spectral method, where a wave dispersion record of the bar was generated by experimental calibration tests (i.e., dynamic calibration of the bar), and the phase shift coefficients of the waveform were determined using the dispersion record and a frequency function. When performing a phase shifting on the actual tests, the experimental strain signal was converted from the time domain into the frequency domain using a Fast Fourier Transform (FFT). Then, the signals were corrected to the right waveform using the shift coefficients and the frequency function. Finally, the modified strain signals used for further calculation were converted back from the frequency domain to the time domain using an inverse FFT. All wave-shift and correction processes can be performed numerically using a custom program or

commercial data processing software. Secondly, the material and geometric impedance differences between the specimen and the bars may result in a low transmitted signal and high reflected signal, which may affect the data accuracy and complicate data processing [78]. Several methods have been used to reduce the low impedance issue, including using additional strain gauges or gauges with high sensitivity [53, 84, 85], modifying the geometry of the bars and specimen [36, 86], pulse-shaping [87, 88], and changing the material of the bars [83, 76, 89]. Furthermore, lubrication between the device and specimen is an important consideration for compression tests, particularly for high strain rate testing of polymers [63]. For polymeric materials, a test specimen with low aspect ratio (L/D) was favoured in previous studies due to the low material strengths and dynamic equilibrium requirement [42, 78]. The result of the low aspect ratio is a large specimen diameter and significant surface friction between the contact areas, which can cause barreling of the specimen [63]. One typical method to lower the frictional force during the SHPB test is to use lubricants [90, 91], such as paraffin wax or petroleum jelly.

2.2.3 Limitations of Previous Epoxy Characterization Studies

As mentioned, the mechanical response of glassy polymers has been widely studied; however, most of the reported studies focused on thermoplastic materials (e.g., PMMA, PC, and PVC). Owing to the recent increase in usage for structural adhesives and composite materials, epoxies have been more widely characterized. Nevertheless, a review of the literature has revealed that two main classes of epoxies have been investigated. Most reported studies focused on characterizing moderately cross-linked epoxies (e.g., EPON and DER), which were based on the widely used DGEBA/F and cured with amine-based hardeners. These epoxies can exhibit ductile behaviour at room temperatures and low strain rate conditions. Few reported studies investigated the response of highly cross-linked epoxies. One example is RTM-6 which is a TGMDA-based epoxy resin developed for the low-volume RTM, particularly for the aerospace industry. These types of epoxies can deform linear elastically at room temperatures and high strain rate conditions.

Snap-cure or rapid curing epoxy systems, which are more suitable for high-volume production environments such as for automobile structures, have not been characterized under dynamic loading conditions. Additionally, in most previous studies epoxy specimens were fabricated in the laboratory, lacking connection to the industrial manufacturing process. Due to the increasing demand for using high-performance composite materials in automotive structures to reduce vehicle weight and improve fuel efficiency and crash performance, there is a need to study the dynamic behaviour of snap-cure epoxy materials and corresponding fiber-reinforced epoxy composites.

2.3 Constitutive Models in Commercial FE Software

Material constitutive models with corresponding material parameters are used in commercial FE software to capture the material behaviour during a simulation (Figure 2.16). A survey of commonly used constitutive models for glassy polymers revealed that the elastic-plastic and viscoelastic-viscoplastic material models were widely used (Table 2.7). In most commercial FE software, integrated material libraries allow users to choose from different constitutive models, where the corresponding material parameters must be defined from material characterization tests. Some common elastic-plastic models and few elastic-viscoplastic models can be found in many integrated material constitutive libraries of commercial FE software. However, in those integrated material constitutive libraries, the available constitutive model sets that are suitable for glassy polymers were limited. Thus, glassy polymers were often modeled with constitutive models originally designed for ductile metallic materials (e.g., elastic-plastic models). Another approach was to develop a customized user-defined material model subroutine (UMAT) as an additional software component to define the behaviour of the glassy polymers.

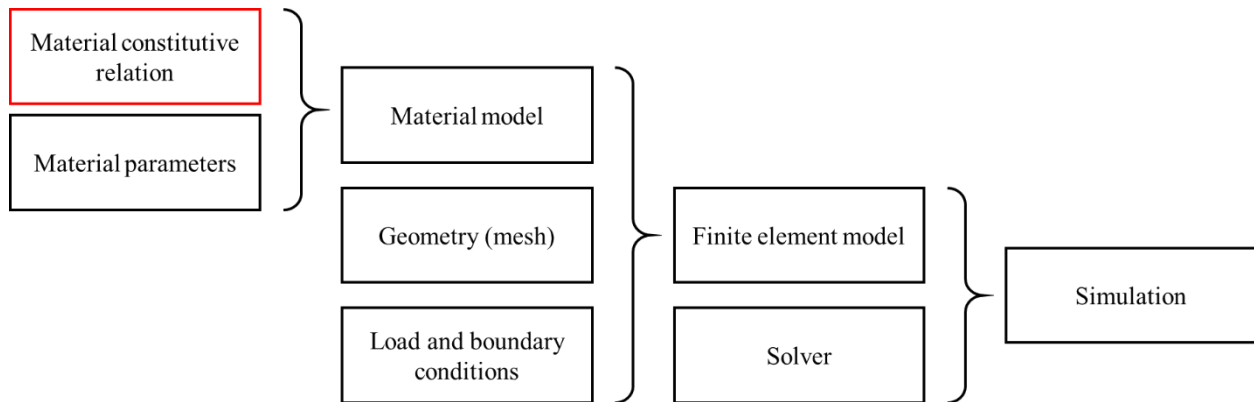


Figure 2.16. The use of a material constitutive model in a commercial FE model

Table 2.7. Survey of common material constitutive models for solid polymers [92].

| Model | Strain-rate effects | Comments |
|------------------------|----------------------------|---|
| Linear elasticity | No | Linear elastic constitutive models can describe the behaviour of most solid polymers under the small strains. In these models, the material deformation is recovered completely upon unloading. |
| Hyper-elasticity | No | Hyper-elastic constitutive models are commonly used for representing large deformations of elastomer-like materials that exhibit nonlinear elastic stress-strain behaviours. The material deformation is recovered completely upon unloading. |
| Linear viscoelasticity | Yes | Linear viscoelastic constitutive models are a combination of linear elastic with linear viscous behaviours, and these models are mainly used for describing the time-dependent stress-strain behaviour of elastomer-like materials (rubber, foam, and soft tissue), and the small strain response of thermoplastic materials. This model may not properly represent the plastic deformation reported for some glassy polymers. |
| Plasticity | Yes | Plasticity constitutive models are used in conjunction with either a linear elastic or equation of state material model. Plasticity models are focused on the non-recoverable deformation of the material, and they are widely used for different types of glassy polymers and metals. When the material is under monotonic loading, the plasticity models with isotropic hardening can capture the deformation response until material failure. However, they have limitations in predicting the nonlinear response of polymers during unloading. Moreover, since plasticity models assume constant elastic modulus, they cannot capture the viscoelastic behaviour of many polymers before yielding. Finally, plasticity models might not be able to describe the strain softening and re-hardening behaviours for polymers under large deformations. |
| Viscoplasticity | Yes | Viscoplastic constitutive models are regarded as the most comprehensive material models for many polymers, and are often used in conjunction with elastic or viscoelastic models. The limitations of these models are that they are not normally integrated within commercial FE software and require users to develop user-defined material models (UMAT). Moreover, extensive experimental data are required to calibrate viscoplastic models, thus they are normally computationally expensive. |

2.3.1 Constitutive Models for Glassy Polymers

As mentioned in the previous section, elastic-plastic and viscoelastic-viscoplastic constitutive models are commonly used to predict the deformation behaviour of glassy polymers. Elastic-plastic models were originally developed for metallic materials and adapted to other materials with similar deformation response, including some glassy polymers. Conversely, viscoelastic-viscoplastic constitutive models were developed primarily for glassy polymers.

The early constitutive relationships for capturing the large deformation of solid polymers was originally proposed by Haward and Thackray [44]. In their study, the deformation of solid polymers was described by two parallel processes: the intermolecular resistance and crosslinking network (Figure 2.9). To model these two processes, an Eyring dashpot in combination with a Hookean spring (Maxwell model) was used to represent the intermolecular resistance, while the crosslinking network was described by a non-linear hyper-elastic network (Langevin spring) (Figure 2.17). The model was originally developed for a glassy thermoplastic polymer, and further extended to glassy polymers.

In 1988, Boyce, Parks and Argon [64] extended the original one-dimensional model into a three-dimensional model (known as the BPA model) and simulated the response of PMMA. In this model, instead of using the original Eyring's equation, a micro-mechanical model developed by Argon [48] that extended the effects of strain rate, pressure sensitivity of yielding, true strain softening, and temperature was used to describe the intermolecular resistance on the plastic region. The original crosslinking network or entropic resistance part of the model was represented with the Langevin spring; however, the one-dimensional Langevin spring was extended into a three-dimensional three-chain model.

In 1993, Arruda and Boyce [93] improved the BPA model, using an eight-chain rubber elastic model to replace the original three-chain model. Later the same year, Wu and Van der Giessen [94] proposed a more realistic full network model, using a Chain Orientation Distribution Function to describe the random distribution of the macromolecular network.

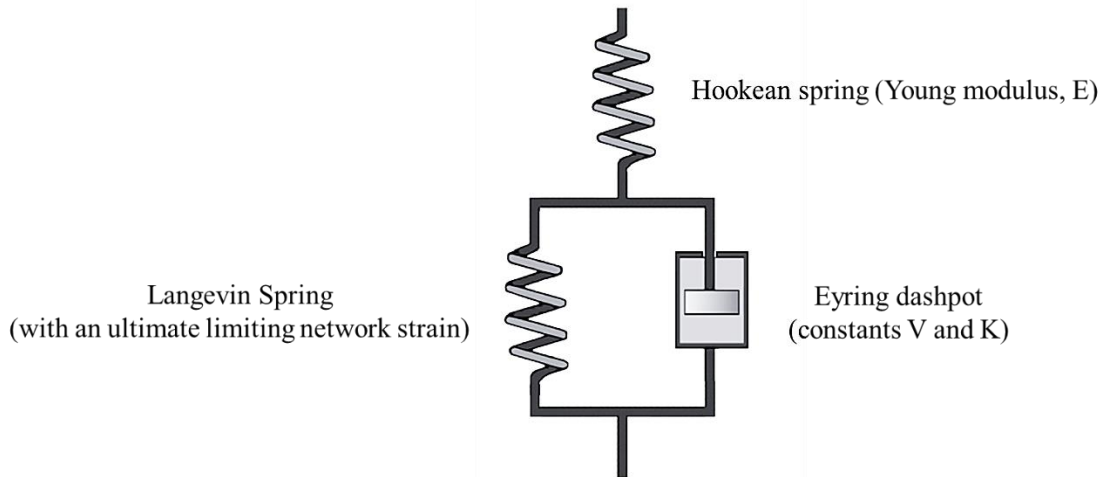


Figure 2.17. A semi-empirical and one-dimensional elastic-viscoplastic model for glassy polymers. Adapted from Haward and Thackray [44].

After the early development of the BPA model, the subsequent studies continuously improved or refined the BPA model to better capture the important features of glassy polymers for different applications. Figure 2.18. shows an overview of the developed finite-strain viscoelastic-viscoplastic models for glassy polymers. Two research groups made notable contributions on the development of these models. The group at MIT led by Boyce and Lallit originally developed the BPA model and reported continual improvements to the model. The research group in Eindhoven led by Tervoort [95] modified the original BPA model and added a linear relaxation time spectrum to better describe the pre-peak yield behaviour of glassy polymers. This model was improved over the years and named Eindhoven Glassy Polymer (EGP) model.

Other than the well-known BPA model, few models were developed that can represent the viscoplastic behaviour of glassy polymers. The viscoplastic model proposed by Goldberg in 2001 [96] was developed based on the Bodner-Partom model [97], which is a viscoplastic state variable model original developed for the viscoplastic deformation of metals at elevated temperatures. The Goldberg model was developed specifically for epoxy resins used in composite materials, and can accurately capture the viscoplastic behaviour in the small to intermediate strain range. The Goldberg model requires nine material parameters, which is much less than some BPA models where thirty or more parameters are required.

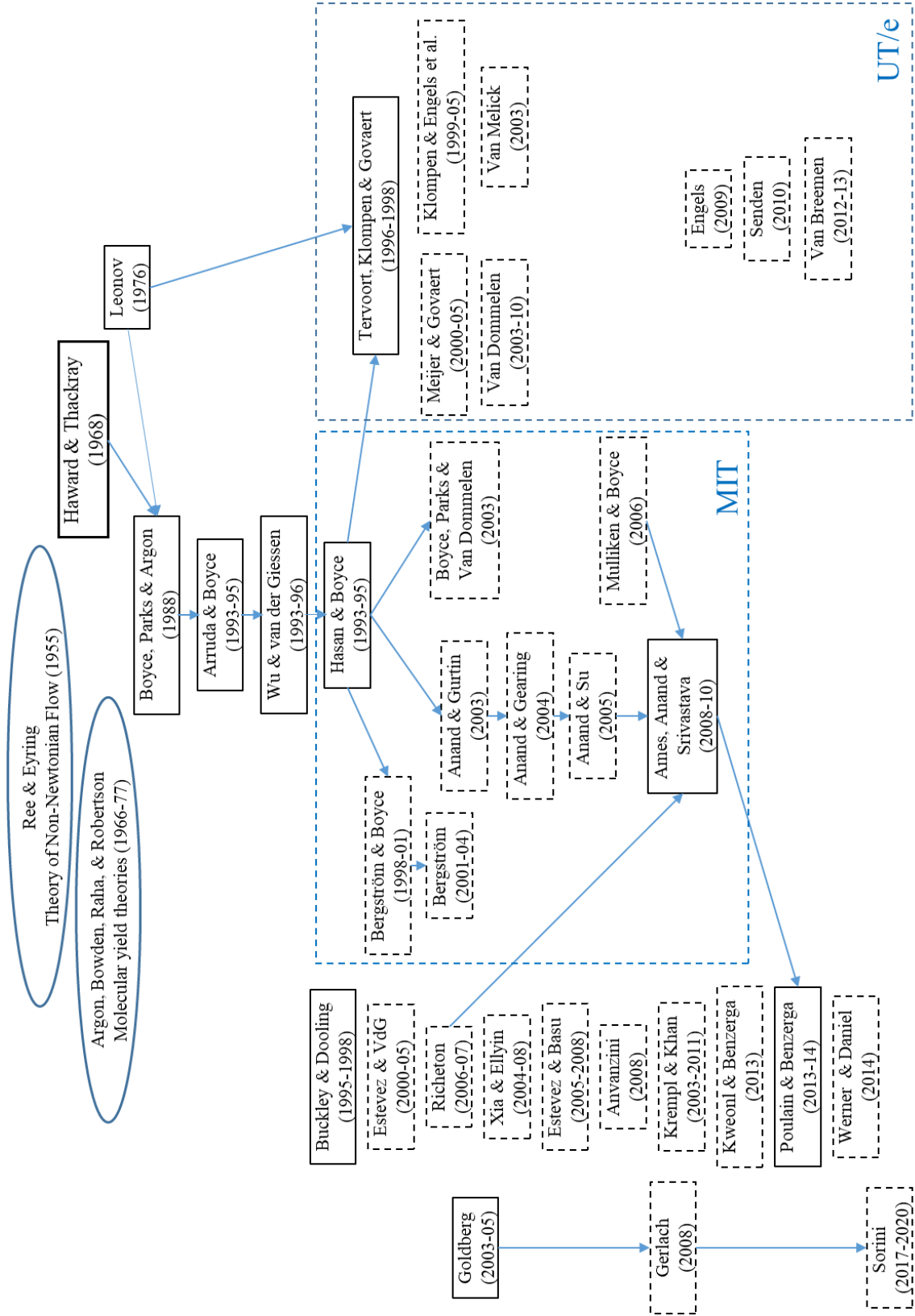


Figure 2.18. Overview of previously developed constitutive models for glassy polymers [10].

Another approach used to model the constitutive behaviour of glassy polymers was to adopt and modify the concept of classical metal plasticity for glassy polymers. Classical metal plasticity models are incremental in nature and decompose strain into elastic and plastic parts [98]. The elastic response is assumed to be constant for different loading conditions, while the plastic response is formulated based on three main elements, namely a yield criterion, flow rule and hardening law.

The yield criterion of a material describes the limits of elastic deformation through a yield surface in the principal stress space. For classical metal plasticity, either the Mises or Hill yield criterion can be used. The Mises yield criterion is often used for isotropic materials (such as the epoxy in this study), while the Hill yield surface is used for anisotropic materials. In the Mises yield criterion, the equivalent stress ($\bar{\sigma}$) is expressed as

$$\bar{\sigma} = \sqrt{3J_2} = \sqrt{\frac{3}{2}S_{ij}S_{ij}} = \sqrt{\frac{(\sigma_{11}-\sigma_{22})^2+(\sigma_{22}-\sigma_{33})^2+(\sigma_{33}-\sigma_{11})^2+6(\sigma_{12}^2+\sigma_{23}^2+\sigma_{31}^2)}{2}} \quad (2.18)$$

where J_2 is the second invariant of the deviatoric stress tensor and S_{ij} are the components of the deviatoric stress tensor [99]. As shown in Equation 2.18, the Mises yield criterion is insensitive to hydrostatic pressure, which is known to influence the yield threshold for glassy polymers [66]. Two commonly used pressure dependent yield criteria, the Drucker-Prager criterion [100] and the Mohr-Coulomb criterion, allow the plastic constitutive models to capture the asymmetric yield behaviours of glassy polymers between tension and compression.

The flow rule or plastic flow rule is used to describe the relationship between the strain increment and deviatoric stress tensor for the plastic behaviour of materials [101].

$$d\varepsilon_{ij}^p = d\lambda S_{ij} = d\lambda G_{ij} = d\lambda \frac{\partial g}{\partial \sigma_{ij}} \quad (2.19)$$

Here, λ is a plastic multiplier, G_{ij} is a function of stresses and g is a scalar function (plastic potential) which gives the plastic strains when it differentiated with respect to the stresses. Flow rules can either be associated and non-associated. Associated plastic flow rules assume that the plastic potential (g) is equal to the yield function (i.e., the flow rule associates with the yield function), and were normally used for the classical metal plasticity models incorporated with Mises or Tresca yield criterion [102]. Associated plastic flow

rules assume that the increment of plastic strain is in a direction normal to the yield surface, and the plastic potential (g) is different from the yield function [103].

The hardening rule describes the evolution of the material yield surface during the material strain hardening process. In plasticity theory, if the resulting stress on the material is greater than its yield strength, plastic deformation occurs and the material hardens [101]. The hardening behaviours of a material can be depended on the strain rate and temperature.

Elastic-plastic constitutive models for glassy polymers were used in many micromechanical analyses of fiber-reinforced composite materials. Gonzalez and LLorca [104] treated the glassy polymer as an isotropic, thermo-elastic-plastic solid within a representative volume element (RVE), and the Mohr-Coulomb yield criterion was used. Canal et al. [105] modeled an epoxy with a plasticity model, and the pressure-sensitivity, strain softening and strain re-hardening behaviours were described by the Drucker–Prager’s yield criterion. Totry et al. [106] used a similar approach as Gonzalez and LLorca, where an epoxy was modeled as an isotropic and elastic-plastic material with the Mohr–Coulomb criterion. Melro et al. [107] modeled an epoxy using an elastic-plastic constitutive model, in which the parabolic yield criterion developed by Tschoegl [108] was used with a non-associative flow rule to define the volumetric deformation of plasticity. A hardening law that considered both tensile and compressive yield strengths by a piece-wise function was developed for the model. Bai et al. [109], proposed a complex modified elastic-plastic constitutive model to capture the phenomenological thermo-visco-plastic hardening behaviours of epoxies. In the model, a modified paraboloid yield criterion that introduced the third deviatoric stress invariant and two dependent parameters was proposed. A non-associative flow rule was adopted from Melro’s study [107]. The hardening law accounted for the strain rate and temperature dependencies by scaling the compressive, tensile and shear yield strengths using a linear logarithmic increment relation. Morelle et al. [40] described a high cross-linked epoxy as an isotropic elastic-plastic material with the strain rate and temperature dependencies using an available material model in Abaqus with a linear Drucker–Prager yield criterion.

2.3.2 Limitation of Developed Epoxy Constitutive Models

Many constitutive models for glassy polymers that are able to predict the strain rate, temperature, and hydrostatic pressure dependencies of epoxy have been proposed. Viscoelastic-viscoplastic constitutive models are regarded as the most comprehensive and accurate material models for many polymers, including epoxies. However, most viscoelastic-viscoplastic constitutive models for cured epoxy require the development of a user-defined material subroutine (UMAT), which is difficult and regarded as a limitation.

Moreover, these models normally require substantial experimental data to calibrate all the material parameters. Finally, the computational expenses for those models were normally very high, which is unfavourable for the load-intensive micromechanical analysis of composites. On the other hand, elastic-plastic constitutive models have been frequently used for modeling the response of the matrix phase in micromechanical analysis of composites. Few studies have used the available constitutive models in general-purpose finite element software to predict the strain rate dependence of epoxy, particularly for the micromechanical analysis of composites.

Chapter 3 Experimental Methods

In this chapter, details of the investigated snap-cured epoxy material, the methods of test sample preparation, and the techniques used for the mechanical characterization are presented.

3.1 Epoxy Material

In this study, a rapid curing (snap-cured) low viscosity epoxy system designed for mass-production of FRP structural components, EPIKOTE™ 06150 (Hexion Inc.), was investigated. The epoxy system was comprised of three components (Table 3.1), hereafter referred to as the resin, curing agent, and internal mold release. The polymerized resin and curing agent contained blends of bisphenol-based glycidyl ethers and aliphatic amine hardeners, respectively, which are suitable for high-volume rapid processes like high pressure-resin transfer molding (HP-RTM) [110]. The supplier provided quasi-static properties of the cured neat epoxy system were used as an initial guideline for this research (Table 3.2).

Table 3.1. EPIKOTE™ 06150 epoxy system (Hexion Inc.) [111].

| Component | Density (g/cm ³) | Viscosity at 25°C (mPa · s) (Method: DIN 53015) | Description |
|-------------------------------------|------------------------------|---|--|
| EPIKOTE™ Resin TRAC 06150 | 1.17 | 8,000 – 10,000 | A medium viscosity epoxy resin |
| EPIKURE™ Curing Agent TRAC 06150 | 0.97 | 10 - 20 | A low viscosity amine hardener |
| HELOXY™ Additive TRAC 06805 | 1.01 | 750 ± 450 | A silicone- and wax-free internal mold release agent |

Table 3.2. Reported properties of cured EPIKOTE™ 06150 epoxy material (Hexion Inc.) [111].

| Properties | Value | Test method |
|--|-------------------|--|
| Density (kg/L) | 1.151 – 1.155 | DIN 53479 A at 23°C |
| Glass transition temperature (T_g) (°C) | Onset: 118 ± 2 | DSC (10K/minute) |
| | Midpoint: 124 ± 2 | |
| | Onset: 118 ± 2 | DMA |
| | Peak: 136 ± 2 | |
| Tensile strength (MPa) | 85 ± 5 | DIN EN ISO 527-1 at Room temperature (RT) |
| Tensile modulus (GPa) | 2.9 ± 0.1 | |
| Elongation at break | 6 – 8 % | |
| Flexural strength (MPa) | 130 ± 5 | DIN EN ISO 178 at RT |
| Flexural modulus (GPa) | 3.0 ± 0.1 | |
| Fracture toughness (MPa√m) | 0.75 ± 0.05 | ISO 17281 at RT |
| Fracture energy (J/m ²) | 225 ± 5 | |
| Thermal expansion coefficient (ppm/°C) | < 75 | ISO 11359-2 |
| Total shrinkage (Vol. %) | < 4 | Calculated DIN 16945 at RT |
| Hardness (Shore D) | 85 – 86 | DIN 53505-D at RT |

3.2 Material Processing

Owing to the different test methods that were used to characterize the mechanical properties of the cured epoxy material over a range of strain rates in tension, compression and shear, different sample sizes and specimen geometries were required (Section 3.3). Therefore, two processes were used to manufacture the epoxy material into flat panels and cylindrical samples, namely HP-RTM and a hand-cast method, respectively.

3.2.1 HP-RTM Panel Processing

In this study, an HP-RTM process was used to fabricate thin flat panels that were required to fabricate the tensile and shear test specimens (see Sections 3.3.2 and 3.3.3). HP-RTM is a fabrication process that is typically used for fiber-reinforced plastic components [112]. In general, the process incorporates a metering unit that rapidly mixes the different parts of a highly reactive epoxy system at the mold injection point using an integrated mixing head. The mixture is injected into a closed two-part mold under a high flow rate, which in turn generates high pressure in the sealed mold cavity (Figure 3.1).

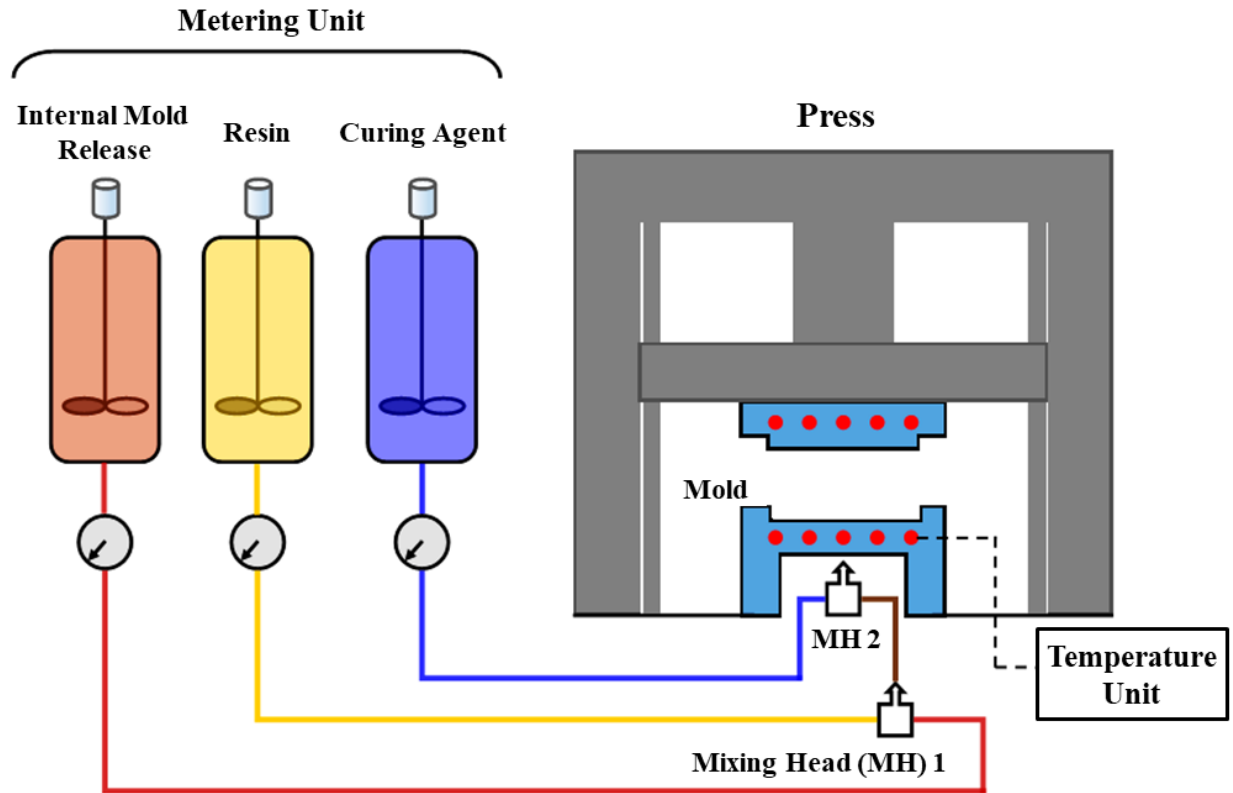


Figure 3.1. Schematic of a typical HP-RTM process.

Table 3.3. Epoxy system part composition and conditioning parameters for the HP-RTM metering unit.

| Name | Part composition by weight (measured) | Temperature (°C) | Diameters of orifices in the mix head (mm) |
|----------------------------------|---------------------------------------|------------------|--|
| EPIKOTE™ TRAC 06150 Resin | 100 (98.81) | 60 | 0.8 |
| EPIKURE™ TRAC 06150 Curing agent | 24 (23.72) | 35 | 0.6 |
| HELOXY™ TRAC 06805 Additive | 1.2 (1.19) | 35 | N/A |

In this research, flat panels of the epoxy system (nominally 4 mm-thick and 900 mm x 550 mm in size) were fabricated using a full-scale HP-RTM setup at the Fraunhofer Project Center for Composites Research (FPC) at Western University (Figure 3.2). During the panel fabrication process, the resin, curing agent, and

internal mold release were heated up to a desirable temperature and recirculated at a pressure of 120 bar in a high flow metering unit (Table 3.3). The elevated temperature reduced the resin viscosity and the thermal shock when the mixture entered the pre-heated mold. After the preprocessing step, the three parts of the epoxy-system were injected through a mixing head into a closed two-part sealed mold, held at a constant temperature of 120°C. A 25,000 kN hydraulic press (DIEFFENBACHER) imposed a 1,000 kN force on the mold during the resin injection, and a 3,000 kN force during the subsequent 5-minute curing cycle. The force profile for the hydraulic press are shown in Table 3.4. A vacuum was used to remove air from the sealed mold before the resin was injected to minimize void content and improve the cured epoxy panel quality.

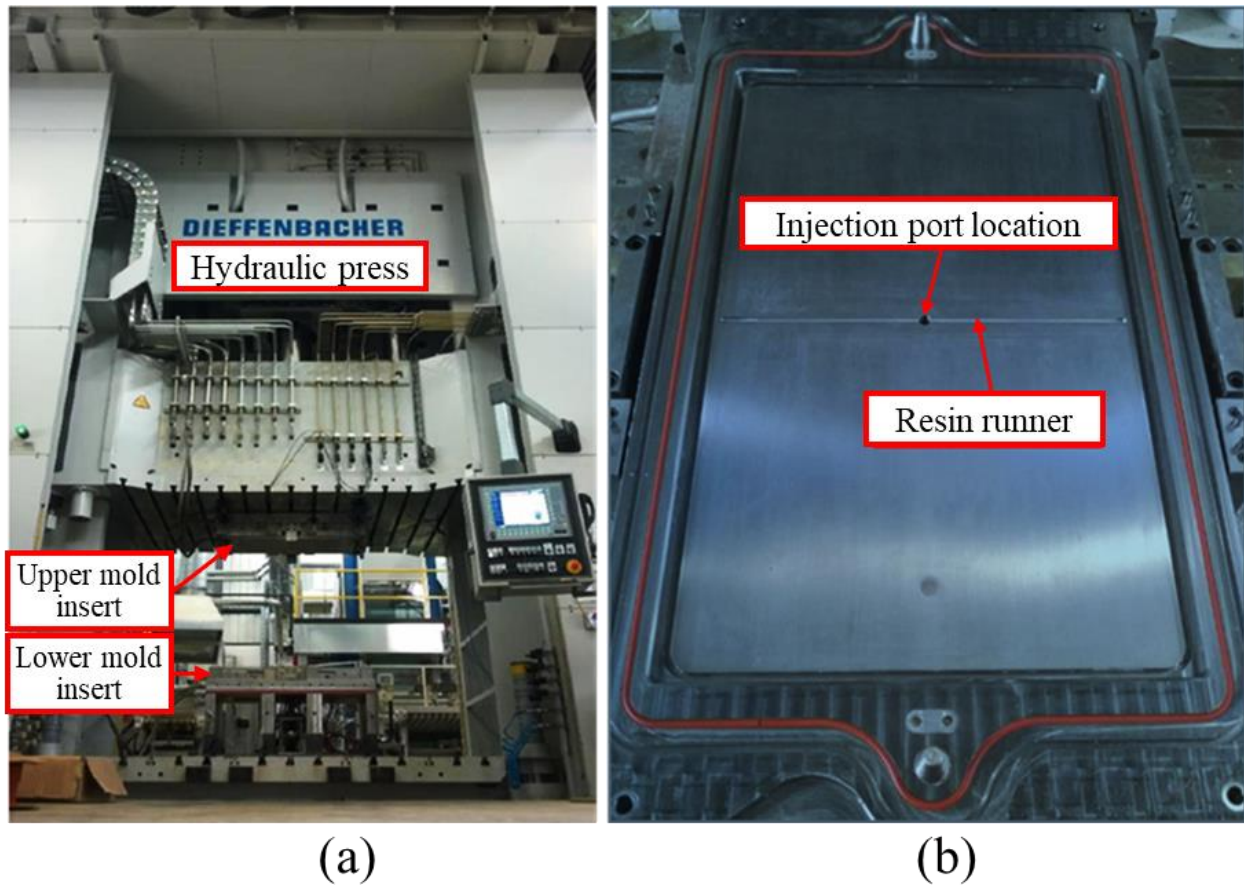


Figure 3.2. Images of the HP-RTM setup: (a) the hydraulic press along with the main tooling base, and (b) the lower mold insert.

Table 3.4. The force profile of the hydraulic press and the mold temperature used for fabricating the neat epoxy panel.

| Time (s) | Mold temperature (°C) | Press Force (kN) | Comment |
|----------|-----------------------|------------------|------------------------------|
| 0 | 120 | 1,500 | Start of the force profile |
| 2 | 120 | 500 | Vacuum start |
| 60 | 120 | 500 | Vacuum end / Injection start |
| 62 | 120 | 1,000 | Injection end |
| 68 | 120 | 3,000 | Curing start |
| 366 | 120 | 3,000 | Curing end |
| 368 | 120 | 0 | End of the force profile |

Panel dimension: 900 mm × 550 mm

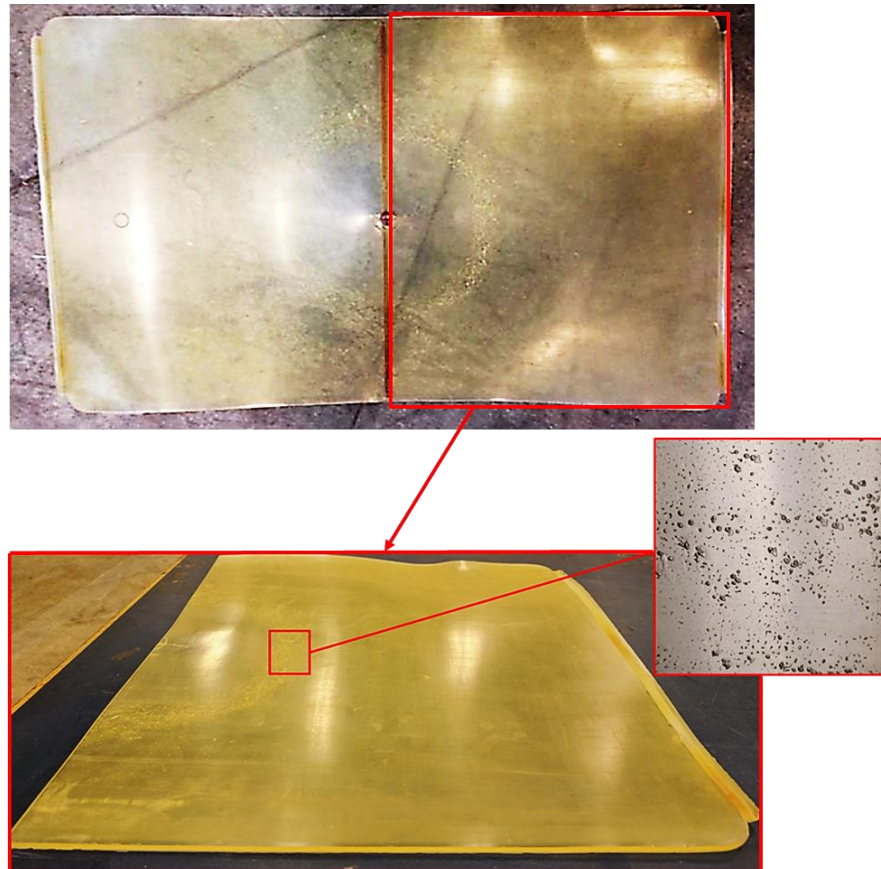


Figure 3.3. Epoxy panel manufactured using the HP-RTM setup (top), and half panel where edge curvature and porosity are observed (bottom).

After curing, the epoxy panels were removed from the hot mold and allowed to cool under ambient conditions, which resulted in slight curvature at their edges. Moreover, there was visible porosity distributed around the center section of the panel where the resin was injected into the mold (Figure 3.3). Consequently, the center portion of the panel that contained porosity was removed, and then the curved pieces were flattened before machining the test specimens. First, the cured epoxy panels were softened in an air-circulated oven by applying heat at a rate of 5 °C/min from ambient temperature to 120 °C (i.e., the glass transition region of the epoxy material). After 5 minutes of dwelling at 120 °C (soak time), the hot panels were removed and placed between two heavy flat steel plates for flattening while they cooled to ambient temperature. The flatness of the panel was visibly improved after this process (Figure 3.4). The quasi-static tensile tests conducted using specimens extracted from these flat panels were compared with the corresponding test results provided by the manufacturer to investigate the influence of the panel flattening on the mechanical responses of the epoxy material.

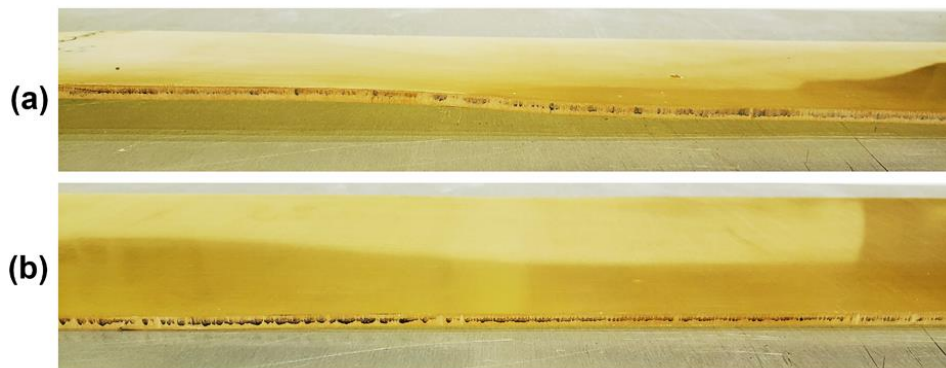


Figure 3.4. Edge view of a neat epoxy panel fabricated using the HP-RTM setup: (a) after demolding and prior to flattening (b) after flattening.

3.2.2 Hand Cast Cylindrical Sample Processing

Compression and high strain rate tensile tests required thicker sample geometries that were not achievable using the HP-RTM process. Therefore, solid cylindrical epoxy samples ($\emptyset 16 \times 55$ mm) were cast by hand-mixing and open-air molding using a custom-built mold. The mold was comprised of three parts, including a base and two mold bodies (Figure 3.5). Each part of the mold was held by bolts when casting the samples to allow for ease of disassembling and sample demolding. The mixing and curing procedures used for the epoxy samples were as follows:

1. The resin and the internal mold release agent were mixed in a disposable plastic cup with a ratio of 100:1.2 by weight. A minimum of 100 g of resin was used to minimize the potential for inaccurate mixing ratio.
2. The mixture in step 1 was heated to 40°C in an air-circulated oven, and held at this temperature for 2 to 3 hours. This step was aimed to lower the mixture viscosity and extract air while not affecting the pot life of the resin. At the same time, a metal mold (Figure 3.5) that was coated with mold release spray (LOCTITE 700-NC) was heated to 40 °C in the oven.
3. The curing agent was added to the mixture from step 2 with a ratio of 101.2:24 by weight. The mixing process was completed in under 3 minutes to minimize porosity and maximize pot life.
4. The mixture in step 3 was injected into the preheated metal mold using a disposable plastic syringe.
5. The mixture and mold were heated to 80°C at a maximum rate of 5°C/min, and allowed to dwell at 80°C for 20 minutes.
6. The hot mold was removed from the oven and allowed to cool down to room temperature in ambient conditions.
7. Finally, the cured hand-cast samples were demolded by disassembling the custom mold (Figure 3.6).

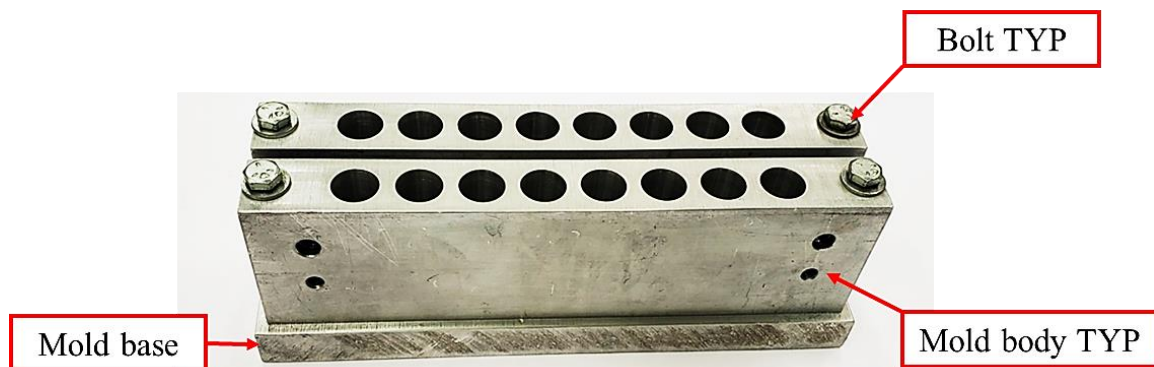


Figure 3.5. Custom-designed mold to manufacture the hand-cast samples.



Figure 3.6. A hand-cast neat epoxy cylinder.

3.3 Test Specimen Preparation

The epoxy test specimens used in this study were machined from either the cured HP-RTM panels or the hand-cast cylinders. Overall, six types of epoxy specimens were used for thirteen sets of material characterization tests, including dynamic mechanical analysis (DMA), tensile, shear, and compression tests.

3.3.1 Test Specimen for Dynamic Mechanical Analysis (DMA)

Rectangular specimens were used for the three-point flexural DMA tests (Figure 3.7), and their dimensions were selected based on recommendation from the user manual of the DMA test machine. The hand-cast specimens were machined from the hand-casted cylinders, while the HP-RTM specimens were extracted from different locations on the fabricated HP-RTM panels. Both the hand-cast samples and the HP-RTM samples were machined by a universal milling machine (First LC1-1/2VS), and the machining tools and parameters used are listed for reference (Table 3.5).

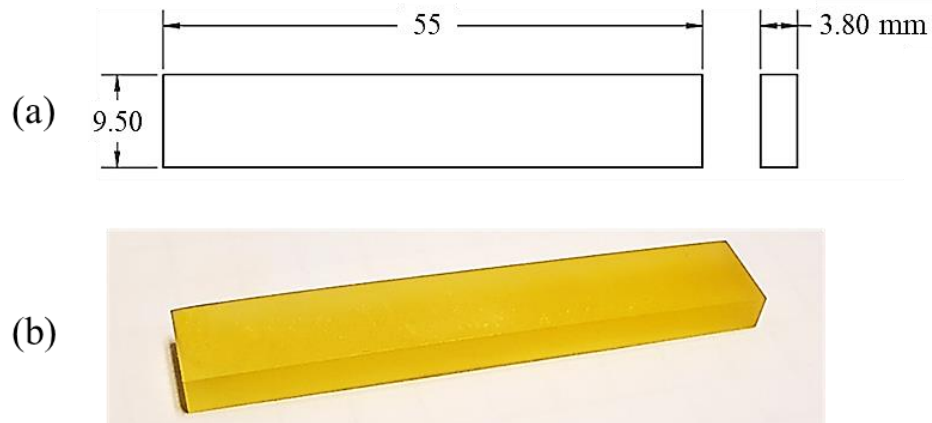


Figure 3.7. DMA test specimen: (a) dimensions, and (b) image.

Table 3.5. Summary of tools used and machining parameters for the DMA specimens.

| Tool | Spindle speed (RPM) | Feed rate | Cooling |
|---|---------------------|-----------------------|---------|
| Ø3/4" Replaceable carbide-insert end mill | 1,500 | Manual (slow) | Air |
| Ø1/4" End mill | 1,000 | Manual (intermediate) | Air |

3.3.2 Quasi-Static and Intermediate Strain Rate Uniaxial Tension Test Specimen

The ASTM International test standard ASTM - D638 provides a detailed guideline for the characterization of the tensile properties of plastics, including material preparation, specimen geometries, test apparatus, testing speeds, data processing, etc. However, one limitation of ASTM D638 is that it specifies testing guidelines for high quasi-static to low-intermediate strain rates ($0.1 \leq \dot{\epsilon} \leq 10 \text{ s}^{-1}$) test conditions. Thus, it may not be suitable for low quasi-static ($\dot{\epsilon} < 0.01 \text{ s}^{-1}$) and high-intermediate ($10 < \dot{\epsilon} < 100 \text{ s}^{-1}$) strain rates. Accordingly, a modified dog-bone shaped specimen geometry that can be used for tension tests at a wide range of strain rates was adopted in this study. The specimens were machined from the fabricated HP-RTM panels and used for quasi-static and intermediate strain rate tensile tests (Figure 3.8). A previous study compared the quasi-static tensile response of the proposed dog-bone geometry with that recommended by ASTM-D638 (type V), and a good agreement was reported [113]. Thus, the proposed geometry was deemed suitable for characterizing the tensile properties of the investigated epoxy. The gauge width of the specimens used in this study was 3 mm for the quasi-static strain rate and 2 mm for the intermediate strain rate. A custom fixture was designed and manufactured for the machining of the tension test specimens (Figure 3.9). A rough-cut flat epoxy sample with two pre-drill holes was held by the screws in the fixture, while a universal milling machine (First LC1-1/2VS) was used to machine the final dimensions of the dog-bone specimens. The machining tools and machining parameters used are listed for reference (Table 3.6).

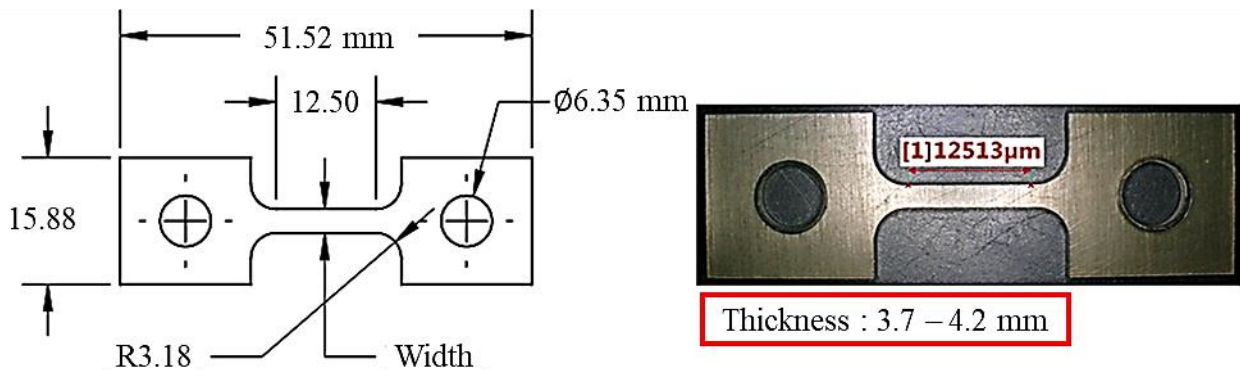


Figure 3.8. The dog-bone specimen dimensions for uniaxial tension tests at quasi-static and intermediate strain rates [113].

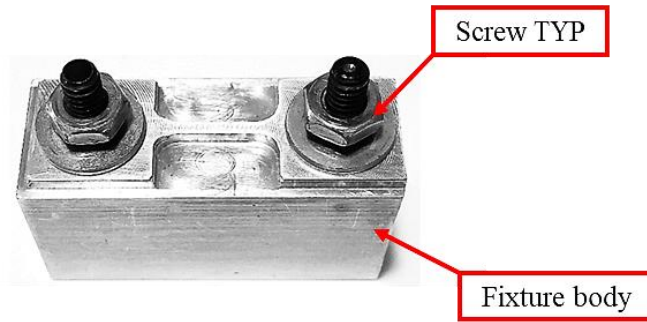


Figure 3.9. The custom fixture for machining dog-bone tension specimens.

Table 3.6. Summary of tools and machining parameters used for the quasi-static and intermediate strain rate tensile specimens.

| Tool | Spindle speed (RPM) | Feed rate | Cooling |
|-----------------|---------------------|-----------------------|---------|
| Ø1/4" Drill bit | 5,00 | Manual (intermediate) | Air |
| Ø1/4" End mill | 1,000 | Manual (intermediate) | Air |

3.3.3 Quasi-Static and Intermediate Strain Rate Uniaxial Shear Test Specimen

There are currently no testing standards designed for characterizing the shear properties of plastics using uniaxial tests. Thus, the geometry of the uniaxial shear specimens was adopted from a novel specimen geometry originally designed for shear tests of metallic alloys under static and dynamic loading [114]. Preliminary tests were conducted to measure the strain field on the surface of the epoxy test specimens, and the final geometry was chosen to ensure that a pure shear strain state was exhibited at the specimen center (Figure 3.10). The shear specimens were extracted from the HP-RTM panels and machined by a computer numerical control (CNC) vertical machining center (HASS VF4 VOP-D). The machining tools and machining parameters are listed for reference (Table 3.7).

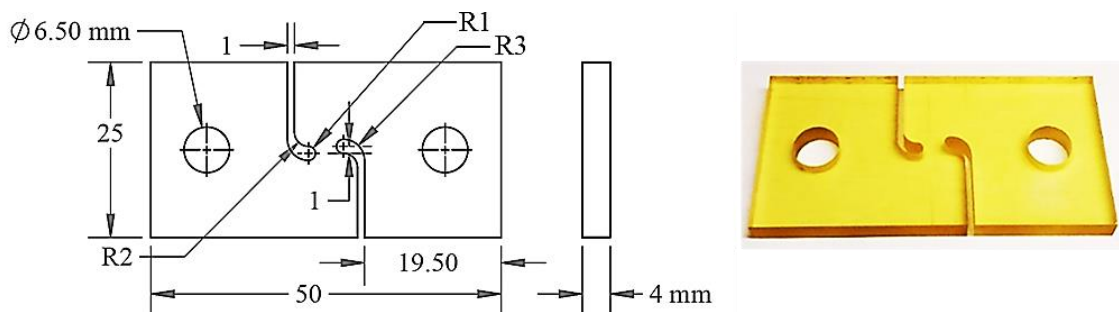


Figure 3.10. The specimen for uniaxial shear tests at quasi-static and intermediate strain rates.

Table 3.7. Summary of tools and parameters used for the CNC machining of quasi-static and intermediate strain rate shear specimens.

| Tool | Spindle speed (RPM) | Feed rate (IPM) | Depth of cut | Cooling |
|-----------------|---------------------|-----------------|--------------|---------|
| Ø1/32" End mill | 4,000 | 1 | 1 x Dia. | coolant |
| Ø1/4" End mill | 2,000 | 3 | 1 x Dia. | coolant |

3.3.4 Quasi-static and Intermediate Uniaxial Compression Test Specimen

ASTM International testing standard ASTM - D695 provides guidelines for characterizing the compression properties of plastics under quasi-static loading, including specimen geometries, test apparatus, loading speeds, test procedure, data processing, etc. This standard was followed in this study; however, several improvements were made to overcome the challenges of specimen buckling and barreling. ASTM-D695 recommends a right cylinder or prism specimen with the length being twice the principal width or diameter, where a 12.7 mm in diameter by 25.4 mm in length cylindrical specimen is preferred. However, preliminary testing revealed that this recommended specimen geometry led to specimen buckling. After several trial tests, a right cylindrical specimen with its length the same as its principal diameter was selected as the final compression specimen geometry (Figure 3.11). The compression specimens were machined from hand-cast cylinders using an engine lathe (Microweily ty-1630s). The machining tools and machining parameters are listed for reference (Table 3.8).

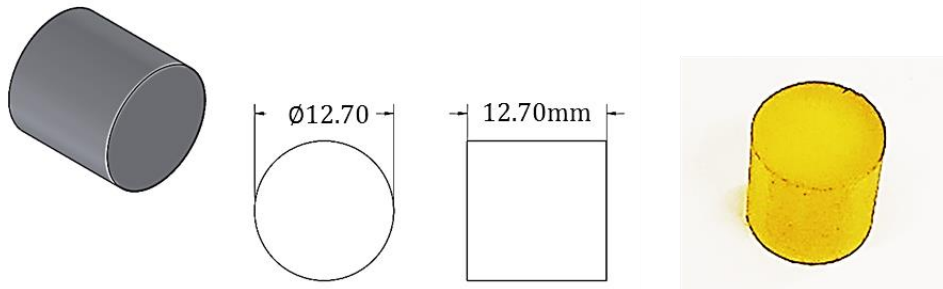


Figure 3.11. The specimen for compression tests at quasi-static and intermediate strain rates.

Table 3.8. Summary of tools and machining parameters used for the quasi-static and intermediate strain-rate compression specimens.

| Tool | Spindle speed (RPM) | Feed rate | Cooling |
|------------------------------------|---------------------|-----------------------|---------|
| RH Turning/Facing with CCMT insert | 700 | Manual (slow) | Air |
| Ø1/4" Center drill bit | 700 | Manual (intermediate) | Air |

3.3.5 Tensile Polymeric Split-Hopkinson Pressure Bar (T-PSHPB) Test Specimen

Since there are currently no standard high strain-rate test methods for polymers, the specimen geometry was developed iteratively based on the test material, T-PSHPB apparatus, and the target strain rate. The modified dog-bone specimens used for the quasi-static and intermediate strain rate tensile tests (Figure 3.8) were not suitable for high strain rate testing due to the loose connection and failure at the pin hole locations. Thus, the T-PSHPB specimens used in this study had a cylindrical dumbbell-shaped geometry with right-hand threads and left-hand threads on both ends (Figure 3.12). The gauge dimensions of the specimen were determined iteratively, and several factors were considered when designing the specimen:

1. Minimizing radial and longitudinal inertia
2. Minimizing stress concentrations at the fillets
3. Achieving specimen dynamic equilibrium during the test
4. Ensuring a tight fit between the specimen and bars.
5. Limiting the stress in the bars within the elastic stress limit

The SHTB specimens were machined from hand-cast samples using an engine lathe (Microweily ty-1630s). The machining tools and parameters used are listed for reference (Table 3.9). In order to mount the specimens to the polymer bars firmly, a tapered thread clamping fixture was developed and fabricated (Figure 3.13). The clamping fixture includes four parts: one RH connector (connected to the RH male thread side of the specimen), one LH connector (connected to the LH male thread side of the specimen), and two RH female thread rings.

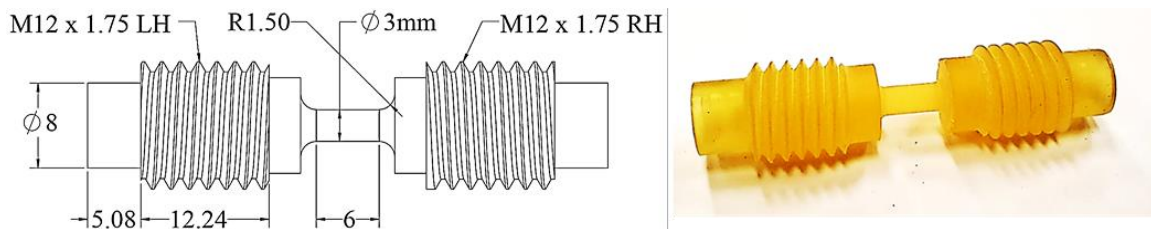


Figure 3.12. The specimen and dimensions for the T-PSHPB tests.

Table 3.9. Summary of tools used and machining parameters for the SHTB specimens.

| Tool | Spindle speed (RPM) | Feed rate | Cooling |
|---------------------------------------|--|-----------------------|---------|
| RH Turning/Facing with CCMT insert | 700 | Manual (slow) | Air |
| Ø1/4" Center drill bit | 700 | Manual (intermediate) | Air |
| RH OD Threading with 16ER AG60 insert | Thread speed setting: BSW8 Direction: LH and RH | | Air |
| RH Grooving with MRMN-3 insert | 700 | Manual (slow) | Air |

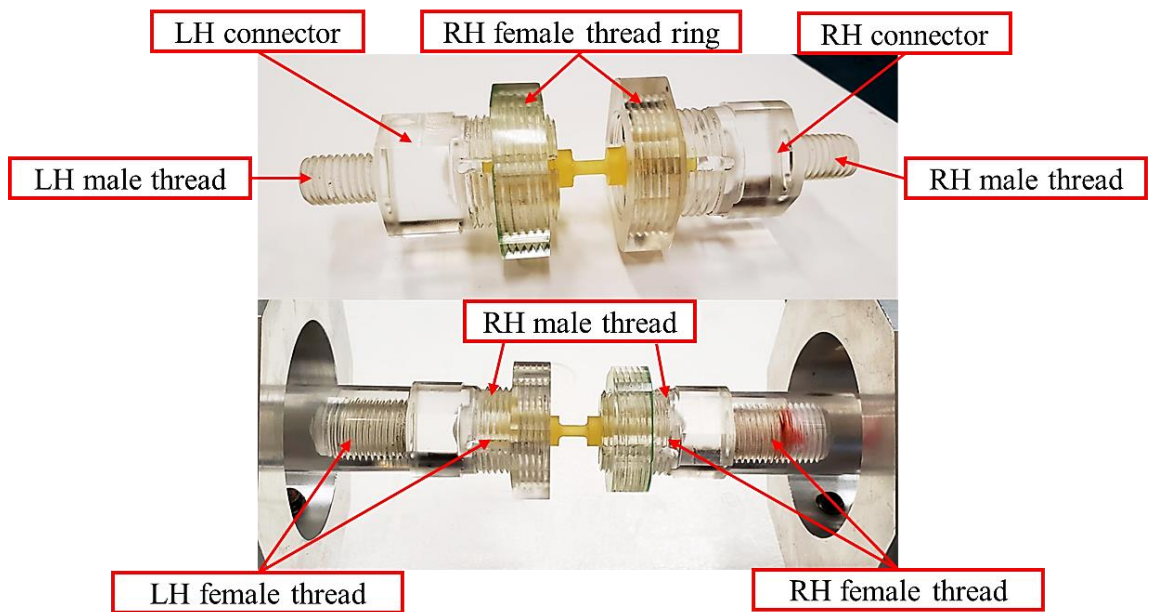


Figure 3.13. Custom clamping fixture for the SHTB specimens.

3.3.6 Compressive Polymeric Split-Hopkinson Pressure Bar (C-PSHPB) Test Specimen

In this study, a cylindrical specimen geometry was selected due to the minimum geometric impedance difference with the cylindrical bars and for consistency with the quasi-static and intermediate strain rate compression tests. The gauge dimensions of the specimen were determined iteratively, and several factors were considered when designing the specimen:

1. Minimizing the radial and longitudinal inertia (the ratio of sample length/diameter typically less than 1)
2. Achieving specimen dynamic equilibrium during the test

3. Lathing two flat loading faces orthogonal to the side of the sample
4. Finishing two loading faces parallel to each other with 0.01 mm tolerance or better
5. Limiting the bar stress within the elastic stress limit of the bars

By considering all the factors, several iterative tests were conducted to finalize the specimen geometry (Figure 3.14). The specimens were machined from hand-cast samples using an engine lathe (Microweily ty-1630s) with a 4mm precision collet and a universal milling machine (First LC1-1/2VS). The machining tools and parameters are listed for reference (Table 3.10).

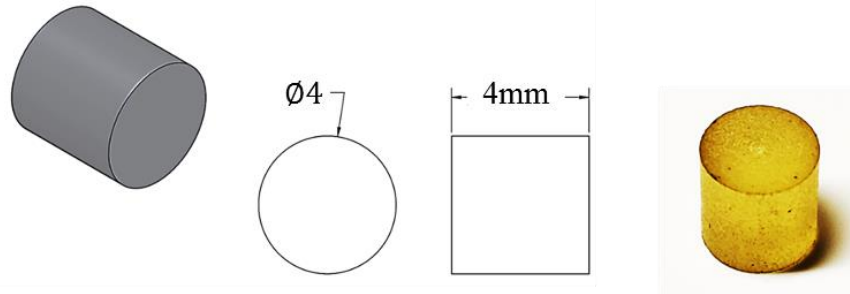


Figure 3.14. Specimen dimensions for the C-PSHPB tests.

Table 3.10. Summary of tools and machining parameters used for the C-PSHPB specimens.

| Tool | Spindle speed (RPM) | Feed rate | Cooling |
|------------------------------------|---------------------|-----------------------|---------|
| RH Turning/Facing with DCMT insert | 700 | Manual (slow) | Air |
| Ø1/"4 Center drill bit | 700 | Manual (intermediate) | Air |

3.3.7 Test Specimens for Validation of Material Constitutive Model

Validation tests were conducted to examine whether the material model adequately captured the response of the material under complex multiaxial stress states. In previous work, bending tests and shear tests on notched specimens were commonly used for validation purposes [92]. However, the dimensions of the fabricated samples of the epoxy material were not suitable for machining of bending and notched shear specimens. Thus, the validation specimens used in this study were based on the geometry of specimens designed by MatchID software with some modifications. MatchID is a software platform providing DIC-FEA validation solutions [115]. Two specimen geometries were designed to generate non-uniform stresses with local multiaxial stress states under the application of a uniaxial load. The first specimen comprised of a symmetric geometry, which was designed to validate the tensile and compressive responses of the material

model (Figure 3.15). The second specimen configuration was an asymmetric geometry designed to validate the shear response of the material model (Figure 3.16). The specimens were extracted from HP-RTM panels and machined in a universal milling machine (First LC1-1/2VS) with all the tools and parameters listed for reference (Table 3.11).

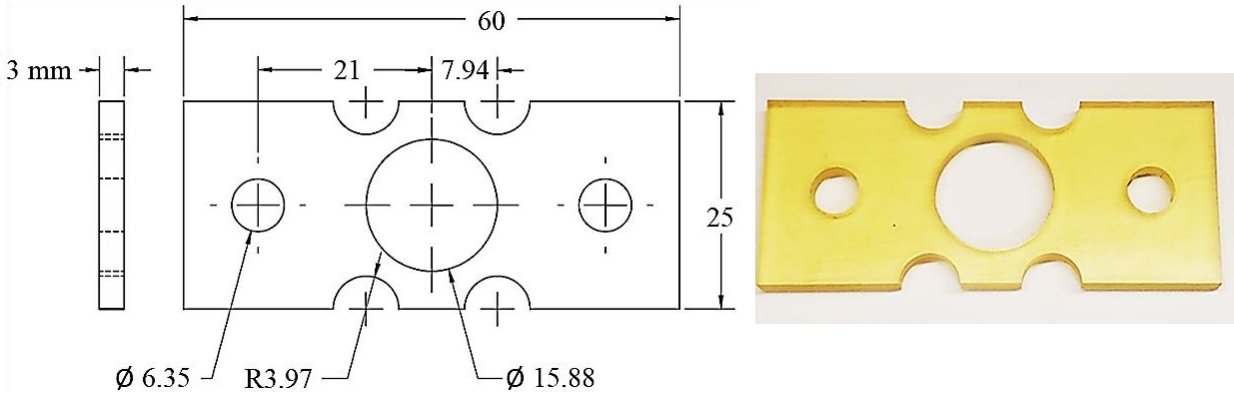


Figure 3.15. Geometrically symmetric specimen for validation of the material model for tensile and compressive stress states.

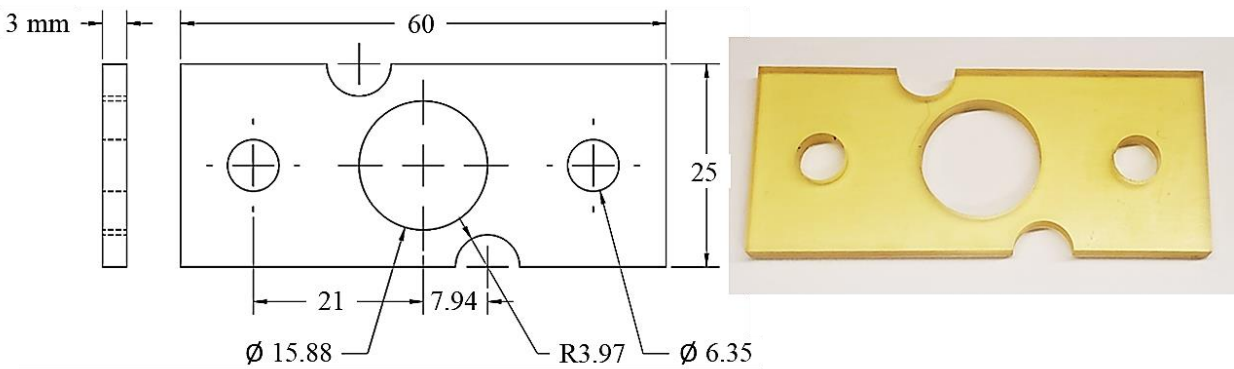


Figure 3.16. Geometrically asymmetric specimen for validation of the material model for shear stress states.

Table 3.11. Summary of tools and parameters used for machining the validation specimens.

| Tool | Spindle speed (RPM) | Feed rate (ipm) | Cooling |
|-----------------|---------------------|-----------------------|---------|
| Ø5/8" Drill bit | 90 | Manual (slow) | Coolant |
| Ø1/4" Drill bit | 500 | Manual (intermediate) | Air |
| Ø5/32" End mill | 1200 | Manual (slow) | Air |
| Ø16mm Reamer | 90 | Manual (slow) | Oil |

3.4 Mechanical Epoxy Characterization Test Equipment and Setup

Different techniques and apparatus were required to characterize the response of the studied epoxy material at different targeted strain rates applicable to automotive crashworthy applications. Uniaxial tests at different strain rates were conducted to investigate the compression, tensile, shear, and complex responses of the neat epoxy material, while DMA tests were conducted to identify the degree of cure and glass transition temperature of the processed samples (Table 3.12). Details for all tests performed are described in the following sub-sections.

Table 3.12. Summary of the material characterization tests performed in this study.

| Test | Property | Test frame | Frame displacement rate | Gauge section (mm) |
|--------------------------------------|------------------------------|--|--------------------------|---|
| Dynamic mechanical analysis | Glass Transition Temperature | DMA Q800 | N/A | 3.8 x 9.5 x 50.0 (Figure 3.7) |
| Quasi-static strain rate tension | Strain-Stress | Small Servo-hydraulic (MTS) | 0.0254 mm/s (0.001 in/s) | 3.8 x 3.0 x 12.5 (Figure 3.8) |
| | | | 0.254 mm/s (0.01 in/s) | |
| Intermediate strain rate tension | Strain-Stress | Hydraulic Intermediate Strain Rate (MTS) | 150 mm/s | 3.8 x 2.0 x 12.5 (Figure 3.8) |
| | | | 1,000 mm/s | |
| High strain rate tension | Strain-Stress | T-PSHPB | ~6,000 mm/s | Ø3.0 x 6.0 (Figure 3.12) |
| Quasi-static strain rate shear | Strain-Stress | Small Servo-hydraulic (MTS) | 0.0254 mm/s (0.001 in/s) | 3.8 x 3.1 (Figure 3.10) |
| | | | 0.254 mm/s (0.01 in/s) | |
| Intermediate strain rate shear | Strain-Stress | Hydraulic Intermediate Strain Rate (MTS) | 700 mm/s | 3.8 x 3.1 (Figure 3.10) |
| | | | 1,800 mm/s | |
| Quasi-static strain rate compression | Strain-Stress | Medium-scale Servo-hydraulic (MTS) | 0.01 mm/s | Ø12.7 x 12.7 (Figure 3.11) |
| | | | 0.1 mm/s | |
| Intermediate strain rate compression | Strain-Stress | Medium-scale Servo-hydraulic (MTS) | 15 mm/s | Ø12.7 x 12.7 (Figure 3.11) |
| High strain rate compression | Strain-Stress | C-PSHPB | ~2,200 mm/s | Ø4.0 x 4.0 (Figure 3.14) |
| Validation | Strain-field | Small Servo-hydraulic (MTS) | 0.0254 mm/s (0.001 in/s) | 3.8 x 25 x 25 (Figure 3.15) (Figure 3.16) |

3.4.1 Dynamic Mechanical Analysis (DMA)

DMA is a commonly used thermo-mechanical characterization technique, where a low-amplitude cyclic force or strain is applied to a test sample at controlled frequencies or temperatures to study its phase angle and deformation response [116]. DMA tests can be used to measure the glass transition temperature (T_g) of polymers and provide an indirect means to characterize the degree of cure [117]. Since two different processes were used to manufacture epoxy samples in this study, DMA tests were performed to compare the T_g of each specimen.

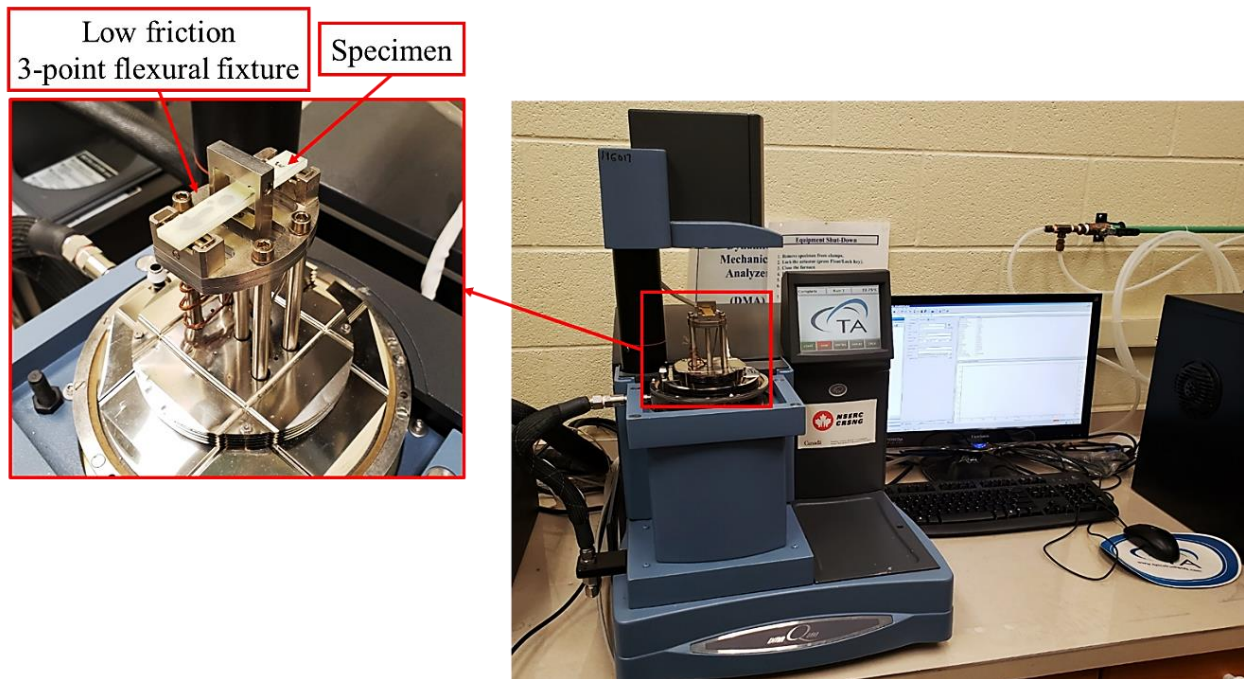


Figure 3.17. TA Instruments DMA Q800 and the specimen setup.

A TA Instruments DMA Q800 was used to conduct the DMA tests, while TA Universal Analysis software was used to collect and analyze the experimental data. As recommended by the user manual, the DMA test method for this research was a three-point flexural method (Figure 3.17). Strain sweep and temperature sweep tests were conducted to investigate the change of storage modulus and loss modulus of the samples over a range of temperatures. The storage modulus indicates the elastic portion of the sample or the amount of energy stored in the sample, while the loss modulus shows the viscous portion of the sample or the amount of energy dissipated as heat from the sample [116]. Generally, two glass transition temperatures (onset and peak) can be determined using the DMA test results. The onset T_g is the temperature that the storage modulus of the material starts to decrease significantly, and this value can be

determined by the storage modulus versus temperature plot. The peak T_g is the temperature that the tan delta curve (ratio of storage modulus to loss modulus) reaches its peak value, and this parameter can be determined by the tan delta versus temperature plot. Both T_g values can be used for analyzing the curing degree of the samples. After the machine calibration, the strain sweep test (see Appendix A) was performed to determine the applied strain for the temperature sweep tests. With the ideal applied strain, the temperature sweep tests (see Appendix A) were conducted to study the change of storage modulus and loss modulus of the material over the targeted temperature range. The storage modulus and loss modulus versus temperature plots were generated and investigated by the TA Universal Analysis software after the temperature sweep tests.

3.4.2 Quasi-Static and Intermediate Strain Rate Uniaxial Tensile Tests

All the tensile tests were carried out in a lab environment with a constant temperature ($24 \pm 1^\circ\text{C}$) and relative humidity ($50 \pm 5\%$). Quasi-static strain rate tensile tests were conducted on an MTS servo-hydraulic test frame with custom pin-loaded fixtures at a constant displacement rate. An MTS FlexTest SE controller was used, and the applied force was measured by a load cell (OMEGA LC412-500) with 500-lbf capacity (Figure 3.18). Intermediate strain-rate tension tests were conducted on a hydraulic intermediate strain rate (HISR) apparatus with custom pin-loaded fixtures (Figure 3.19). The test frame functioned by accelerating an engagement sleeve to a predetermined constant velocity, which then contacted the engagement piston at the bottom of the stroke. An MTS 407 unit was used to control the loading process of the frame, while the applied force was measured by a piezoelectric force sensor (KISTLER 9341B) with ± 30 kN range.

Four different strain rate settings were used to characterize the tensile properties of the material at the quasi-static and intermediate strain rate range (Table 3.13). For quasi-static strain rate tests, two uniaxial tensile tests were performed at a constant crosshead displacement rate (CCDR) of 0.001 and 0.01 in/s. For intermediate strain rate tensile tests, the crosshead displacement rates were set to 150 and 1000 mm/s. A minimum of five specimens were tested for each tensile test setup, and additional trial tests were conducted to ensure that the setup was appropriate.

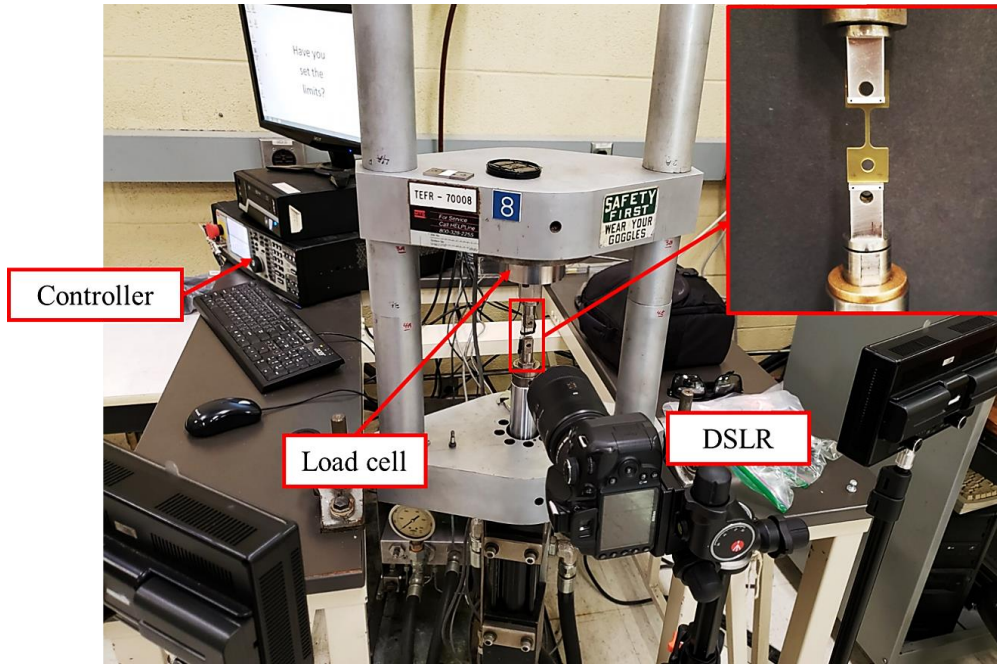


Figure 3.18. MTS servo-hydraulic test frame used for quasi-static tension tests.

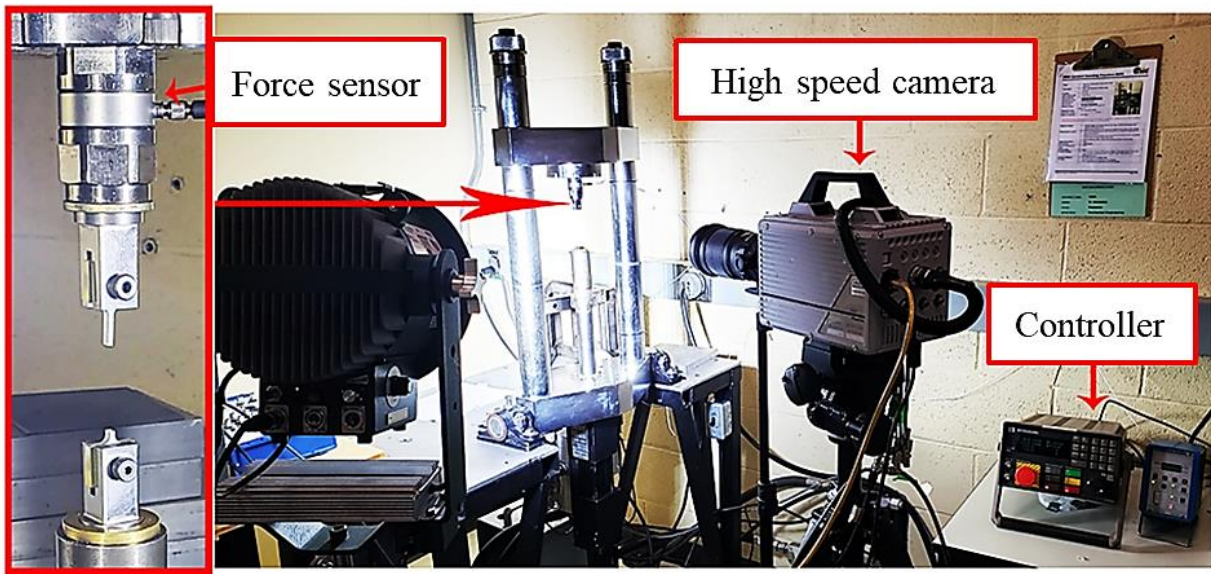


Figure 3.19. HISR test apparatus for intermediate strain rate tests.

Table 3.13. Summary of camera settings for the tension tests conducted at quasi-static and intermediate strain rates.

| Crosshead displacement rate | | Camera | Image size (pixels) | Frame rate (FPS) |
|-----------------------------|------------|-------------|---------------------|------------------|
| Quasi-static | 0.001 in/s | Nikon D3200 | 1920 x 1080 | 30 |
| | 0.01 in/s | Nikon D3200 | 1920 x 1080 | 30 |
| Intermediate | 150 mm/s | Photron SA5 | 1024 x 1024 | 7,000 |
| | 1,000 mm/s | Photron SA5 | 192 x 592 | 50,000 |

The deformation or the strain of the specimens was captured using a 2D digital image correlation (DIC) method. The gauge section of all specimens was painted with stochastic speckle pattern using latex-based spray paint. A Nikon D3200 Digital Single-lens Reflex (DSLR) camera was used to record the loading motions during the quasi-static strain rate tests, while a Photron SA5 high-speed camera was used for the intermediate strain rate tests. For post-processing of captured images, an industry-grade DIC software, GOM Correlate, was used to calculate the strain of the specimen without using any strain filters. The parameters of the cameras were selected based on the test duration, the specimen gauge area, and the lighting condition. There are some general rules that were followed to set up the camera for DIC purposes. First, the camera frame rate setting was able to record the whole test and provide sufficient frames or images. Second, the recorded images captured the full gauge area of the specimen and provided sufficient detail. Third, for two-dimensional DIC, the optical axis of the camera lens was perpendicular to the recorded specimen surface and located in the center of the gauge section area. A summary of the camera settings for the tension tests at the quasi-static and intermediate strain rates is listed (Table 3.13). For the GOM setup, the subset sizes were 15 pixels for D3200 images and 32 pixels for SA5 images, while the step size was determined according to the frame rate, which was one frame per step.

For the calculation of the material properties, the elastic modulus was measured as the slope of the stress-strain curves between 0.1% and 1% strain, where the initial unstable data resulting from grip sliding or specimen/grip misalignment was avoided. The Poisson's ratio was calculated as the ratio of negative transverse strain rate to the axial strain rate in the elastic range, where all the strain rates were measured by a DIC method. For polymers, yield strength can normally be determined as maximum stress (yield point) before the strain-softening stage, but the yield point might not be identified for some glassy polymers because of their low elongation to break during the tension tests. It has been noticed that there were different

methods to define the tensile yield strength of polymer, from 0.3% to 2% strain offset. In this study, a 0.3% offset of the elastic modulus slope line was reported since it was commonly accepted in the polymer technical community [118]. In addition, the fracture surface of the specimens was investigated with a KEYENCE digital microscope equipped with a high-resolution zoom lens, VH-Z500R.

3.4.3 Quasi-Static and Intermediate Strain Rate Uniaxial Shear Tests

For quasi-static and intermediate strain rates, uniaxial shear tests were conducted using the same test frames, fixtures, and cameras as those used for the uniaxial tension tests, while the same DIC technique was also used to analyze the sample deformation. The shear behaviour of the material was characterized at four different strain rates (Table 3.14). For the quasi-static strain rates, two uniaxial shear tests were performed at 0.001 and 0.01 in/s CCDR. For the intermediate strain rates, the crosshead displacement rates were set to 700 and 1800 mm/s. A minimum of five specimens was tested for each test setup. Following the same rules mentioned in Section 3.3.2, the camera setting for the shear tests is listed (Table 3.14). To determine the shear properties of the tested material, the shear elastic modulus was measured as the slope of the stress-strain curve between 0.1% and 1% strain, where the initial unstable data resulting from grip sliding or specimen/grip misalignment was avoided. The shear yield strength was determined as maximum stress before the strain softening of the material.

Table 3.14. Summary of camera settings for shear tests conducted at quasi-static and intermediate strain rates.

| Crosshead displacement rate | | Camera | Image size (pixels) | Frame rate (FPS) |
|-----------------------------|------------|-------------|---------------------|------------------|
| Quasi-static | 0.001 in/s | Nikon D3200 | 1920 x 1080 | 30 |
| | 0.01 in/s | Nikon D3200 | 1920 x 1080 | 30 |
| Intermediate | 700 mm/s | Photron SA5 | 576 x 576 | 20,000 |
| | 1,800 mm/s | Photron SA5 | 448 x 384 | 40,000 |

3.4.4 Quasi-Static and Intermediate Strain Rate Uniaxial Compression Tests

The quasi-static and intermediate compression tests were conducted on a medium-scale custom-built servo-hydraulic test frame with flat platen fixtures. An MTS 407 hydraulic controller was used, while the applied force was measured by a 20k load cell (Transducer Techniques SWP) with 20,000 lb capacity (Figure 3.20). To reduce the specimen barreling during the compression tests, in addition to the use of white lithium grease for lubrication, two carbide plates were placed between the platens and the specimen to reduce the surface contact friction (Figure 3.21).

The same cameras and DIC software used for the tension tests were also used for the quasi-static and intermediate strain-rate compression tests. One difference for the DIC technique used during the compression tests was that point tracking was used instead of speckle patterns to analyze the deformation of the cylindrical specimen surfaces using a 2D DIC setup. The camera setting for the compression tests followed the same method as tensile and shear tests (Table 3.15). Three strain rates were used to characterize the compression properties of the epoxy material. Two sets of quasi-static strain rate compression tests were performed at 0.01 and 0.1 mm/s CCDR, while one set of tests was conducted at the intermediate strain rate of 15 mm/s CCDR.

For each test condition, a minimum of five specimens was tested. For the result processing, the compressive elastic modulus was measured as the slope of the stress-strain curves between 0.1% and 1% strain, where the initial unstable data resulting from lubrication was avoided. The yield strength was determined as maximum stress before the strain softening of the material.

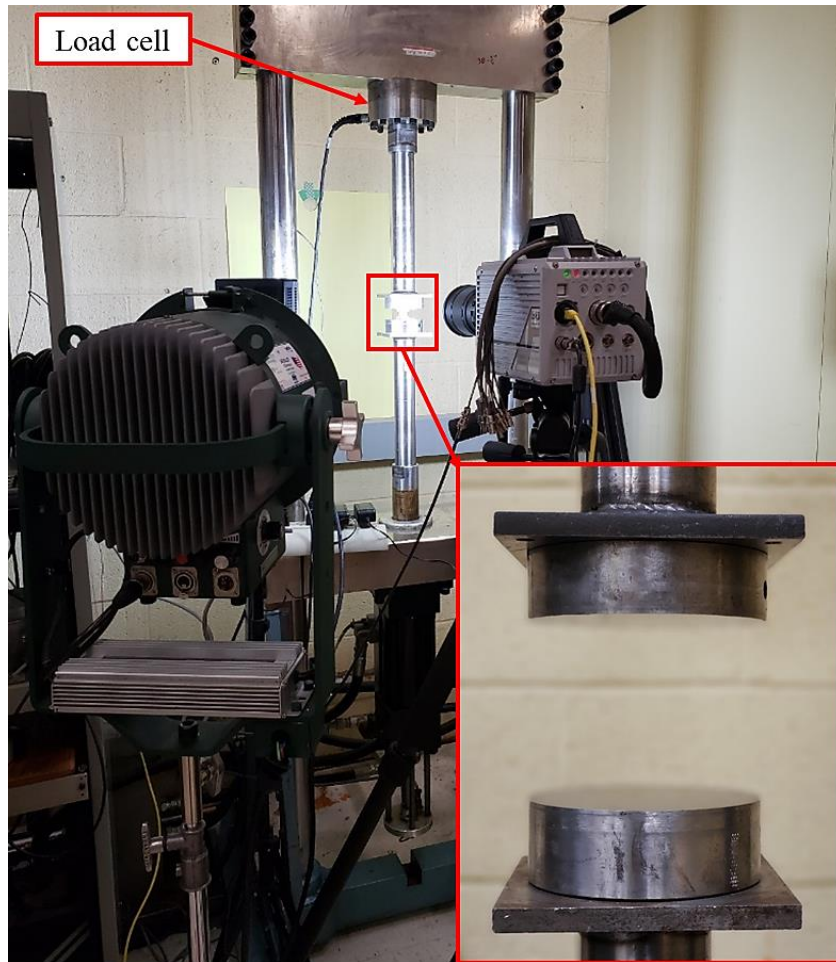


Figure 3.20. Custom-built 20,000 lb servo-hydraulic test frame used for the quasi-static and intermediate strain rate compression tests.

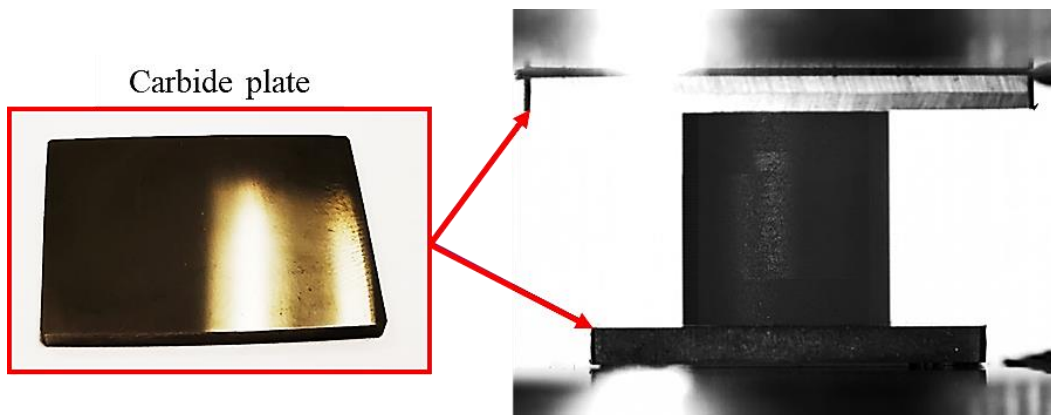


Figure 3.21. Carbide plates mounted between platens and epoxy specimen.

Table 3.15. Summary of the camera settings for compression tests performed at quasi-static and intermediate strain rates.

| Crosshead displacement rate | | Camera | Image size (pixels) | Frame rate (FPS) |
|-----------------------------|-----------|-------------|---------------------|------------------|
| Quasi-static | 0.01 mm/s | Nikon D3200 | 1920 x 1080 | 30 |
| | 0.1 mm/s | Nikon D3200 | 1920 x 1080 | 30 |
| Intermediate | 15 mm/s | Photron SA5 | 1024 x 640 | 5,000 |

3.4.5 Tensile Polymeric Split-Hopkinson Pressure Bar (T-PSHPB) Apparatus: High Deformation Rate Tension Testing

As reviewed in Section 2.2.2, the split-Hopkinson pressure bar technique was commonly used for the dynamic characterization of glassy polymers. In this study, a custom-built T-PSHPB system was used to characterize the studied epoxy material (Figure 3.22). In this system, a hollow cylindrical striker bar loaded by four bungee cords impacted the flange of the incident bar to generate an elastic stress-wave in the specimen. The T-PSHPB apparatus was designed for polymer characterization, and thus comprised of plastic bars to minimize the material impedance difference with the tested epoxy specimens (Table 3.16 Figure 3.23). The impact velocity of the striker bar was adjusted by changing the stretch length of the bungee cords, while a load cell (OMEGA LC412-1k) with 1,000-lbf capacity measured the applied load. In this study, a 32 N load was applied to the striker bar to accelerate the bar to a velocity of 6 m/s upon impact. The strain of the incident and transmitter bars was measured by two strain gauges (OMEGA SGD-7/1000-LY13) and two signal-conditioning amplifiers (Vishay 2210B). The test signals were recorded by National Instruments™ LabVIEW software. A Photron SAZ high-speed camera was also used to capture the specimen deformation during the tests for subsequent DIC analysis and to verify the calculated strain from the T-PSHPB system.

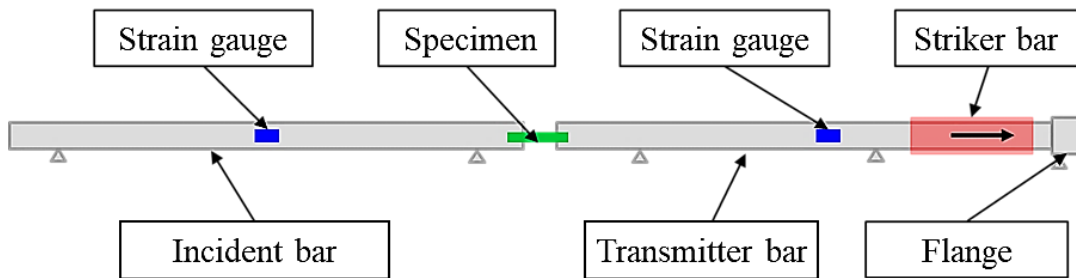


Figure 3.22. Schematic of T-PSHPB apparatus.

Table 3.16. The specifications for the T-PSHPB components.

| Bar | Material | Dimension (mm) |
|-------------|--------------------------------|-------------------|
| Striker | Polycarbonate | OD38 x ID29 x 311 |
| Incident | Polymethyl methacrylate (PMMA) | Ø26 x 2527 |
| Transmitter | PMMA | Ø26 x 2503 |

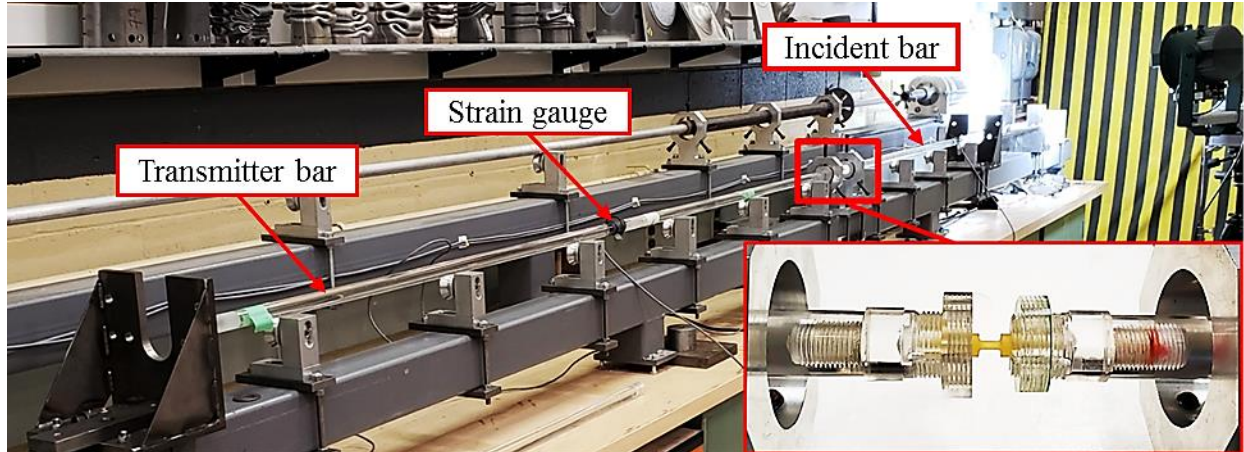


Figure 3.23. Image of the T-PSHPB apparatus.

A custom software, CHSB Version 3.2 (Salisbury, 2001, University of Waterloo) was used to post-process the test data, including the material stress-strain response analysis, specimen dynamic force state verification, and strain rate calculation. The CHSB software required calibration files for both the incident bar and the transmitter bar to perform calculations, including bar dimensions, strain gauge locations, the strain-voltage coefficient, the mechanical properties of bars, and the wave propagation coefficient. For each set of tests, depending on the completion of the calibration files, static and dynamic bar-calibrations were required. The static bar-calibration determines the strain-voltage coefficients, while the dynamic bar-calibration provides the wave propagation coefficient (see Appendix B). The T-PSHPB tests were all conducted using the final calibrated parameters (Table 3.17). Due to the challenges of the test requirements and specimen machining, a minimum of three specimens were tested for the T-PSHPB test.

Table 3.17. Parameters for the performed T-PSHPB tests.

| Bungee cords loading | Sticker bar impact velocity | Amplifier gain | Data sampling frequency | High speed camera rate |
|----------------------|-----------------------------|----------------|-------------------------|------------------------|
| 32 N | ~ 6 m/s (DIC) | 610 | 1,000,000 Hz | 480,000 fps |

3.4.6 Compressive Polymeric Split-Hopkinson Pressure Bar (C-PSHPB) Apparatus: High Deformation Rate Compressive Testing

Similar to a T-PSHPB, a typical C-PSHPB test apparatus consists of a transmitter bar, an incident bar, a striker bar, two strain gauges and one data acquisition system, where strain gauges are located at the center of the transmitter and incident bar surfaces (Figure 2.13). Differences between the T-PSHPB and the C-PSHPB are the striker bar impact location, loading device, and specimen clamping method. Overall, the two systems have similar principles and requirements. The custom-built C-PSHPB apparatus used in this study also comprised of polymeric bars (Table 3.18).

Table 3.18. The specifications of the C-PSHPB components.

| Bar | Material | Dimension (mm) |
|-------------|--------------------------------|----------------|
| Striker | Polymethyl methacrylate (PMMA) | Ø26 x 710 |
| Incident | PMMA | Ø26 x 2438 |
| Transmitter | PMMA | Ø26 x 2438 |

In this C-PSHPB system, the striker bar was loaded by digitally controlled compressed nitrogen gas, and the impact velocity of the striker bar was adjusted by changing the compressed gas pressure (Figure 3.24). In this study, the compressed gas pressure applied to the striker bar was set to 20 psi to yield a striker bar impact velocity of 2.2 m/s. The strains of the incident and transmitter bars were measured by two strain gauges (Micro-Measurements CEA-13-250UW-120) and two signal-conditioning amplifiers (Vishay 2210B). The test signals were recorded by a National Instruments™ LabVIEW software. A Photron SAZ high-speed camera was also used to record specimen deformation during the tests and to perform subsequent DIC analysis. The CHSB software Version 3.2 was used to post-process the SHPB test data. Similar to the T-PSHPB test, the CHSB software requires calibration files for both the incident bar and the transmitter bar to perform the calculation for the C-PSHPB test, thus static and dynamic calibration may be required for both the incident and transmitter bar. The individual static and dynamic calibration processes for incident and transmitter bars are similar between C-PSHPB and T-PSHPB. One additional calibration test for the C-PSHPB is an end-to-end dynamic calibration, which verifies the condition of the contact surfaces and alignment of the two bars, as well as the wave propagation coefficient (see Appendix B). All conducted C-PSHPB tests were used the calibrated parameters (Table 3.19). A minimum of three repeated tests were performed for the C-PSHPB tests.

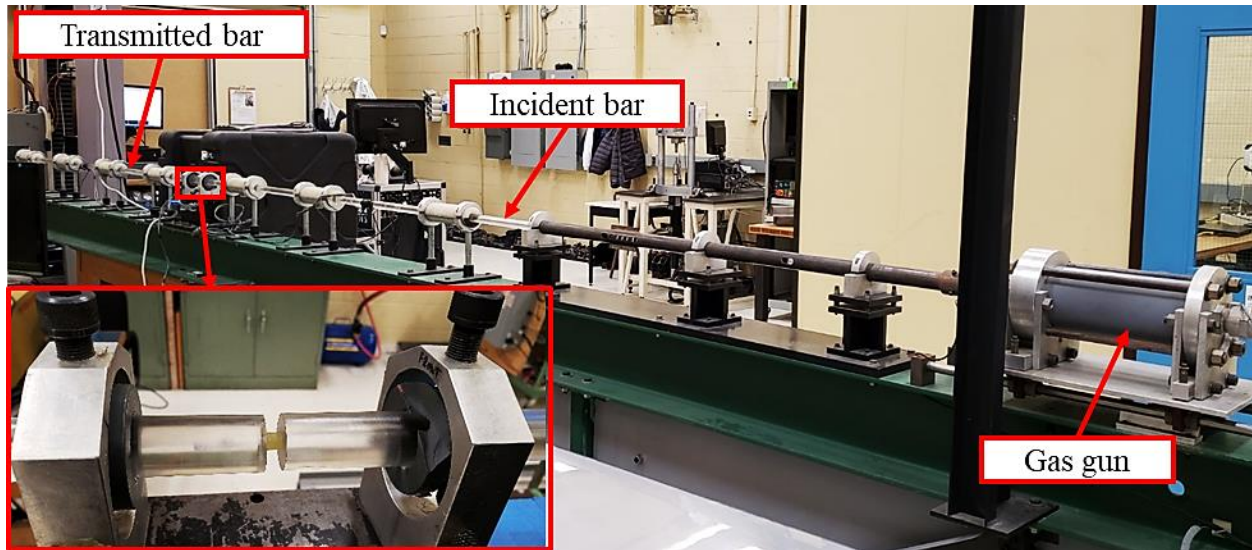


Figure 3.24. Image of the C-PSHPB apparatus.

Table 3.19. Parameters for the performed C-PSHPB tests.

| Compressed gas pressure | Sticker bar impact velocity | Amplifier gain | Data sampling frequency | High speed camera rate |
|-------------------------|-----------------------------|----------------|-------------------------|------------------------|
| 20 psi | ~ 2.2 m/s (DIC) | 300 | 1,000,000 Hz | 300,000 fps |

3.4.7 Validation Tests for Computational Model

The validation tests were conducted at a quasi-static strain rate with the same setup as the tensile tests discussed in Section 3.4.2, using the specimen geometers presented in Section 3.3.7. The crosshead displacement rate was set to 0.001 in/s, and the camera settings used for the quasi-static tensile tests were also adopted (Table 3.20). DIC was used to capture the strain fields of the specimen just before failure, and these results were compared with the FEA simulation results.

Table 3.20. Summary of the camera settings for validation tests performed at a quasi-static strain rate.

| Crosshead displacement rate | | Camera | Image size (pixels) | Frame rate (FPS) |
|-----------------------------|------------|-------------|---------------------|------------------|
| Quasi-static | 0.001 in/s | Nikon D3200 | 1920 x 1080 | 30 |

Chapter 4 Epoxy Characterization Test Results

The DMA test results of both hand-cast and HP-RTM specimens are first presented, and the T_g of each, which is representative of the degree of cure, are compared. Next, the test results for tensile, shear, and compression at different strain rates are presented and discussed. The fracture surfaces of the tested specimens are also investigated to determine the effect of strain rate on fracture surface morphology. All the characterization tests aimed to establish the strain rate dependent behaviour of the studied epoxy.

4.1 DMA Test Results

In this study, the performed DMA testing consisted of two tests: strain sweep and temperature sweep (see Section 3.4.1). The strain sweep test was conducted to determine a suitable applied strain for the subsequent temperature sweep tests. Since the geometries of both the HP-RTM and hand-cast specimens were the same and a similar mechanical response was anticipated, only the HP-RTM specimens were considered for strain sweep tests. The main result of the strain sweep test is a storage modulus versus applied strain profile (Figure 4.1). Accordingly, the values of storage modulus stabilized at approximately 3200 MPa within the strain range of 0.01 to 0.065%, which confirms that the elastic behaviour of the specimen is stable in this strain range. For this study, a strain magnitude of 0.035% was selected for the subsequent temperature sweep tests.

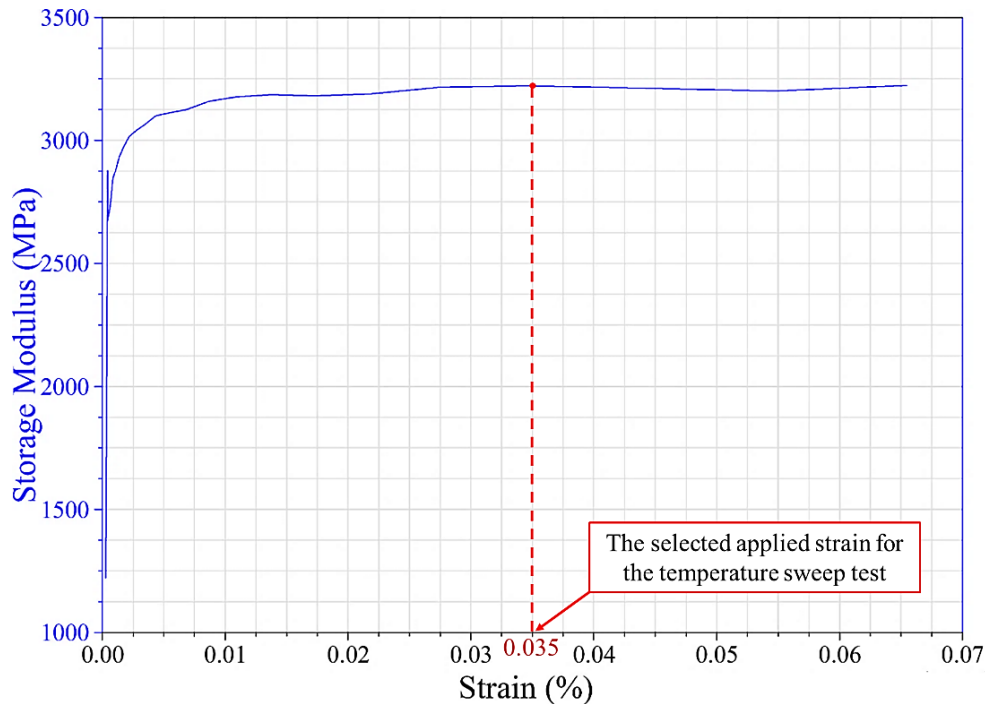


Figure 4.1. The strain sweep test result for the DMA test (HP-RTM specimen).

The temperature sweep tests were conducted to analyse the change of the storage modulus, loss modulus and tan delta (i.e., the ratio of loss-to-storage modulus) for both types of specimens over the expected glass transition temperature range (i.e., ~120 °C). To determine the T_g , the storage modulus-temperature and loss modulus-temperature data for specimens extracted from the HP-RTM panels and hand cast cylinders were investigated (Figure 4.2 and Figure 4.3). The scatter of the temperature sweep test results for three HP-RTM specimens was minimal (Figure 4.2), which revealed a consistency in the elastic and viscous properties at different locations across the fabricated HP-RTM panels. For the three hand-cast specimens, the scatter of the temperature sweep test results was more significant than the HP-RTM specimens (Figure 4.3). The deviation of the material properties might be caused by variations of the component mixture ratio of the resin system and curing temperatures during the hand-cast process.

As mentioned in Section 3.4.1, the T_g of the test specimens could be determined based on the storage modulus, loss modulus, and tan delta. Following the description in Section 3.4.1, the onset T_g (from storage modulus curves) and peak T_g (from tan delta curves) values for these two types of specimens are labelled (Figure 4.2 and Figure 4.3). Using the temperature sweep test results, a comparison of the T_g for both types of specimens with a 95 % confidence interval (CI) is shown (Table 4.1). Statistical hypothesis tests (Student's T-distribution) were conducted, and the results indicated that there was a statistically significant difference (alpha = 0.050) between the two sets of T_g . The average onset and peak T_g values for the HP-RTM specimens are 3% higher compared to the hand-cast specimens, which indicates that the HP-RTM specimens have a slightly higher degree of cure or crosslink density. This result agrees with a generally accepted theory, where a higher cure temperature yields a higher T_g for the same epoxy system (i.e., Chapter 2). Moreover, the T_g values for both specimens were similar in magnitude to those provided by the supplier (Table 3.2). Since the difference in the T_g between the two types of tested specimens was considered negligible, their mechanical properties were deemed to be similar.

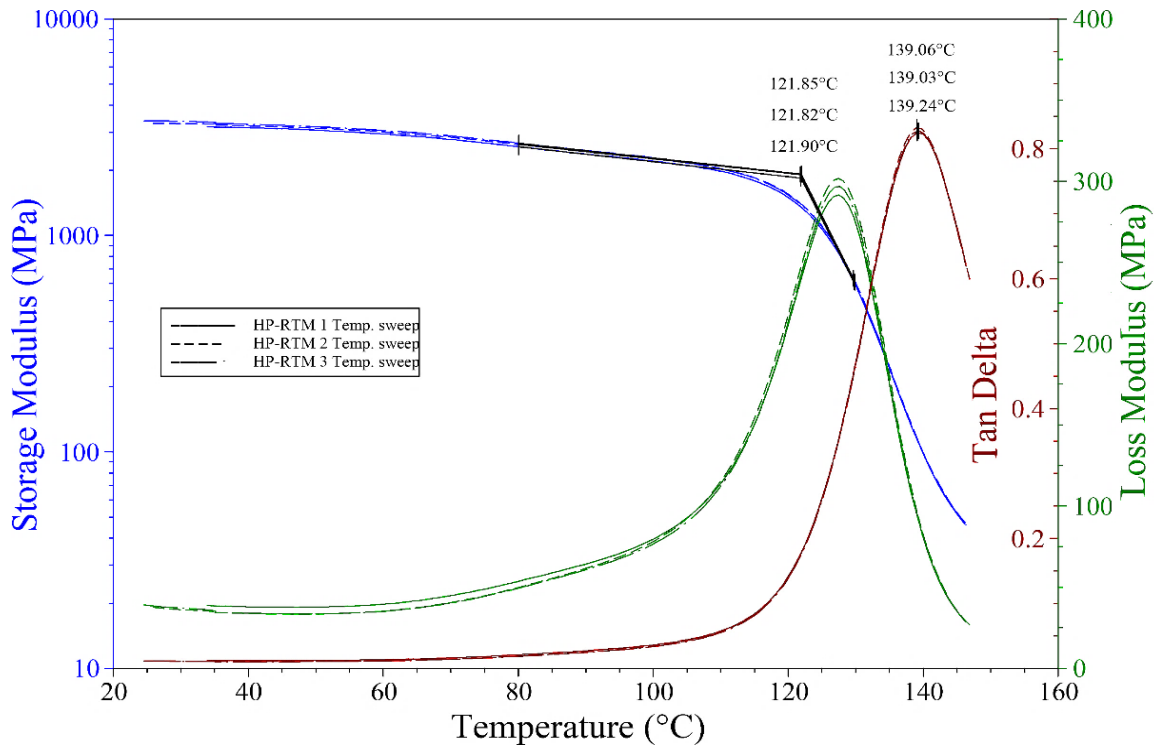


Figure 4.2. The results of temperature sweep DMA tests for the HP-RTM specimens.

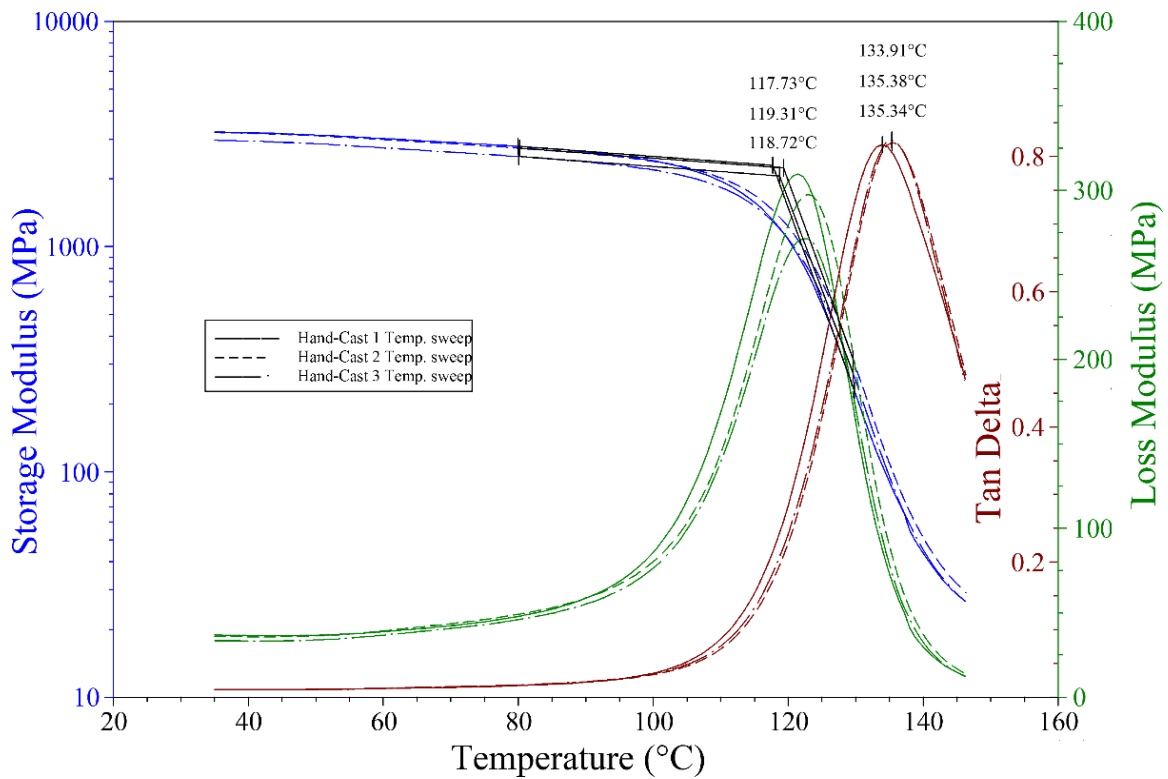


Figure 4.3. The results of the temperature sweep DMA tests for the hand-cast specimens.

Table 4.1. T_g for HP-RTM and hand-cast specimens (95% CI and T-test) obtained using DMA.

| | HP-RTM | Hand-Cast | % Diff. | P_{two trials} |
|------------------------------------|-------------------|-------------------|----------------|-------------------------------|
| Onset T_g ($^{\circ}\text{C}$) | 121.86 \pm 0.05 | 118.59 \pm 0.91 | 3% | 0.020 |
| Peak T_g ($^{\circ}\text{C}$) | 139.11 \pm 0.12 | 134.88 \pm 0.95 | 3% | 0.013 |

4.2 Uniaxial Tensile Test Results

4.2.1 Quasi-static Strain Rate Tensile Test Results

Uniaxial tensile tests were conducted at two different strain rates in the quasi-static range ($3.3 \times 10^{-4} \text{ s}^{-1}$ and $3.5 \times 10^{-3} \text{ s}^{-1}$) using the same specimen geometry and test equipment (see Section 3.4.2). Experimental strain measurements showed that the major and minor strain distributions were uniform in the gauge section of the specimens during deformation. The stress-strain response of the epoxy was consistent for each repeated test, for each strain rate (Figure 4.4). This reveals that the mechanical properties of the HP-RTM resin panels were consistent, owing to the uniformity of the fabricated panel. As mentioned in Section 3.2.1, the quasi-static tensile tests conducted using specimens extracted from these flat panels were compared with the corresponding test results provided by the manufacturer (Table 3.2). A good agreement between these results was observed, revealing that the panel flattening procedure did not affect the mechanical properties of the epoxy material.

Overall, the tensile response of the epoxy material demonstrated moderate ductile deformation behaviour. For both quasi-static strain rates considered, the epoxy deformed elastically up to approximately 1-2% strain. Thereafter, the epoxy plastically deformed reaching the yield point at approximately 7% strain. This observation agrees with the common stress-strain behaviours of the glassy polymers discussed in Chapter 2. The failure strain of the specimens varied from 7 to 10% strain, which was attributed to machining-induced defects that occurred during specimen fabrication.

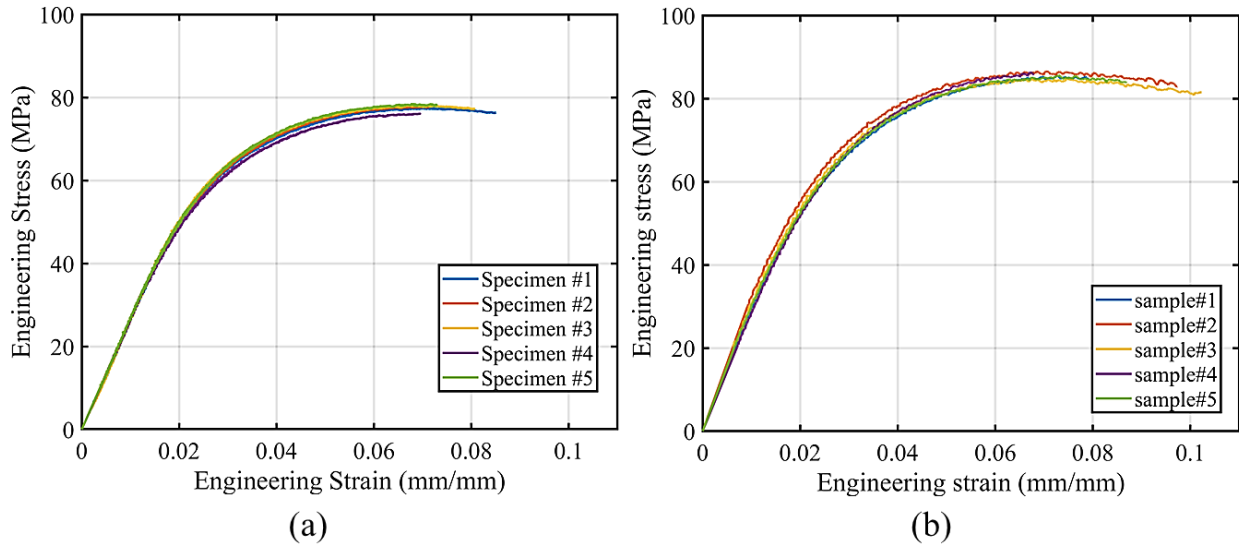


Figure 4.4. Uniaxial tensile engineering stress-strain curves for quasi-static strain rates of: (a) 0.00033 s^{-1} , and (b) 0.0035 s^{-1} , Note, five repeated tests were performed for each strain rate.

4.2.2 Intermediate Strain Rate Tensile Test Results

In the intermediate strain rate range, uniaxial tensile tests were conducted at two different strain rates (3.2 s^{-1} and 23.9 s^{-1}) using the mini dog-bone specimen geometry and the HISR apparatus (see Section 3.4.2). For both loading cases considered, the stress-strain response of the epoxy was consistent for all repeated tests (Figure 4.5).

Overall, the response of the epoxy at intermediate strain rates demonstrated lower ductility when compared to the response measured during the quasi-static strain rate tests. For both intermediate strain rates, the response of the epoxy in the linear elastic region was similar (around 1-2 % strain) to the quasi-static strain rate tensile tests. All the specimens fractured at the plastic flow region, without reaching the strain-softening stage. Thus, no yield point was identified in the intermediate strain rate tensile tests. There was notable variation in the failure strain of the specimens (from 4% to 9% strain), and the tests conducted with a strain rate of 3.2 s^{-1} have notably low failure strains compared to the other quasi-static and intermediate tensile tests. The low failure strains may have been a result of the applied loading frequency, which was close to the natural frequency of the hydraulic loading device; this resonance issue was previously reported as a common challenge for a hydraulic intermediate strain rate apparatus [63].

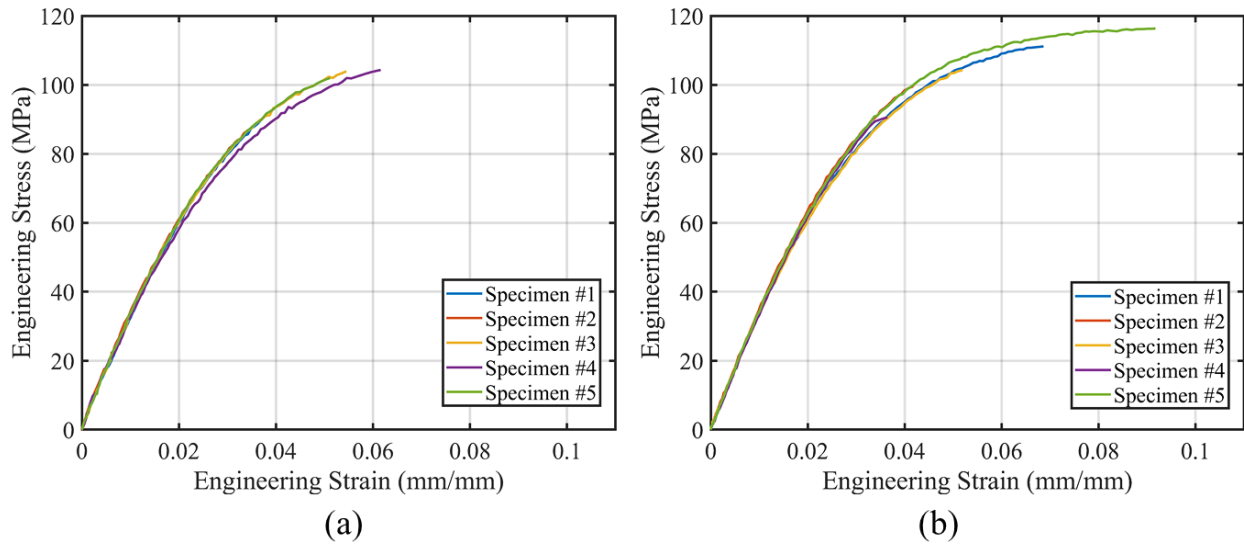


Figure 4.5. Uniaxial tensile engineering stress-strain curves for intermediate strain rates of: (a) 3.2 s^{-1} , and (b) 23.9 s^{-1} . Note, five repeated tests were performed for each strain rate.

4.2.3 High Strain Rate Tensile Test Results

In the high strain rate range, the tensile tests were conducted at only one strain rate (approximately 300 s^{-1}) using the specimen geometry and test protocol discussed in Section 3.4.5. Based on the split Hopkinson-bars test guidelines (see Section 2.2.2), dynamic force equilibrium must be achieved during the test to obtain valid results. To assess dynamic force equilibrium for the T-PSHPB tests, two approaches were used, namely one-wave versus two-wave verification and a direct method employing DIC. The one-wave versus two-wave method compares the forces on both ends of the test specimen measured from the incident and transmitter bars using the CHSB software. To ensure that a specimen attains dynamic force equilibrium, these forces should be equal for the duration of the test. The corresponding results for one of the T-PSHPB tests revealed that the specimen reached dynamic force equilibrium (Figure 4.6). In contrast, the direct approach involved measuring strain directly on the test specimen surface at various locations along its length. Dynamic force equilibrium was achieved if the strain versus time curves overlap, indicating that the specimen undergoes uniform deformation along the gauge section. In this study, the test specimens were divided into three sections (Figure 4.7 a), and specimen deformation was captured using a high-speed camera with a frame rate of 480,000 fps. DIC software was used to analyze the captured images and calculate the strain versus time for each section. The corresponding strain-time data indicated that the same specimen reached dynamic force equilibrium during the test (Figure 4.7 b).

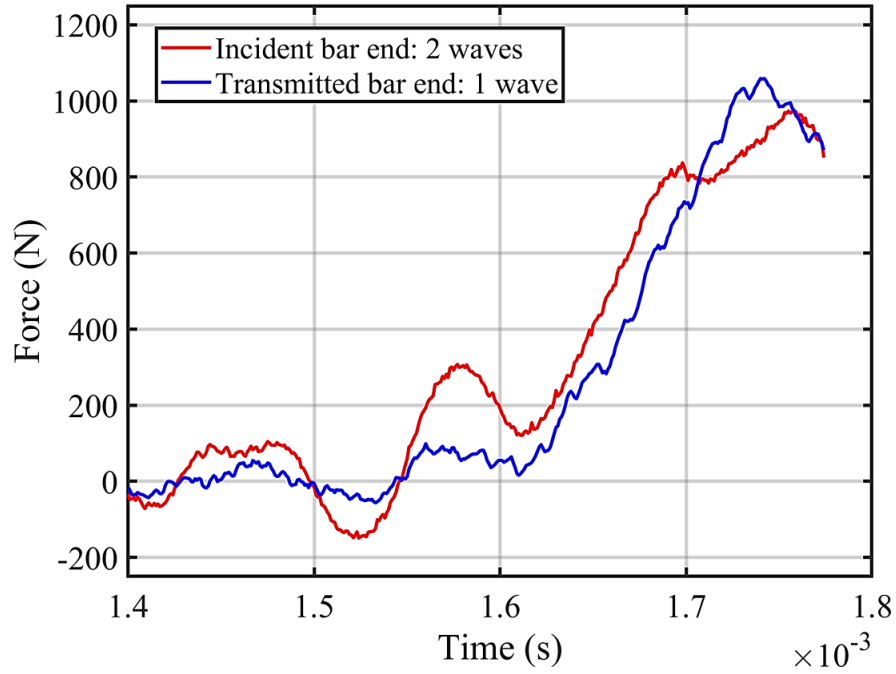


Figure 4.6. The force-time profiles measured from the incident end (two-wave) and transmitter bars (one-wave) for the T-SHPB test.

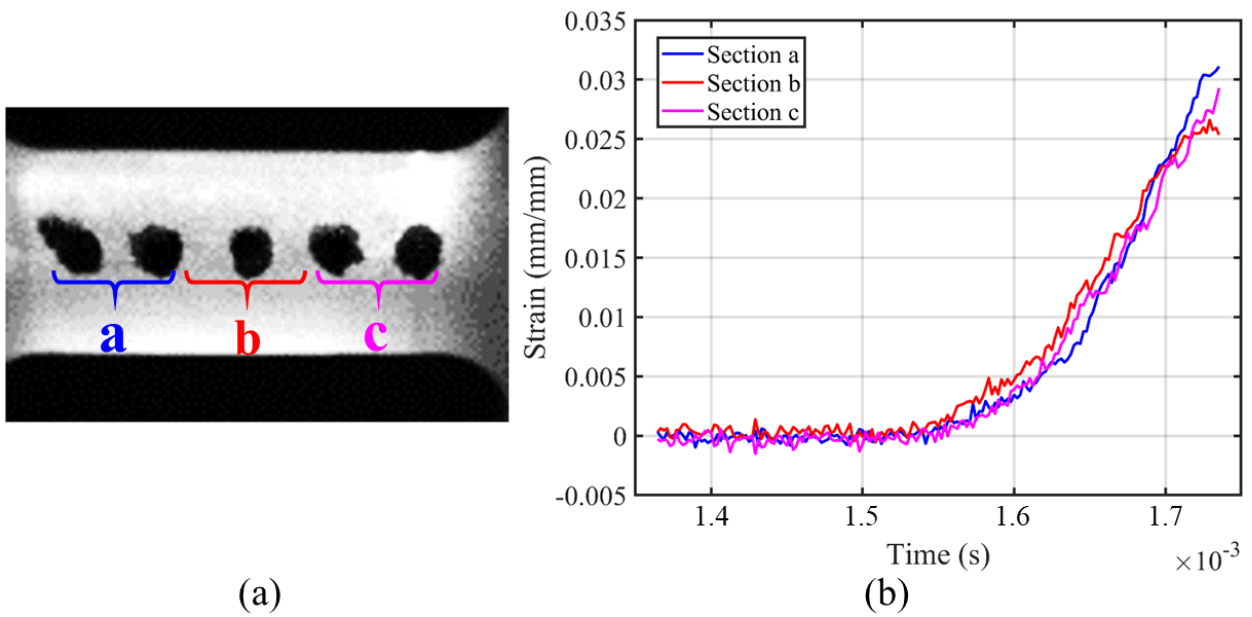


Figure 4.7. (a) A gauge section image of the T-SHPB test specimen indicating three sections analyzed using DIC, and (b) strain-time plots for three indicated sections.

Furthermore, a good agreement was found between the strain calculated by the CHSB software and that extracted from DIC (Figure 4.8), thus verifying the accuracy of the CHSB software. This is important for this tensile split Hopkinson-bar test because the fillets located at both ends of the gauge section of the dog-bone specimens might affect the strain calculation from the CHSB software. These results also demonstrate that after an initial transition the test specimens were subjected to a constant strain rate for the duration of the tests.

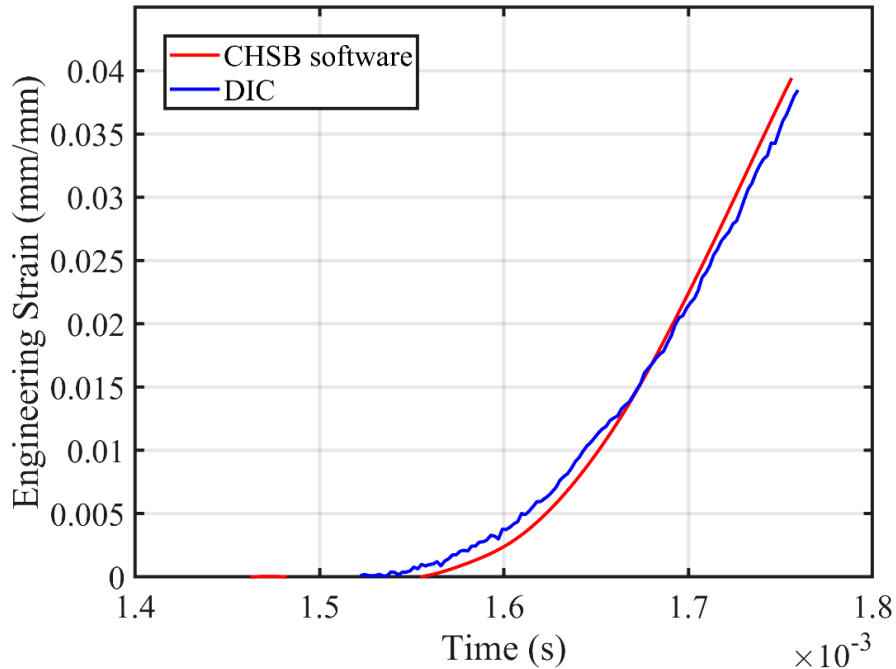


Figure 4.8. Strain profiles calculated by the CHSB software and captured by the DIC method for the T-SHPB test.

The engineering stress-strain plots for the T-PSHPB specimens reveal that the epoxy deformed in a linear elastic manner prior to failure, with an average strain at failure of $\sim 3.7\%$ (Figure 4.9). The stress-strain response and failure strains for the repeated tests were found to have good consistency. It should be noted that for the T-PSHPB tests, only three repeated test results are reported since these were the only tests conducted where dynamic force equilibrium of the specimen was attained. Not every specimen tested was able to reach dynamic force equilibrium due to the short test duration and low strain to failure of the test specimens.

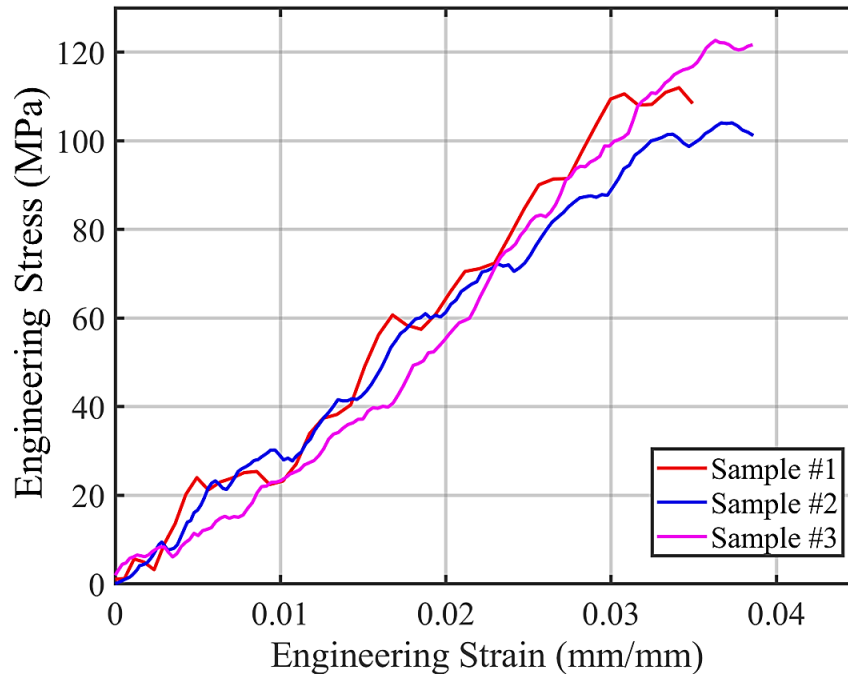


Figure 4.9. Uniaxial tensile engineering stress-strain curves for a strain rate of 300 s^{-1} by CHSB software). Note, three repeated tests were performed at this strain rate.

4.2.4 Summary of the Tensile Test Results

The average tensile stress-strain curves for all considered strain rates were combined to assess the strain rate-dependent response of the epoxy (Figure 4.10). The elastic modulus, tensile strength, 0.3% offset tensile strength and Poisson's ratio were carefully determined based on the engineering stress and strain results, and a 95% confidence interval for each value was calculated (Table 4.2). The elastic modulus and 0.3% offset strength of the epoxy both increased with higher strain rates (Figure 4.11 and 4.12), while the Poisson's ratio remained constant at 0.38 ± 0.04 . The elastic modulus increased by 34% for high strain rate loading when compared to the quasi-static strain rate case, while the yield strength increased by 31% over the same range of strain rate. As indicated in Figure 4.11 and 4.12, the strain rate dependence of the tensile modulus and 0.3% offset strength roughly follows a linear logarithmic increment relation. These phenomenological-based relationships were adopted by many constitutive models to capture the strain rate dependence of epoxy [51, 109].

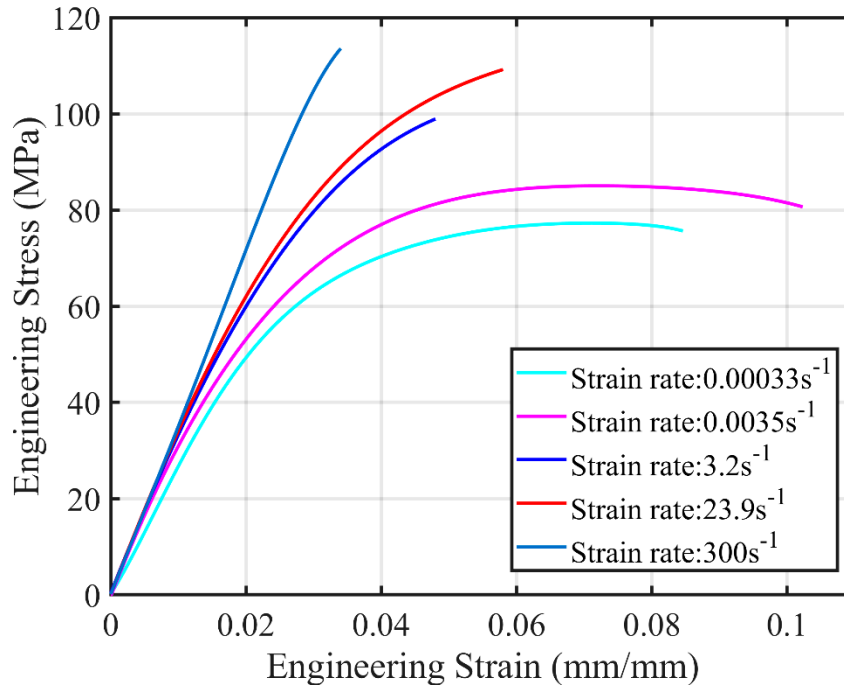


Figure 4.10. Average stress-strain response of the epoxy material at the different tensile loading strain rates.

Table 4.2. Summary of mechanical properties for tensile tests at different strain rates (95% CI)

| Average strain rate | 0.00033 s ⁻¹ | 0.0035 s ⁻¹ | 3.2 s ⁻¹ | 23.9 s ⁻¹ | 300 s ⁻¹ |
|----------------------------|-------------------------|------------------------|---------------------|----------------------|---------------------|
| Elastic modulus (GPa) | 2.70 ± 0.09 | 3.02 ± 0.23 | 3.12 ± 0.12 | 3.25 ± 0.08 | 3.57 ± 0.70 |
| Tensile strength (MPa) | 77.6 ± 1.8 | 85.8 ± 1.3 | 97.5 ± 16.1 | 104.6 ± 19.4 | 115.8 ± 20.0 |
| 0.3% offset strength (MPa) | 47.2 ± 3.0 | 53.9 ± 4.1 | 70.9 ± 5.3 | 73.4 ± 4.5 | N/A |
| Poisson's ratio | 0.39 ± 0.02 | 0.36 ± 0.04 | 0.38 ± 0.04 | 0.39 ± 0.02 | N/A |

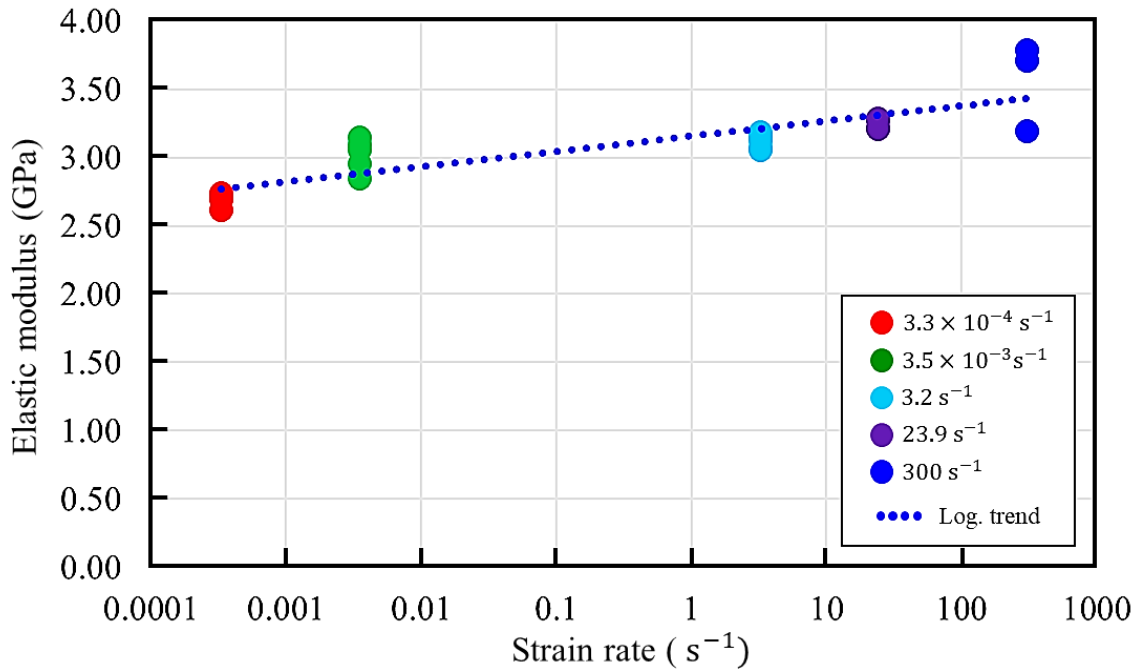


Figure 4.11. The increase of tensile elastic modulus associated with increased strain rate.

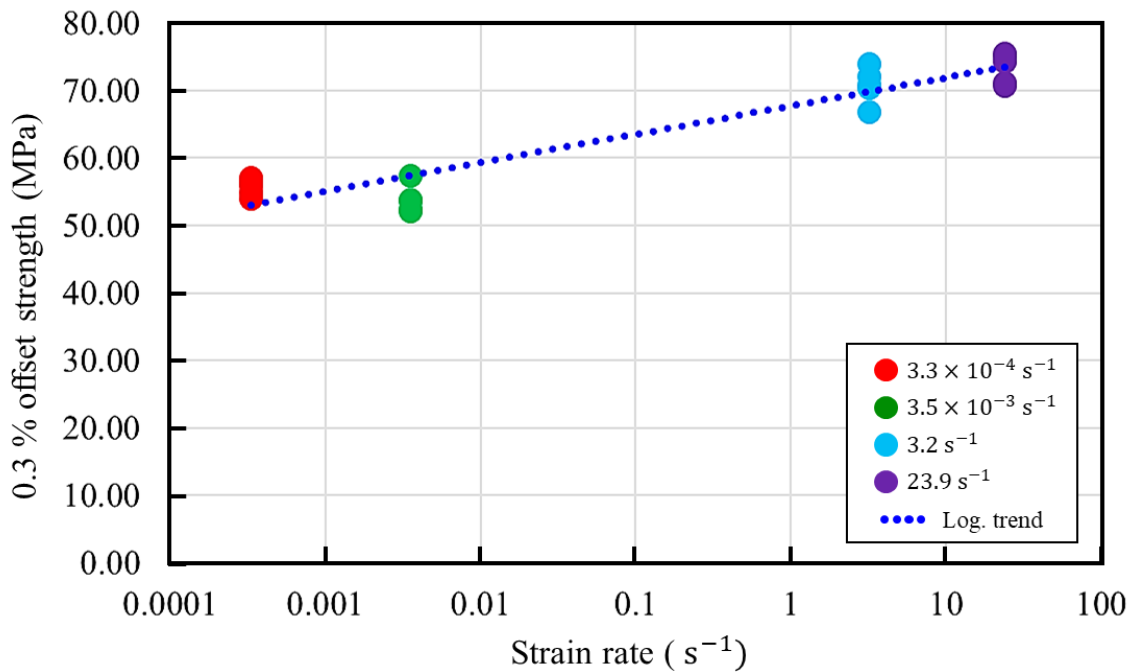


Figure 4.12. The increase of 0.3% offset strength associated with increased strain rate.

4.3 Uniaxial Compression Test Results

4.3.1 Quasi-static Strain Rate Compression Test Results

Uniaxial compression tests were conducted at two different quasi-static strain rates ($8 \times 10^{-4} \text{ s}^{-1}$ and $8 \times 10^{-3} \text{ s}^{-1}$), and the same specimen geometry and test equipment were used (see Section 3.4.4).

For both loading conditions, the stress-strain response for all repeated tests was consistent prior to the yield point, with notable scatter in the strain re-hardening stage (beyond 25% strain) (Figure 4.13). In this stage, strain re-hardening was primarily affected by the crosslink network, including crosslink density, crosslink distributions, specimen defects, which may have varied from specimen to specimen. The specimen fractured along the axial direction due to the tensile transverse strains induced by Poisson's effect. The difference in failure strain was less than 6% between specimens for both strain rates.

Overall, the stress-strain response of the epoxy material demonstrated typical ductile behaviour, in which elastic, plastic flow, strain softening, and strain re-hardening stages were observed (Figure 4.13). For both quasi-static strain rates considered, the epoxy deformed elastically up to approximately 1-2% strain. Thereafter, the inelastic deformation of the epoxy specimens was significant, reaching the yield point at approximately 7% strain. Beyond the yield point, the epoxy specimens deformed plastically in the strain range of 8 – 15%, leading to strain softening because of shear band relocation. In the final stage of the deformation process from approximately 15% until specimen failure at 45-55% strain, the stress continuously increased during strain re-hardening.

To ensure quality of the processed data, specimen buckling and barreling were inspected using images captured during the tests. The side view of a cylindrical compression specimen during the quasi-static compression test was inspected, where no visible buckling was observed (Figure 4.14). Specimen barreling was observed to be minor between 0 and -25% strain, while there is some notable barreling in the final strain stage before specimen failure (Figure 4.14) which may have also contributed to the scatter observed in Figure 4.13.

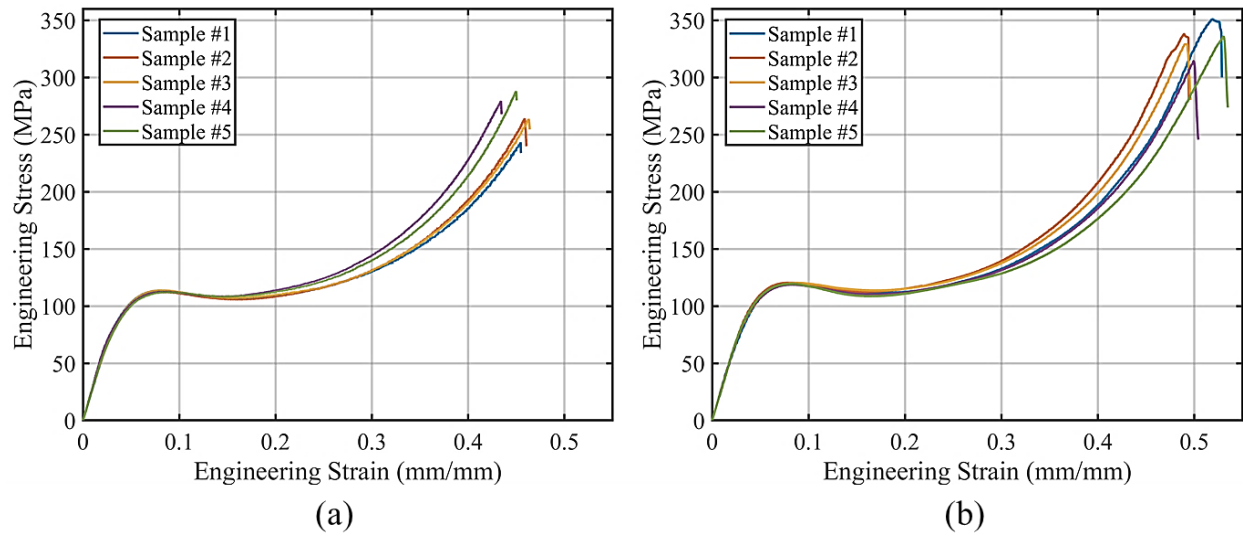


Figure 4.13. Uniaxial compressive engineering stress-strain curves for quasi-static strain rates of: (a) 0.0008 s^{-1} , and (b) 0.008 s^{-1} . Note, five repeated tests were performed for each strain rate.

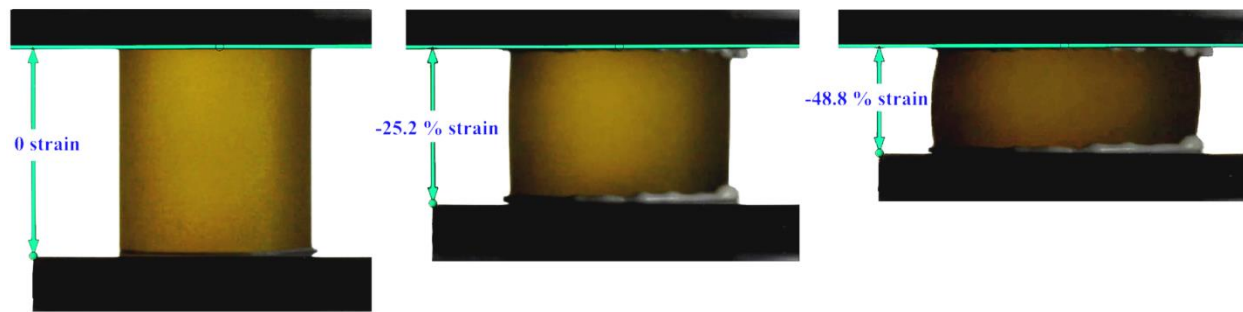


Figure 4.14. Barreling of a cylindrical specimen at the different strains during a quasi-static compression test (0.008 s^{-1}).

4.3.2 Intermediate Strain Rate Compression Test Results

In the intermediate strain rate range, the uniaxial compression tests were performed at one strain rate (1.56 s^{-1}) due to limitations with the test frame. The specimen geometry and test equipment were provided in Section 3.4.4. From the corresponding DIC analysis, it was observed that the test frame cross-head speed reduced when some of the tested specimens attained compressive strains beyond 35% (Figure 4.15). Thus, the corresponding test results are presented up to a strain of 35%. Similar to the quasi-static strain rate tests, assessment of the engineering stress-strain response revealed that the specimens underwent similar deformation stages including elastic, plastic flow, strain softening, and strain re-hardening (Figure 4.16). During the deformation, the yield point was observed at approximately 10% strain, while the strain re-hardening began at 18% strain. The stress-strain response for all repeated tests was consistent prior to the

yield point, whereas the post-yield behaviour beyond 10% strain shows minor scatter. The specimens ultimately fractured along their axial direction due to the tensile transverse strains induced by Poisson's effect.

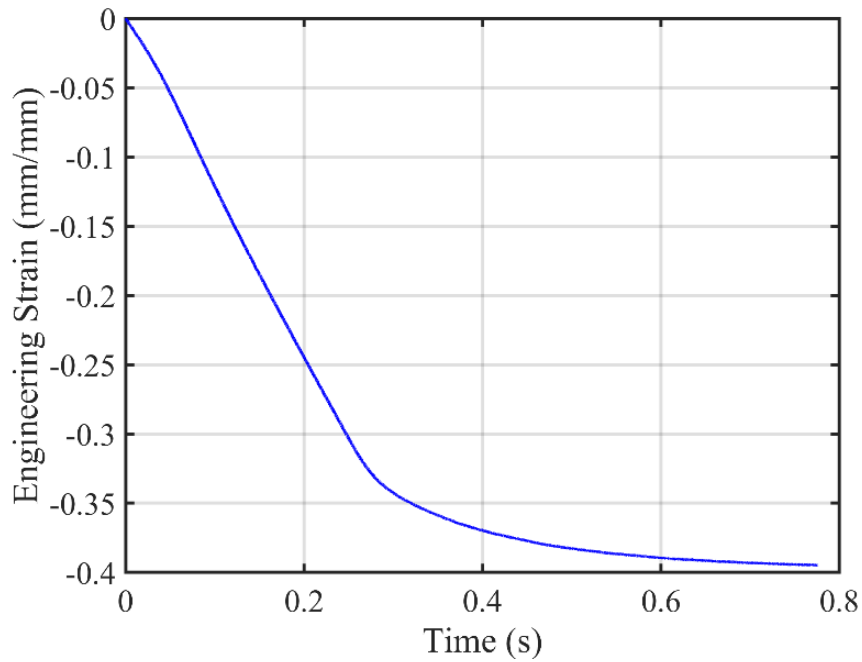


Figure 4.15. Strain versus time for an intermediate strain rate compression tests (1.56 s^{-1}).

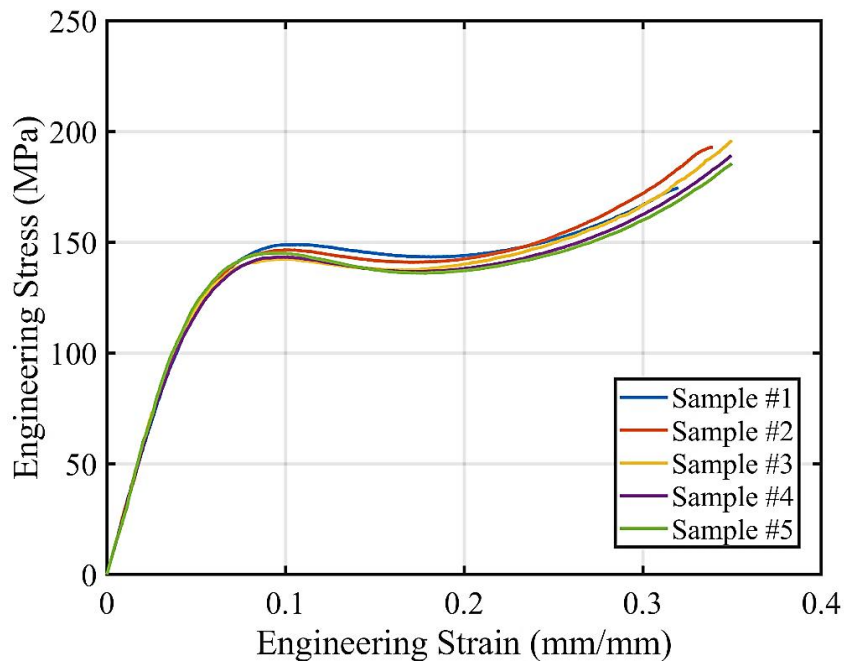


Figure 4.16. Uniaxial compressive engineering stress-strain curves at the intermediate strain rate (1.56 s^{-1}). Note, five repeated tests were performed for this strain rate.

To ensure quality of the processed data, specimen buckling and barreling were inspected using images captured during the tests. The side view of a cylindrical compression specimen during an intermediate strain-rate compression test was checked, where no visible buckling was observed (Figure 4.17). Specimen barreling is not observed between 0 and -19 % strain, while there is minor barreling in the strain re-hardening stage at approximately -35% strain (Figure 4.17), which may have contributed to the scatter observed in Figure 4.16.

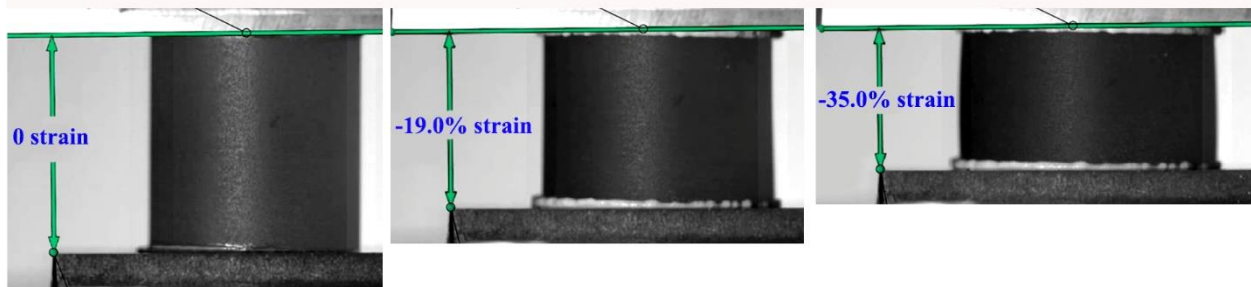


Figure 4.17. The barreling of a cylindrical specimen at the different strains during one intermediate strain rate compression test (1.56 s^{-1}).

4.3.3 High Strain Rate Compression Test Results

In the high strain rate regime, uniaxial compression tests were performed under only one strain rate (approximately 550 s^{-1}) using the C-PSHPB. The specimen geometry and test setup were described in Section 3.4.6. Unlike the low failure strain that was observed for the performed high strain rate tensile tests, the C-PSHPB test specimens exhibited a high failure strain so that dynamic force equilibrium was more readily achievable. To verify this, the one-wave versus two-wave method was used through the CHSB software for one of the C-PSHPB tests (Figure 4.18). The specimen clearly reached a dynamic force equilibrium during the test. As discussed in Section 4.2.3, for the T-PSHPB tests a DIC method was also used to verify the dynamic force equilibrium. However, this method was not suitable for the C-PSHPB test due to the short specimens used. To verify the calculation results of the software, the strain calculated by the CHSB software was compared with the strain captured by the DIC method (Figure 4.19), and a reasonably good agreement was found between the two results.

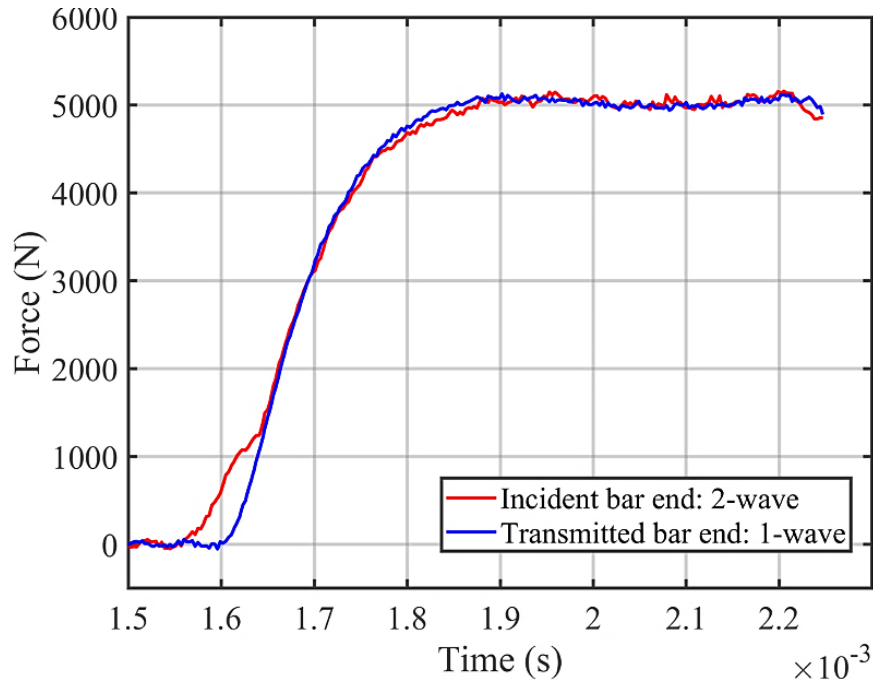


Figure 4.18. The force-time profiles from the incident end (two-wave) and transmitter bars (one-wave) for a C-PSHPB tests.

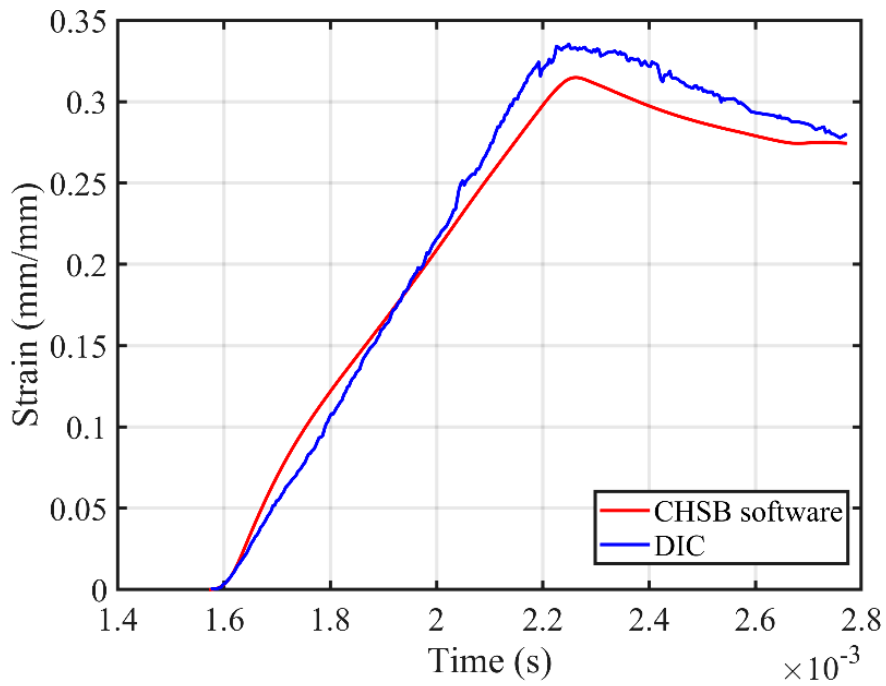


Figure 4.19. A comparison of strain calculated by the CHSB software and captured by the DIC method for a C-PSHPB test.

The engineering stress-strain response of the epoxy revealed that the yield point was attained at 13% strain (Figure 4.20). In contrast to the quasi-static and intermediate strain rate tests, strain softening and re-hardening were not significant. Three repeated tests were performed with minor scatter in the stress-strain response. The specimens fractured explosively into small pieces at failure.

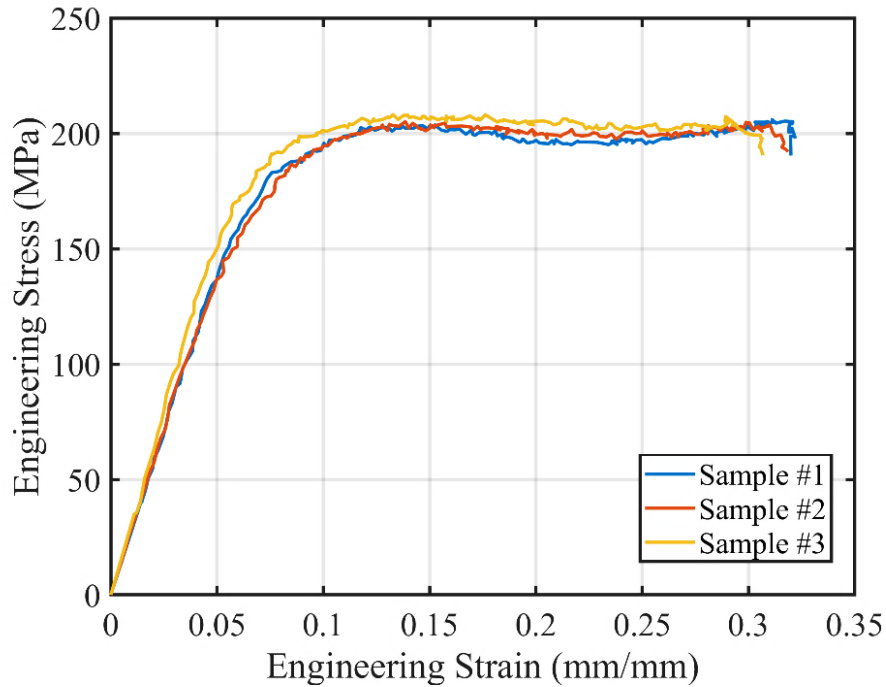


Figure 4.20. Uniaxial compressive engineering stress-strain curves for the high strain rate of 550 s^{-1} . Note, three repeated tests were performed for this strain rate.

4.3.4 Summary of the Compression Test Results

The average compressive stress-strain curves for all considered strain rates are combined to assess the strain rate-dependent response of the epoxy (Figure 4.21). The overall stress-strain response is similar at different strain rates. The elastic modulus and the yield strength were carefully determined based on the engineering stress and strain results, and a 95% confidence interval for each value was calculated (Table 4.3). The elastic modulus was observed to have little change with increasing strain rate. Single-factor analysis of variance (ANOVA) showed that there were no statistically significant differences of the compressive elastic modulus between different strain rates ($F = 1.03$ and $F_{\text{crit}} = 4.10$). In contrast, increased yield strengths were associated with increased strain rates (Figure 4.22). From the lowest quasi-static strain rate to the highest strain rate, the yield strength increases as much as 81%.

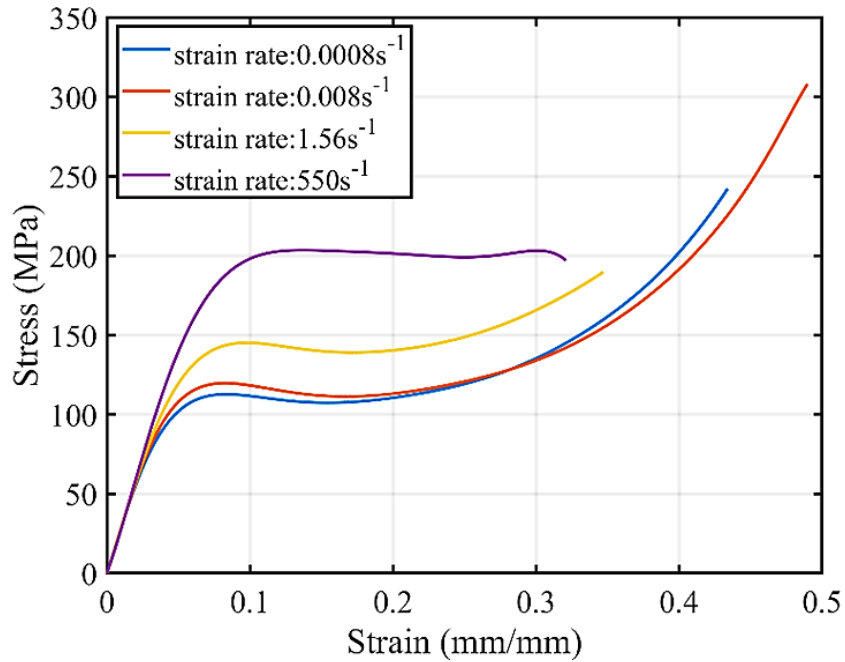


Figure 4.21. Average stress-strain response of the epoxy material at the different compression strain rates.

Table 4.3. Summary of mechanical properties for compression tests at different strain rates (95% CI).

| Average strain rate | 0.0008/s | 0.008/s | 1.56/s | 550/s |
|-----------------------|-----------------|-----------------|-----------------|-----------------|
| Elastic modulus (GPa) | 2.84 ± 0.06 | 2.85 ± 0.24 | 2.87 ± 0.02 | 2.89 ± 0.16 |
| Yield strength (MPa) | 113.1 ± 1.7 | 119.9 ± 1.4 | 146.1 ± 4.1 | 205.0 ± 3.1 |

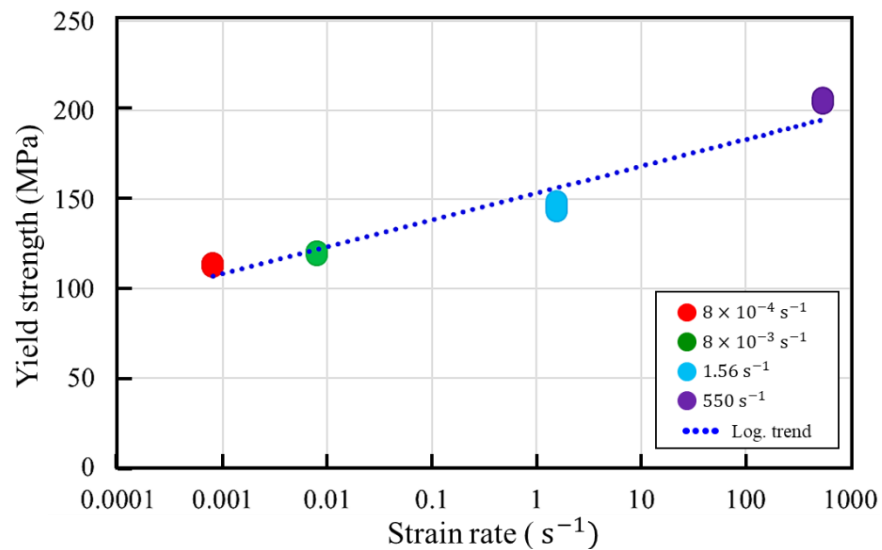


Figure 4.22. The increase of the yield strength associated with increased strain rates under compression.

4.4 Uniaxial Shear Test Results

4.4.1 Quasi-static Strain Rate Shear Test Results

In the quasi-static strain rate range, shear tests were performed at two different strain rates (1.3×10^{-3} and $1.2 \times 10^{-2} \text{ s}^{-1}$), and for all tests the same specimen geometry and test equipment were used (see Section 3.3.3 and 3.4.3). The engineering stress-strain response of the epoxy under uniaxial shear loading at the two quasi-static strain rates was investigated (Figure 4.23). For both quasi-static strain rates considered, the overall shear deformation of the epoxy was similar to that reported in previous studies conducted using torsional specimens (Littell et al., 2008; Gilat et al., 2007), where distinct deformation segments were observed (i.e., elastic, plastic flow and strain softening). The yield point of the shear deformation was observed at 17-20 % strain during the plastic flow segment. Thereafter, the specimens fractured at strains of 23-33% in the strain-softening stage.

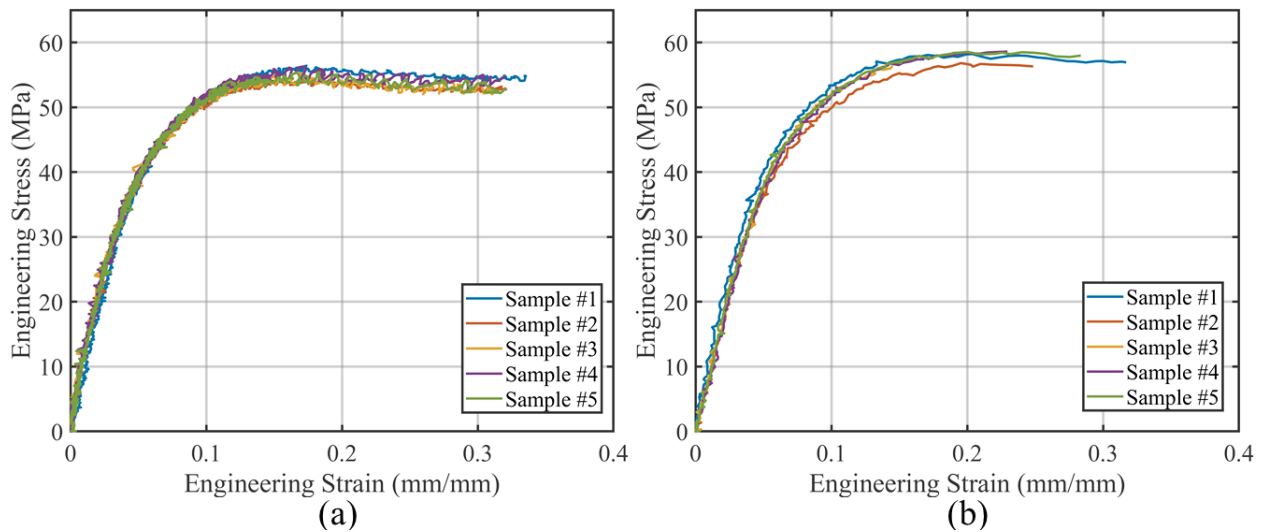


Figure 4.23. Engineering shear stress-strain curves for quasi-static strain rates of: (a) 0.0013 s^{-1} , and (b) 0.012 s^{-1} . Note, five repeated tests were performed for each strain rate.

It should be noted that fracture of the specimen initiated at the inner arc away from the center of the specimen (Figure 4.24) due to tension, causing the crack to open (Mode I) along the y-axis direction. For both loading conditions, the stress-strain response for all repeated tests was consistent with minor scatter. However, notable fluctuations were observed with the stress-strain data and were induced by the strain calculations of the DIC software. Unlike the tensile and compression test in which the strains were calculated as the change of gauge distance (mean value) in the DIC software, the shear strains were

measured from the shear deformation at the center point of the specimen (Figure 4.24). Thus, the shear strain calculations were very sensitive to small rotation of the gauge section. Also, strain contours captured using DIC confirmed that the specimen central gauge section was under pure shear conditions for the duration of the test (Figure 4.24).

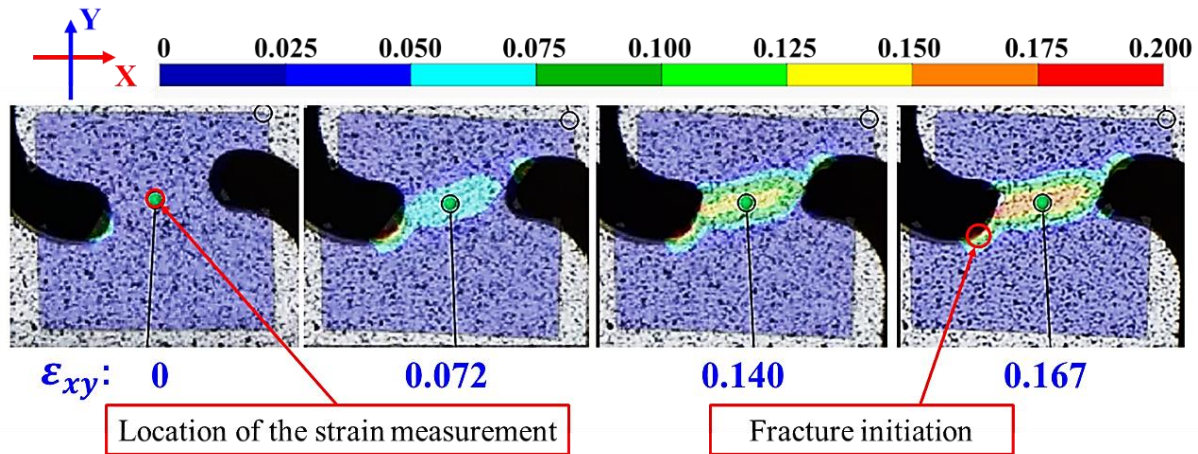


Figure 4.24. The DIC captured shear strain field for a shear specimen analysed at the quasi-static strain rate of 0.0013 s^{-1} (load axis in the x-direction).

4.4.2 Intermediate Strain Rate Shear Test Results

In the intermediate strain rate range, shear tests were performed at two strain rates (16.8 s^{-1} and 28.4 s^{-1}), and for all tests the same specimen geometry and uniaxial test equipment were used (see Section 3.3.3 and 3.4.3). The stress-strain response of the epoxy was similar for both loading rates considered, while there was consistency for all repeated tests with minimal scatter (Figure 4.25). The specimen fractured at approximately 5% strain, which was much lower in magnitude compared to the yield strain of 17 to 20% that was observed for the quasi-static strain rate cases. The result reveals that the specimen was unable to deform up to the yield point due to premature tensile fracture. The stress concentration might be more significant at higher loading rates, initiating fracture at lower strains. Therefore, the specimen geometry considered may not be suitable for intermediate rate testing.

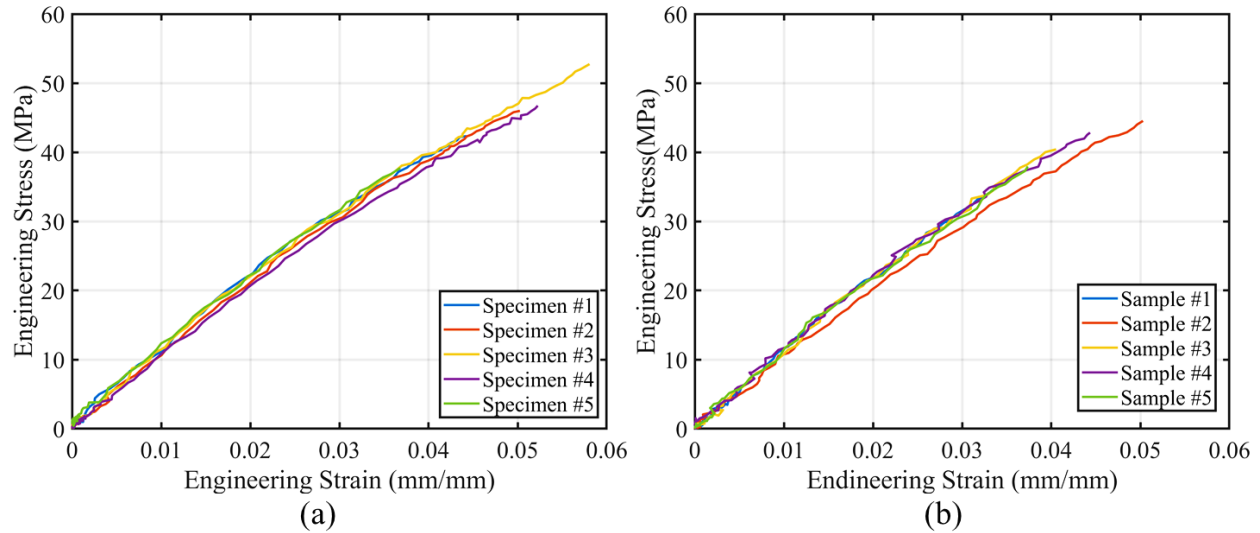


Figure 4.25. Shear engineering stress-strain curves for intermediate strain rates of: (a) 16.8 s^{-1} , and (b) 28.4 s^{-1} . Note, five repeated tests were performed for each strain rate.

4.4.3 Summary of the Shear Test Results

The average shear stress-strain curves for all considered strain rates are combined to assess the strain rate-dependent response of the epoxy (Figure 4.26). Note, only one intermediate strain rate is shown since there is no significant difference between the two intermediate-strain-rate shear tests. The elastic region of the average stress-strain curves is similar in shape, and a higher yield point is expected at a higher strain rate test. The shear modulus and estimated shear strength were carefully determined based on the engineering stress and the engineering strain results, and a 90% confidence interval for each value was calculated (Table 4.4). The shear modulus was not notably influenced over the range of strain rates considered, while the shear yield strength increased by approximately 8% between the two quasi-static strain rates considered.

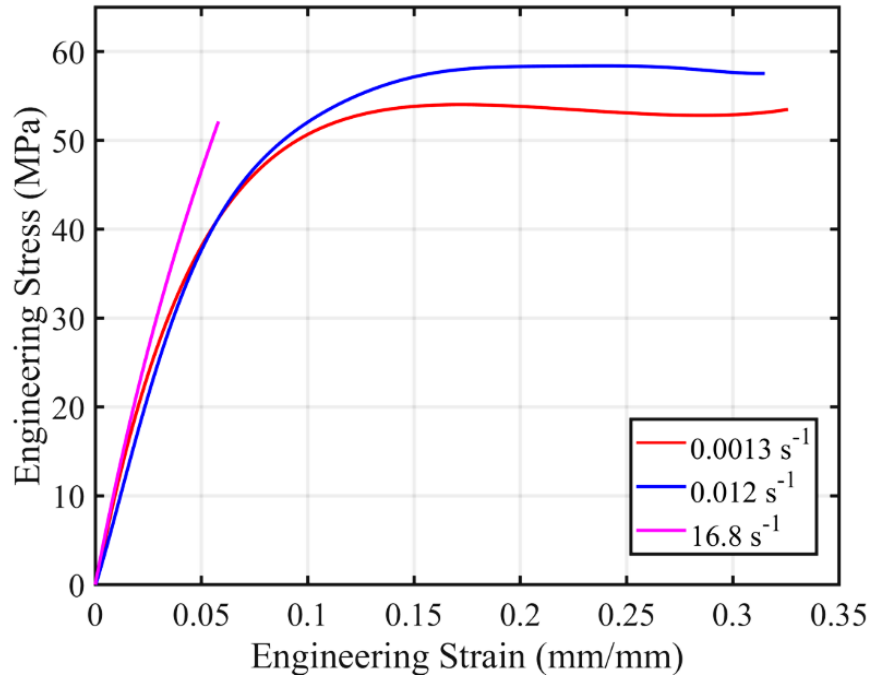


Figure 4.26. Average shear stress-strain response of the epoxy material at the different shear strain rates.

Table 4.4. Summary of mechanical properties for shear tests at different strain rates (90% CI).

| Strain rate | 0.0013/s | 0.012/s | 16.8/s |
|----------------------------|-------------|------------|-----------|
| Shear Modulus (GPa) | 1.02 ± 0.13 | 0.89±0.11 | 1.09±0.08 |
| Shear yield strength (MPa) | 53.37±1.53 | 57.57±2.08 | N/A |

4.5 Fracture Surface Investigation

Investigation of the specimen fracture surfaces was conducted using optical microscopy. The typical failure modes observed for representative test specimens are depicted for the indicated tests (Figure 4.27). All test specimens fractured due to tension (i.e., Mode I). The two tensile specimens fractured in a typical brittle manner with the fracture surface oriented perpendicular to the loading direction (Figure 4.27a and Figure 4.27b). Fracture of the shear specimens initiated at the inner arc because of local tri-axial stresses and the crack propagated toward the outer face along the direction perpendicular to the loading direction (Figure 4.27c). The compression specimens failed as a result of high tensile strains along the specimen radial direction caused by Poisson’s effect, resulting in fracture surfaces in planes parallel to the loading direction (Figure 4.27d).

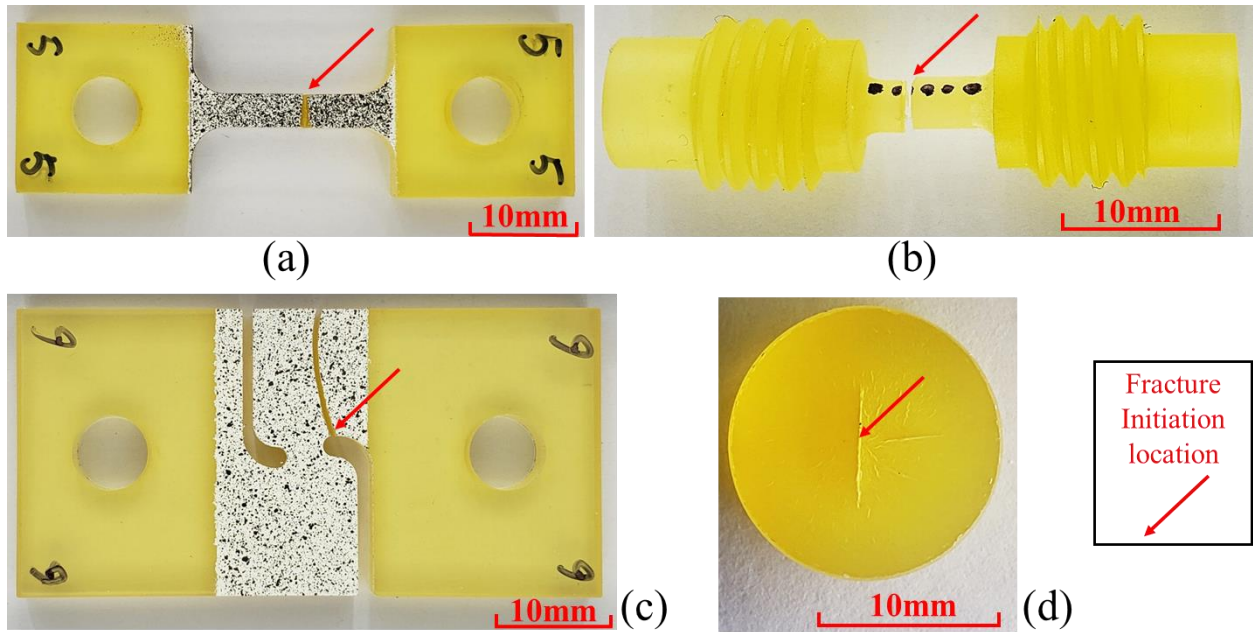


Figure 4.27. Representative specimens tested until failure: (a) quasi-static strain rate tensile test; (b) high strain rate tensile test; (c) intermediate strain-rate shear test; and (d) quasi-static compression test.

The tensile specimens were chosen to investigate the fracture surfaces using a digital optical microscope. Overall, all the tensile specimens fractured in a brittle manner without necking, with similar fracture pattern for all tested strain rates. This indicates that although the stress-strain curves in Figure 4.4 exhibit some degree of ductility, the epoxy is sufficiently brittle and the mechanisms leading to fracture do not change with strain rate. Figure 4.28 shows the typical fracture pattern observed, revealing that the crack propagation follows several well-known stages for thermosetting polymers: mirror-like, smooth with parabolas, hackle, and rough [119]. The fracture process initiates at a local defect on the specimen surface, which may be a void or a machining mark. Thereafter, the crack propagates at a slow rate, creating a smooth and patternless surface, often call mirror-like stage (Figure 4.28a). As the crack propagation speed increases with the increase of applied stress, parabolic patterns appear due to the formation of secondary crack (Figure 4.28 b), referred to as smooth with parabolas stage. During the subsequent hackle stage, ellipse shape patterns are formed when the primary crack propagation speed increases as shown in Figure 4.28c. During the final stage, the abrupt fracture of the specimen creates rough surfaces and complex patterns (Figure 4.28d). Figure 4.29 shows the fracture surface of the tensile specimen under dynamic loading. Comparing to the quasi-static strain rate tensile test, the fracture surface for the dynamic tensile test has similar patterns, but the mirror-like, smooth with parabolas and hackle stage areas are much smaller.

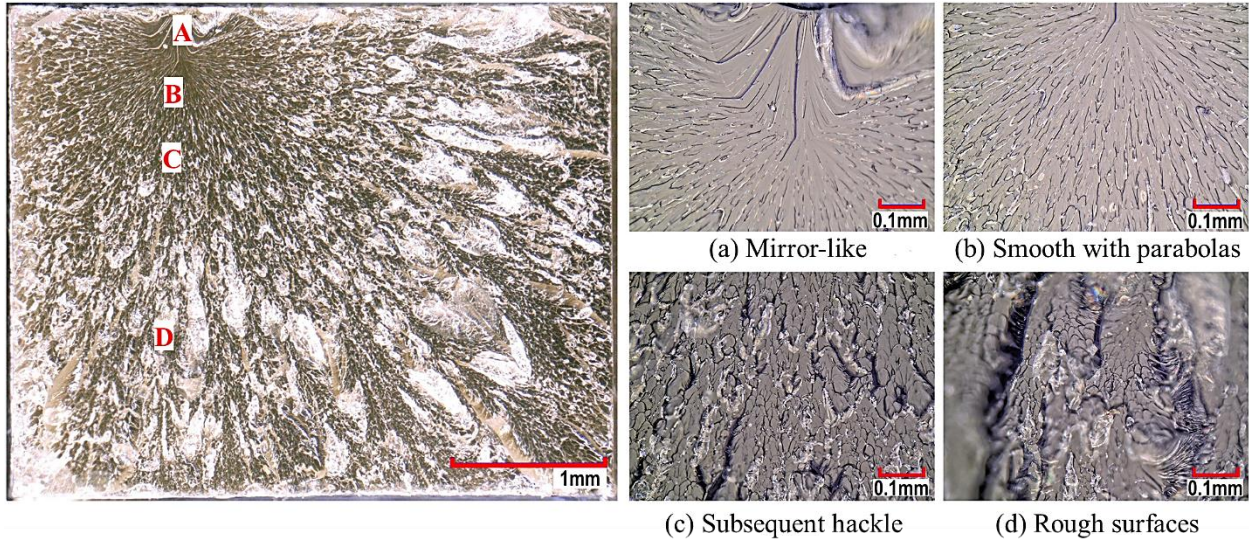


Figure 4.28. Fracture surface images for the quasi-static strain rate tensile test specimen (0.00033 s^{-1}).

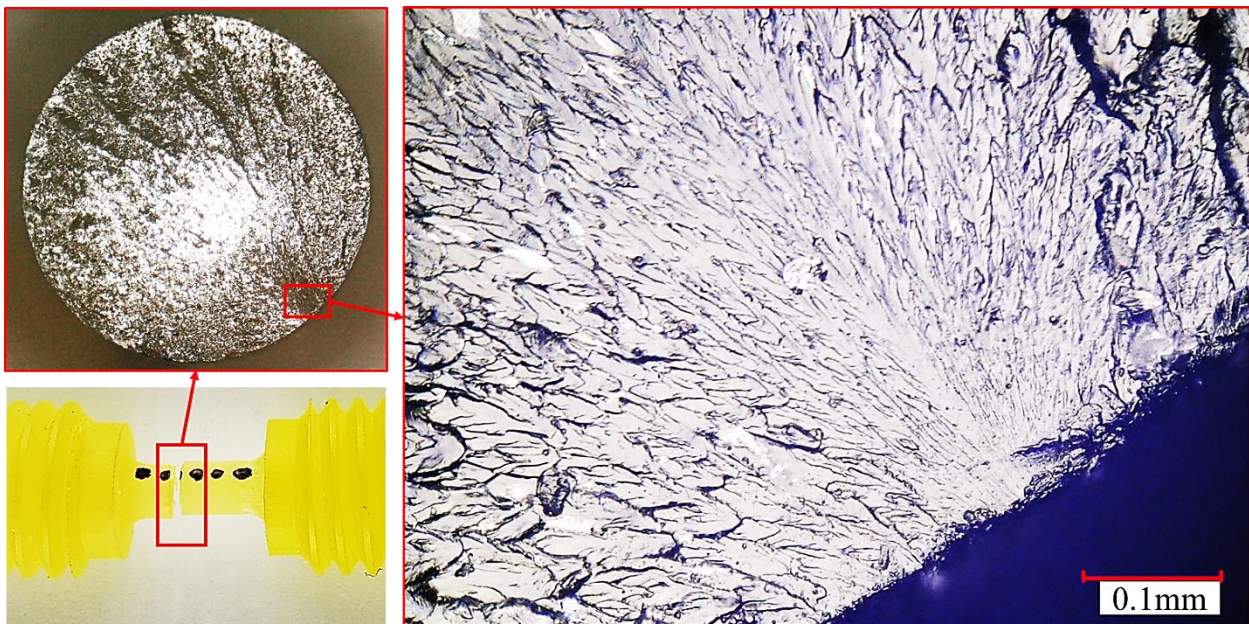


Figure 4.29. Fracture surface images for the high strain rate tensile test specimen (300 s^{-1})

Chapter 5 Epoxy Constitutive Modeling Fitting and Validation

This chapter presents the details of the identification of a suitable constitutive model to represent the epoxy material in a commercial finite element program, Abaqus. Furthermore, the calibration method of the material model used in this study, as well as the material model verification, and the independent validation test simulations are discussed.

5.1 Material Model Identification for the Epoxy

In this study, the constitutive model was identified from the standard material model library in Abaqus, eliminating the need to create a custom user-defined material model. Based on the material characterization results, a summary of the critical characteristics that the material model should ideally meet was collected (Table 5.1).

Table 5.1. A summary of assumptions for the material model.

| Material Behaviour | Assumption |
|---------------------------------|--|
| Strain rate dependence | The epoxy exhibited a clear strain-rate dependent behaviour. This characteristic is an important feature that the studied material model must describe. |
| Hydrostatic pressure dependence | The distinct yield behaviour in tension and compression confirmed the pressure dependent response of the epoxy. This property was not intended to capture by the current material model. |
| Temperature dependence | The temperature dependence was not investigated in this study. Given the fact that the composite structure tends to fragment into tiny pieces during impact [9], the limited plastic deformation might limit the degree of adiabatic heating during deformation. |
| Directional dependence | Material characterization tests revealed that the mechanical response of the epoxy is isotropic. |
| Large deformation | The observed strain softening and re-hardening response that occurred for large compressive deformations was neglected for the current study since for a fiber-reinforced composite material the constrained epoxy is expected to undergo low local strains (<5%). |
| Unloading | The unloading behaviour of the epoxy were not considered in the current impact study. |

To identify a material model to meet all the assumptions, an investigation of the available constitutive models for glassy polymers was conducted, and the key feature for the targeted material model was the strain rate dependence. Material libraries in commercial FE software (e.g., Abaqus) provides a large number of material models that can describe the comprehensive behaviours of materials [98]. The assessment of the existing strain rate-dependent material models in the commercial FE software led to the conclusion that the strain rate-dependent response of glassy polymers could be modelled using either an elastic-plastic or viscoelastic material model. As discussed in Section 2.3, viscoelastic material models are not suitable for glassy polymers exhibiting plastic deformations. Therefore, the elastic-plastic constitutive models were considered for the studied epoxy. It should be noted that use of a metal elastic-plastic model to simulate the nonlinear stress-strain response of epoxy resins might produce inaccurate predictions during large deformation and unloading or cyclic loading conditions [92]; however, these situations were not considered in this study. Metal elastic-plastic models also assume that the elastic modulus of the material is constant, which was not always the case for the epoxy materials [120]. A viscoplastic constitutive model, which requires the development of a user-defined material subroutine and is beyond the scope of this study, may provide an improved description of the polymer stress-strain behaviour.

The candidate elastic-plastic constitutive models with strain rate effects were investigated. In Abaqus, the elastic and plastic parts of the material model were defined individually. For the elastic part, isotropic and shear (equation of state) can be used in conjunction with plasticity models. Since the material characterization results revealed that the epoxy resin exhibited an isotropic elastic response, the isotropic linear elastic model was selected to model the elastic portion of the response. For the plasticity models, there are ten different options currently available in Abaqus (Table 5.2). Out of the ten plasticity models, the classical metal and Drucker-Prager models are suitable for polymeric materials. Comparing these two plasticity models, the classical metal model is suitable for crash analysis, while the Drucker-Prager model has a pressure-dependent yield function, which is important for the glassy polymers. However, the Drucker-Prager plastic model requires additional tri-axial test data at different levels of confining pressure to calibrate the model, which requires a special test instrument [98]. Thus, the classical metal plasticity model was selected for this study.

Table 5.2. Summary of the plasticity models in Abaqus [98].

| Plasticity models | Description | Target material |
|-------------------------------------|---|---|
| Classical elastic-plastic isotropic | Used for crash analysis, metal forming, and general collapse studies. | Metal |
| Cap | Used for cohesive geological materials with a pressure-dependent yield. | Soils and rocks |
| Cast iron | Designed for gray cast iron. | Gray cast iron |
| Clay | Defines the yield function by three stress invariants, and the plastic strain rate is controlled by an associated flow rule. | Clays |
| Concrete damaged | Used for concrete and other quasi-brittle materials. | Concrete |
| Concrete smeared cracking | Designed for concrete subjected to virtually monotonic strain at low confining pressures. | Concrete |
| Crushable foam | Used to analyse crushable foams that are used as energy absorption structures. | Foams |
| Drucker-Prager | Used for frictional materials that exhibit pressure-dependent yield. Also, used for materials with higher compressive yield strength than the tensile yield strength. | Granular-like soils and rock; composite and polymeric materials |
| Mohr-coulomb | Designed for materials that follow classical Mohr-Coulomb yield criterion. | Concrete and rubble piles; soils and rocks |
| Porous metal | Used for materials with a dilute concentration of voids (a relative density greater than 90%). | Porous metal |

The classical metal plasticity is an incremental plasticity model that decomposes the strain into elastic and plastic parts [98]. As discussed in Section 2.3.1, this type of model is formulated based on three elements, including a yield function or criterion, a flow rule and a hardening law. The Mises yield surface was used for the current material model. Abaqus uses associated plastic flow for the classical metal plasticity model, which means the plastic potential (g) is the yield function. In terms of hardening rule, the Johnson-Cook plasticity-hardening rule was selected due to the strain rate-dependent capabilities (Table 5.3). To incorporate the rate-dependent hardening behaviour into the Johnson-Cook plasticity model, the true plastic stress-strain behaviour of the material at the lowest strain rate was input into the model to determine the stress-strain response at the higher strain rates.

Table 5.3. Summary of plasticity hardening laws in Abaqus [98].

| Hardening | Description |
|------------------|--|
| Isotropic | Isotropic hardening assumes that the yield surface expands uniformly in all directions during plastic deformation. |
| Linear Kinematic | Linear kinematic assumes a constant rate of hardening. It is a pressure-independent plastic model that is used for simulating a material under cyclic loading conditions. |
| Johnson-Cook | Johnson-Cook hardening is a specific type of isotropic hardening rule. The yield stress is governed by a given analytical function of equivalent plastic strain, strain rate, and temperature. The benefit of this model is that it is favourable for predicting the high strain-rate deformation of many materials. |
| User | The material hardening can be defined through a user subroutine. |
| Combined | The nonlinear combined hardening combines isotropic and kinematic hardening. This hardening provides better predictions than kinematic hardening but requires detailed calibration. |

5.2 Calibration Method for the Constitutive Material Model

The calibration of an elastic-plastic material model can be divided into two parts: elastic and plastic (Figure 5.1). For the elastic part of the calibration, the only material parameter was the elastic modulus, which can be acquired directly from the material characterization. The plastic part of the calibration was critical and required some steps to calibrate the plasticity model. For a Johnson-Cook plasticity model, the yield stress of a material can be expressed as:

$$\bar{\sigma} = \left[A + B(\bar{\epsilon}^{pl})^n \right] \left[1 + C \ln \left(\frac{\dot{\bar{\epsilon}}^{pl}}{\dot{\epsilon}_0} \right) \right] (1 - \hat{\theta}^m) \quad (5.1)$$

where

$\bar{\sigma}$ is the yield stress at nonzero strain rate;

$\bar{\epsilon}^{pl}$ is the equivalent plastic strain;

$\dot{\bar{\varepsilon}}^{pl}$ is the equivalent plastic strain rate;
 $\dot{\varepsilon}_0$ is the plastic strain rate at the lowest strain rate states;
 $\hat{\theta}$ is the nondimensional temperature (not applicable in this study);
 $A, B, n, C,$ and m are the material parameters.

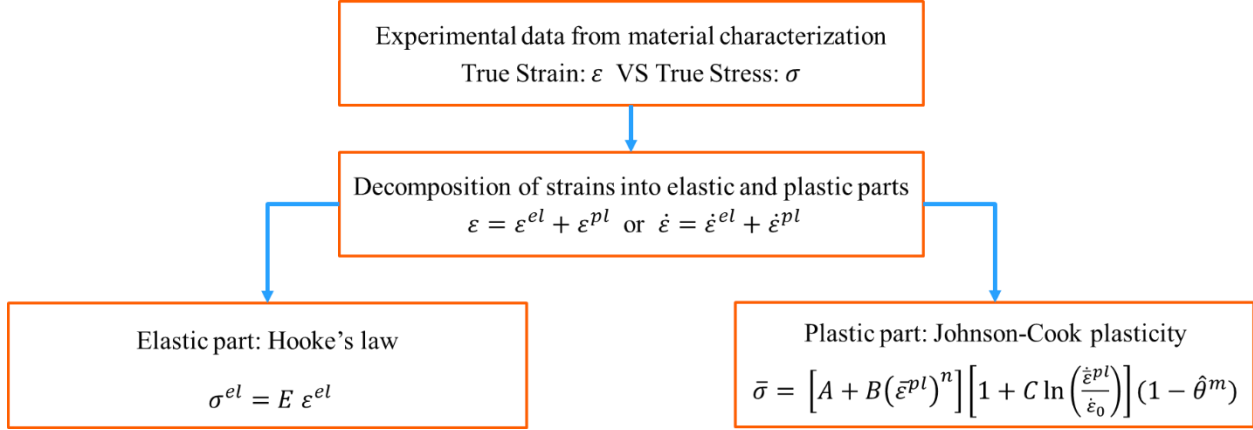


Figure 5.1. Diagram of a general calibration procedure for an elastic-plastic material model.

In the current study, the tensile tests provided a more complete data set than compression tests, and the material failure was dominated by tension mode. Moreover, the Johnson-Cook plasticity model cannot describe the strain softening and re-hardening behaviours of the epoxy material observed in compression loading. Thus, the uniaxial tensile data were used to calibrate the material parameters, without considering the compression and shear. In the experiments, engineering stress (σ_e) and engineering strain (ε_e) were measured. However, the material model required true stress and logarithmic (true) strain, determined using an assumption of constancy of volume (Equation 5.2).

$$\begin{aligned}\varepsilon_t &= \ln(1 + \varepsilon_e) \\ \sigma_t &= \sigma_e(1 + \varepsilon_e)\end{aligned}\quad (5.2)$$

In the monotonic loading condition, the equivalent stress is the same as the uniaxial stress, while the equivalent plastic strain ($\bar{\varepsilon}^{pl}$) is equal to the axial plastic strain (ε^{pl}) [99]. Thus, the plastic strain was decomposed from the true total strain using Equation 5.3, where E is the elastic modulus.

$$\bar{\varepsilon}^{pl} = \varepsilon^{pl} = \varepsilon_t - \varepsilon^{el} = \varepsilon - \sigma_t/E \quad (5.3)$$

The next step was to determine the material parameters A , B and n in Equation 5.1. When the $\dot{\epsilon}^{pl}$ was equal to the $\dot{\epsilon}_0$ at the lowest strain rate, the strain rate dependent term, $\left[1 + C \ln\left(\frac{\dot{\epsilon}^{pl}}{\dot{\epsilon}_0}\right)\right]$, became 1. As the temperature term $\hat{\theta}$ was ignored in this study, the Equation 5.1 became

$$\bar{\sigma} = \left[A + B(\bar{\epsilon}^{pl})^n \right] \quad (5.4)$$

To determine the material parameters A , B and n in the Johnson-Cook plasticity model, the first step was to determine the basic curve σ_y^0 (Figure 5.2). In this case, the basic curve σ_y^0 was the yield stress versus true plastic strain for the lowest strain rate tests. There were two methods to incorporate the σ_y^0 into Abaqus. The first method was to input the experimental data points, allowing Abaqus to calculate the model parameters internally. Another method was to determine the coefficients of Equation 5.4 a priori and then input the coefficients into Abaqus. In this study, a curve fitting using the MATLAB curve-fitting tool was conducted to determine the coefficients A , B and n for Equation 5.4.

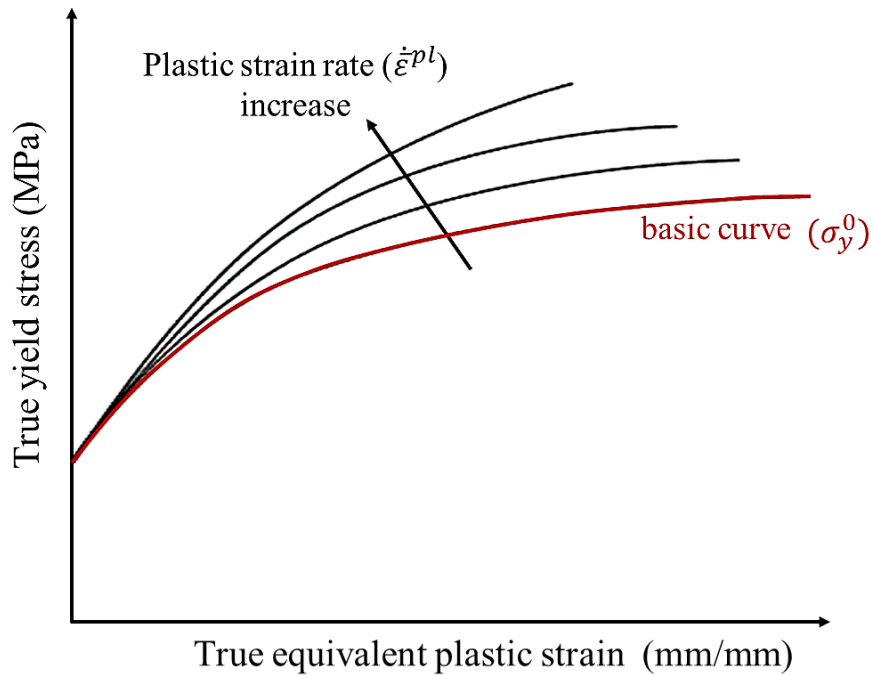


Figure 5.2. Strain rate dependent of the true plastic stress-strain curves.

In the final step, the strain rate dependent parameter, C , was calibrated using multiple yield stress versus plastic strain curves at different equivalent plastic strain rates. In the strain rate term, $\left[1 + C \ln \left(\frac{\dot{\epsilon}^{pl}}{\dot{\epsilon}_0}\right)\right]$, each $\dot{\epsilon}^{pl}$ corresponds to one set of yield stress versus plastic strain data. The calibration was performed in MATLAB using a custom algorithm. Different values of C were introduced into the strain rate term, and one set of yield stress versus plastic strain curves was calculated for each C value. The calculated yield stress versus plastic strain curves were compared with the experimental data sets, and the coefficient of determination between the calculated and the experimental data was computed. The parameter C was determined as the value that gave the highest coefficient of determination.

5.3 Verification and Validation Methods for the Material Constitutive Model

The material model verification was conducted using single-element tests in Abaqus, while the validation was performed by comparing independent tests that used complex specimen geometry with the corresponding FE simulation results.

5.3.1 Single Element Material Constitutive Model Verification

After all the material parameters were calibrated, the verification of the material model with experimental data at different strain rates was conducted using single-element tests. For all simulations, an 8-node brick solid element was created, material properties were assigned, and boundary conditions were imposed. For the uniaxial tensile single element test, the bottom face of the element was fixed in the Y direction with one node ENCASTRE, while a 0.1 or 10% strain was applied on the top surface along the Y direction (Figure 5.3). When the total applied strain is fixed, different strain rates can be achieved by changing the total applied time-period in the step manager (Table 5.4). The shear single-element simulation was conducted at the quasi-static strain rate (0.0013 s^{-1}) using the test method by Dienes [121]. For the boundary conditions, nodes 1, 2, 3, 4 at the bottom face of the element were fixed in the X, Y, and Z directions (Figure 5.4). Nodes 5, 6, 7, 8 at the top face of the element were fixed at the Y and Z directions, and a 0.0013 mm/s velocity in X direction was applied to the four nodes (Figure 5.4). After each simulation (one for each strain rate), the logarithmic strain and stress along the strain-direction were collected and plotted. These simulation results were used to compare with the experimental tensile test results to verify the accuracy of the material model.

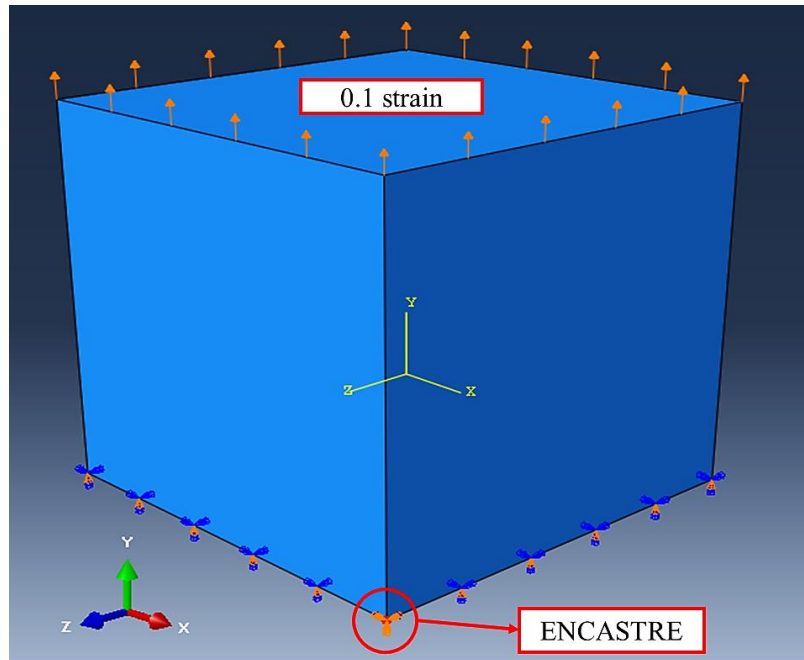


Figure 5.3. Tensile single element and its boundary conditions.

Table 5.4. Summary of the period setup for the tensile single-element tests

| Strain rate (s^{-1}) | 0.0056 | 3 | 30 | 300 |
|--------------------------|--------|---------|---------|---------|
| Time period (s) | 1.79e1 | 3.33e-2 | 3.33e-3 | 3.33e-4 |

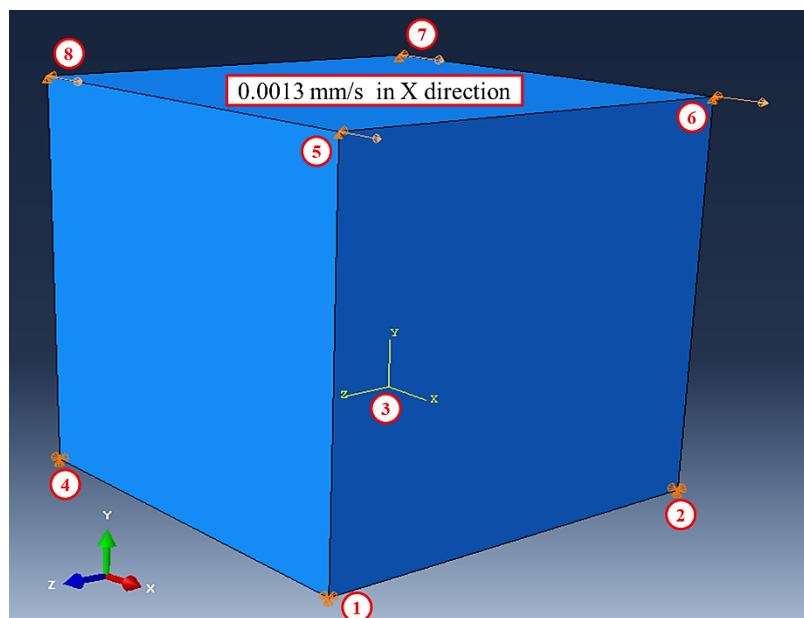


Figure 5.4 Shear single element and its boundary conditions

5.3.2 Material Constitutive Model Validation

Independent tests were conducted to validate the material model for the case where the epoxy exhibits non-uniform stress states (Section 3.4.7). FE models of the validation test specimens were developed to represent the specimen geometry and the test setup. The element type was solid and homogeneous, and the element geometry was hex-dominated with a 1:1:1 aspect ratio. However, the 1:1:1 aspect ratio was not achieved for every element in the FE models due to the complex specimen geometry (Figures 3.15 and 3.16). A mesh sensitivity study was conducted over a mesh size of 0.2 mm to 1 mm with 0.1 mm increments. Two rigid-body-pin constraints were assigned between the center of the pin-hole (reference point) and half pin-hole surfaces to represent the actual tests (Figure 5.5). Any boundary condition applied to the reference point would simultaneously be assigned to the corresponding half pin-hole surfaces due to the rigid constraints. The center reference point of the hole was fixed, while the velocity was applied to the other reference point with the same velocity as the crosshead setup (Figure 5.5). The simulation model for the asymmetric specimen was similar to that of the symmetric specimen.

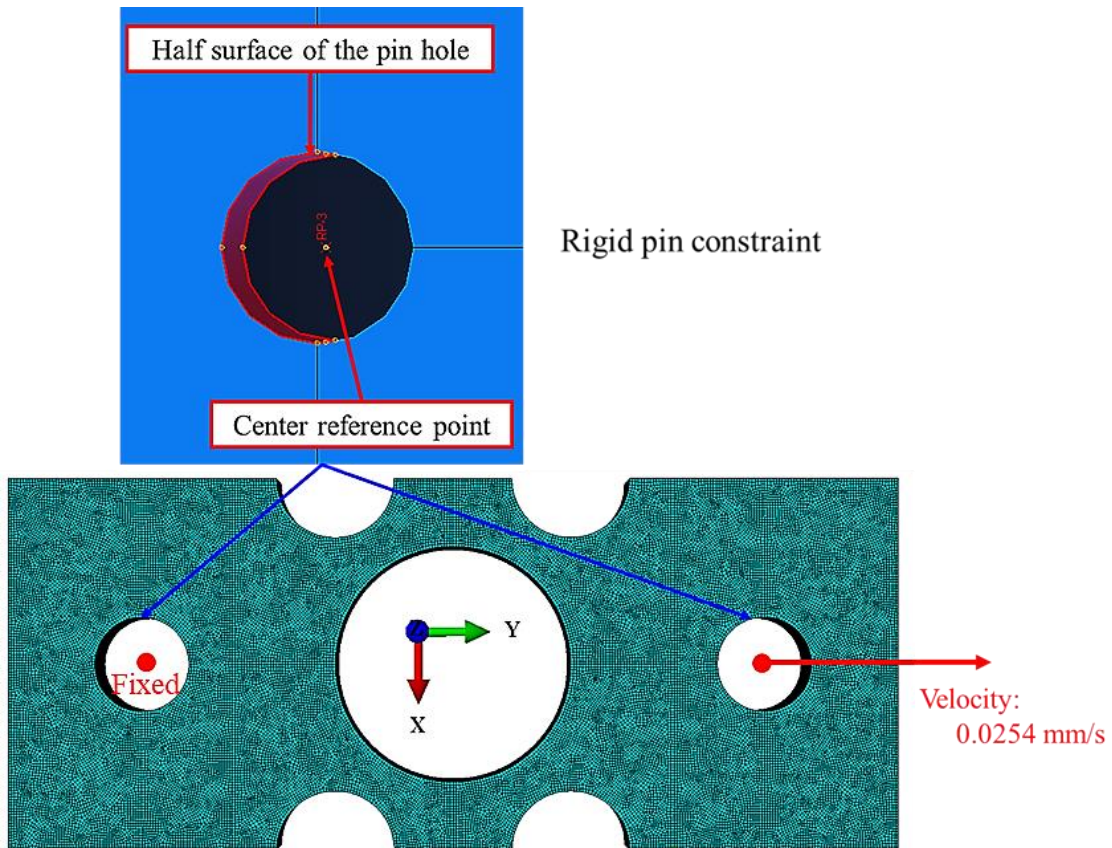


Figure 5.5. A rigid-body-pin constrains the outer half of the pin-hole surface to the center reference point in the FEA model for the symmetric specimen (Solid element with 0.2 mm mesh size, 655,006 elements).

5.4 Calibration Results of the Constitutive Modelling Results

To calibrate the parameters of the elastic-plastic material model, as described in Section 5.2, the true yield stress and true plastic strain were calculated from the engineering stress and engineering strain (Figure 5.6). Since the high strain rate stress-strain response was almost linear, there was no plastic strain component to decompose for those tests. Once the true yield stress and true plastic stress were calculated, the parameters A , B , and n in Equation 5.1 were determined by fitting the true yield stress versus true plastic strain data at the 0.00033 s^{-1} strain rate using MATLAB. The curve fitting method and the result are listed (Table 5.5).

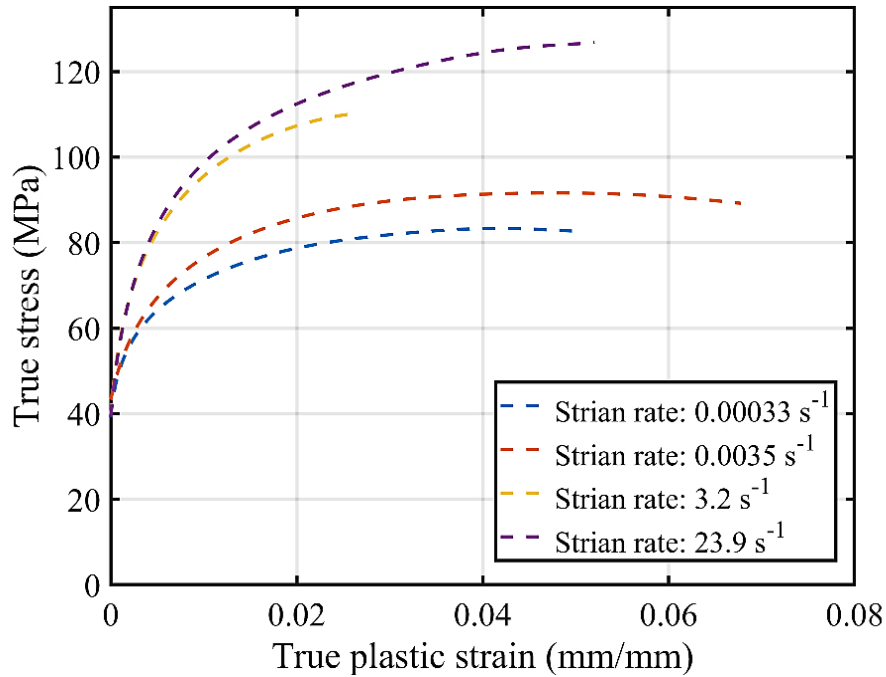


Figure 5.6. The true yield stress versus true plastic strain average experimental data for the tensile tests at different strain rates.

Table 5.5. The curve fitting method and results of Johnson-Cook material parameters for the basic curve.

| Material parameters | | | Curve fitting setting | | |
|---------------------|----------|--------|-------------------------|--------|--------------|
| A | B | n | Method | Robust | Algorithm |
| 19.2MPa | 114.6MPa | 0.1761 | Nonlinear Least Squares | Off | Trust-Region |

Using the material parameters in Table 5.5, the Johnson-Cook plasticity model was plotted and compared with the experimental data, and the coefficient of determination (R^2) was calculated to quantify

the accuracy of the model fit (Figure 5.7). Overall, the calibrated Johnson-Cook plasticity model reasonably represents the experimental stress-strain behaviour of the material in the plastic region. In the 0 to 0.8% true plastic strain range, the model and the experimental data correlate well. As the true plastic strains increase from 0.8 to 3%, the true stress value predicted by the model was slightly lower than the experimental values. Finally, for true plastic strains > 4%, the model predicts higher true stress values than the experimental data, and the differences between model prediction and experimental value are expected to become larger as the strain increased in this region. It should be noted that the total true strain is the true elastic strain plus the true plastic strain. For unidirectional CFRPs in a related study [8], the experimental global failure strains of the CFRPs were approximately 1 to 1.5% true strain depending on the test direction; however, the local failure strains of the resin could be notably higher than the global failure strains of the CFRPs.

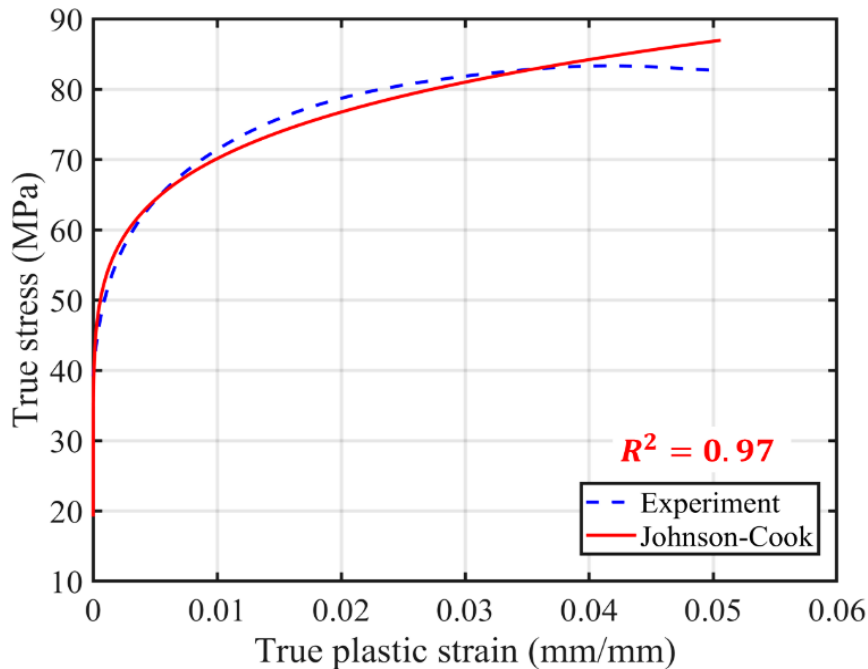


Figure 5.7. A comparison between the Johnson-Cook plasticity model (excluding rate dependence) and the corresponding experimental data (0.00033 s^{-1}).

The next step of the calibration process was to determine the strain-rate dependent parameters, which was performed by fitting three true yield stress versus true plastic strain curves at the higher strain rates ($\dot{\epsilon}^{pl} = 0.0035, 3.2, \text{ and } 23.9 \text{ s}^{-1}$). When the lowest true plastic strain rate was fixed ($\dot{\epsilon}_0 = 0.0005 \text{ s}^{-1}$), only the parameter C in the strain rate dependency term ($1 + C \ln\left(\frac{\dot{\epsilon}^{pl}}{\dot{\epsilon}_0}\right)$) was required to be determined. To

determine the parameter that provides the best fit for all three higher strain rate curves, the coefficients of determination for each curve fittings were calculated and summed using different parameter values (Figure 5.8). Based on Figure 5.8, the value of 0.05 provides the maximum sum of coefficients of determination, and it is assigned to the strain rate-dependent parameter C . The strain rate-dependent parameters for the Johnson-Cook plasticity model are listed (Table 5.6).

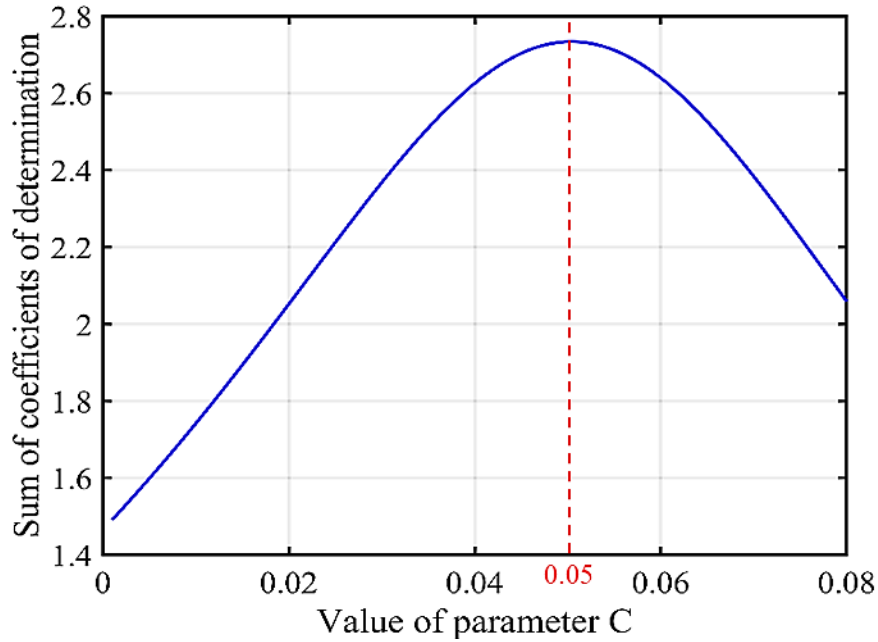


Figure 5.8. Sum of three coefficients of determination for fitting the three curves (strain rates of 0.0035, 3.2, and 23.9 s^{-1}) versus the strain rate-dependent parameter C

Table 5.6. Strain rate-dependent parameters for the Johnson-Cook plasticity model.

| C | $\dot{\epsilon}_0$ |
|------|--------------------|
| 0.05 | $0.00033s^{-1}$ |

To verify the calibration accuracy of the Johnson-Cook plasticity model, the determined material parameters were assigned to the constitutive model and the material plasticity at different strain rates was predicted using a MATLAB script. The analytical simulation results were compared with the experimental results (Figure 5.9), revealing a good agreement with the tensile experimental results.

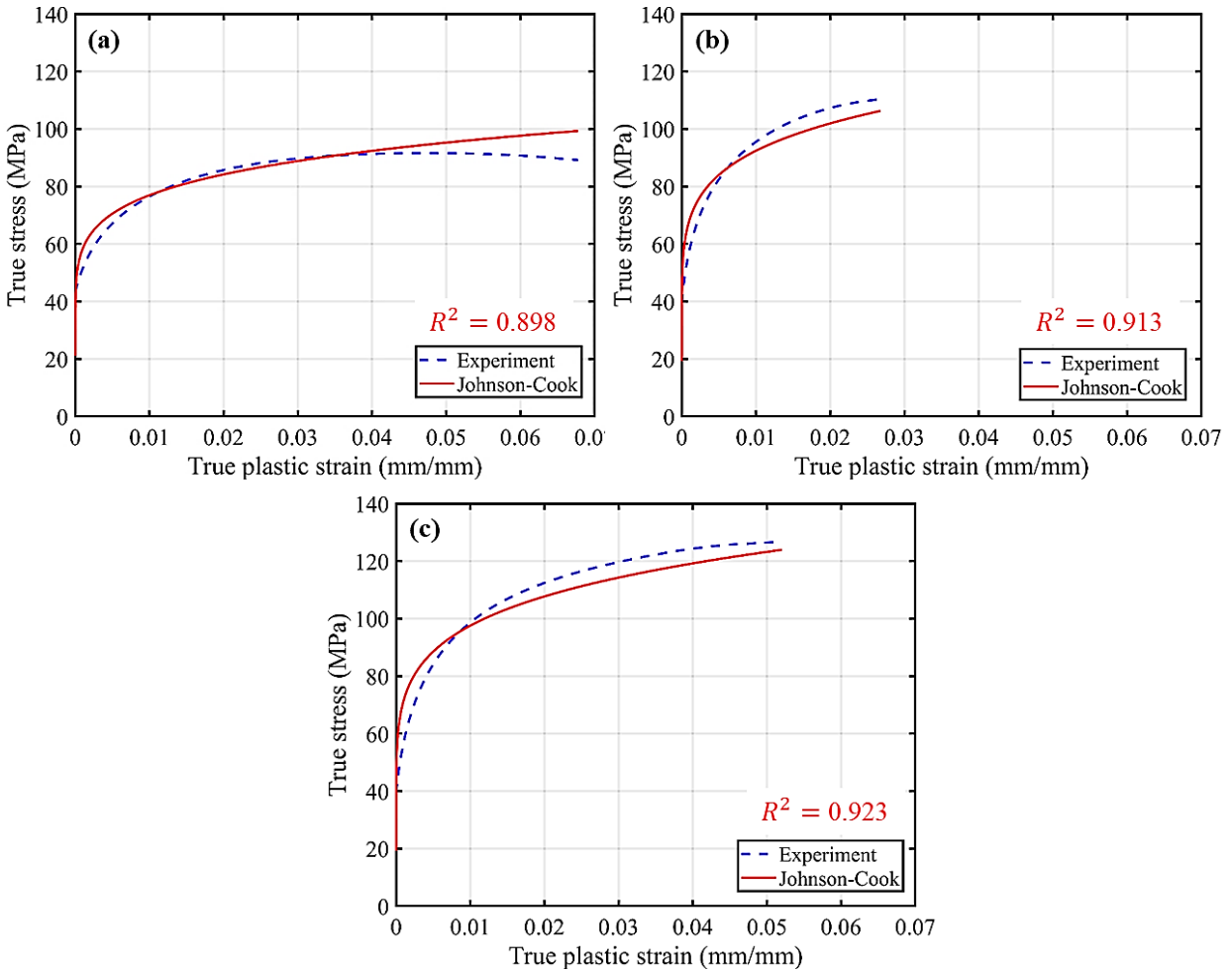


Figure 5.9. Comparisons of true stress and true plastic strain data from the Johnson-Cook plasticity rate dependent model and the corresponding experiments: (a) the strain rate of 0.0035 s^{-1} ; (b) the strain rate of 3.2 s^{-1} ; (c) the strain rate of 23.9 s^{-1} .

5.5 Single Element Material Model Verification Results

Following the procedure of the single-element material model verification discussed in Section 5.3.1, all the calibrated material parameters were assigned to the FE model in Abaqus. One important consideration for the material model was to select a constant elastic modulus for the element, which is an assumption of the chosen material model. However, the elastic modulus of the epoxy material exhibited a strain rate dependency (Table 4.2 and Figure 4.10). Since this material was targeted for a dynamic loading condition, a higher elastic modulus value was favoured. After several iterative simulations, the value of 3.35 GPa was identified as it provided a good overall correlation between the single-element predictions and the experimental data, especially in the intermediate and high strain rate range (Figure 5.10).

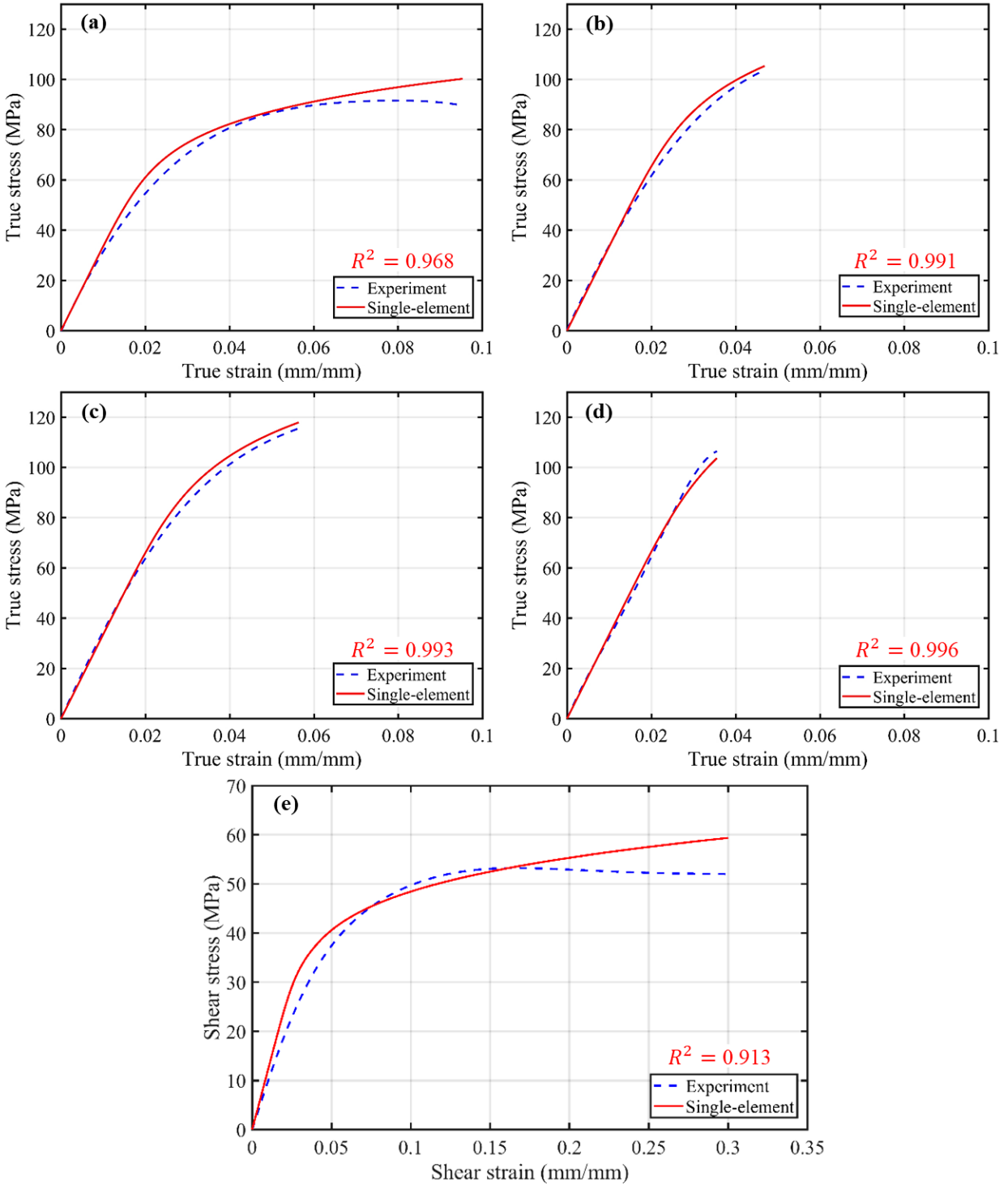


Figure 5.10. Comparisons of true stress-strain data for the single-element simulations with corresponding experiments: (a) tensile strain rate of 0.0035 s^{-1} ; (b) tensile strain rate of 3.2 s^{-1} ; (c) tensile strain rate of 23.9 s^{-1} ; (d) tensile strain rate of 300 s^{-1} ; (e) shear strain rate of 0.0013 s^{-1} .

5.6 Material Model Validation Results

To validate the calibrated material model for the case where the material is subjected to a complex stress state, independent tests were performed (see Section 3.4.7) and simulated using a developed FE model (see Section 5.3.2). A mesh sensitivity study was initially conducted for the symmetrical specimen model over a range of mesh sizes from 0.2 mm to 1 mm. Using the same FE model with different mesh sizes, the true average strain values for a defined path in an identified critical zone of the specimen along the x-axis were investigated (Figure 5.11). First, true average strain along the defined path for simulation models with mesh sizes of 0.2 to 1 mm at 0.2 mm increments were plotted and compared (Figure 5.12 a). There was a notable variation of the true average strain for the mesh sizes considered, with little variation in strain for simulations of 0.2 mm and 0.4 mm mesh sizes other than at the ends of the defined path. A further investigation of the mesh size from 0.2 to 0.4 mm with 0.1 mm incensement was conducted (Figure 5.12 b). The result confirms that the overall behaviour of the average true strain-distance plots was the same, with some differences at both ends of the path. In this study, a 0.3 mm mesh size was selected to balance computational efficiency and accuracy.

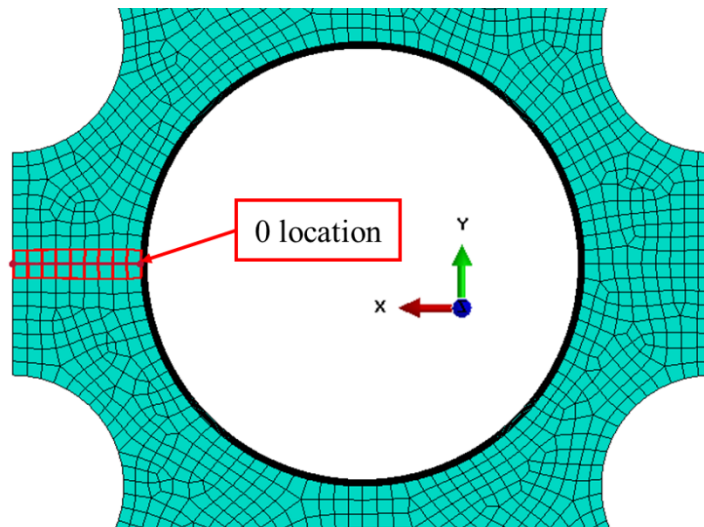


Figure 5.11. The critical area of the specimen used for the mesh sensitivity study.

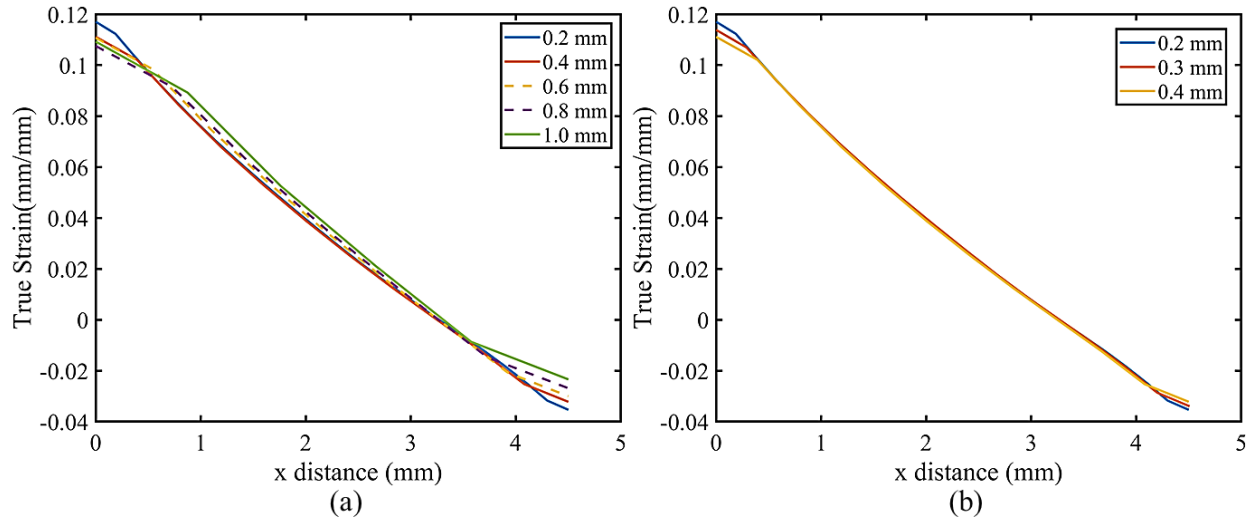


Figure 5.12. The true average strain values at different x-locations from the critical area of the specimen using different mesh sizes: (a) mesh sizes of 0.2 to 1 mm at 0.2 mm increment; (b) mesh sizes of 0.2 to 0.4 mm at 0.1 mm increment.

Strain maps captured during the validation tests were compared with the FE model simulation results for the symmetric specimen (Figure 5.13). Overall, the FE models captured the strain fields of the symmetric specimens, where the maximum magnitudes of strain were in good agreement. However, the FE simulation models slightly over-predicted the strain values at zones where strains were measured in the range of approximately 4 - 7 % (Figure 5.13c). This result agrees with the single-element test because the material model over-predicts the stress-strain response at the quasi-static strain rate region. Another difference was that the outer edge areas of the specimen in the FE model showed notable compression strain (Figure 5.13a), while the validation specimen captured little or no compression strain in these areas. One explanation could be that machining defects on the outer surfaces of the specimens create weak areas and offset the strain in other areas. As indicated in Figure 5.13, in comparison to the FE model, the edges of the validation specimen show higher magnitude of strains. Similar comparative results for the asymmetric specimens were also observed (Figure 5.14).

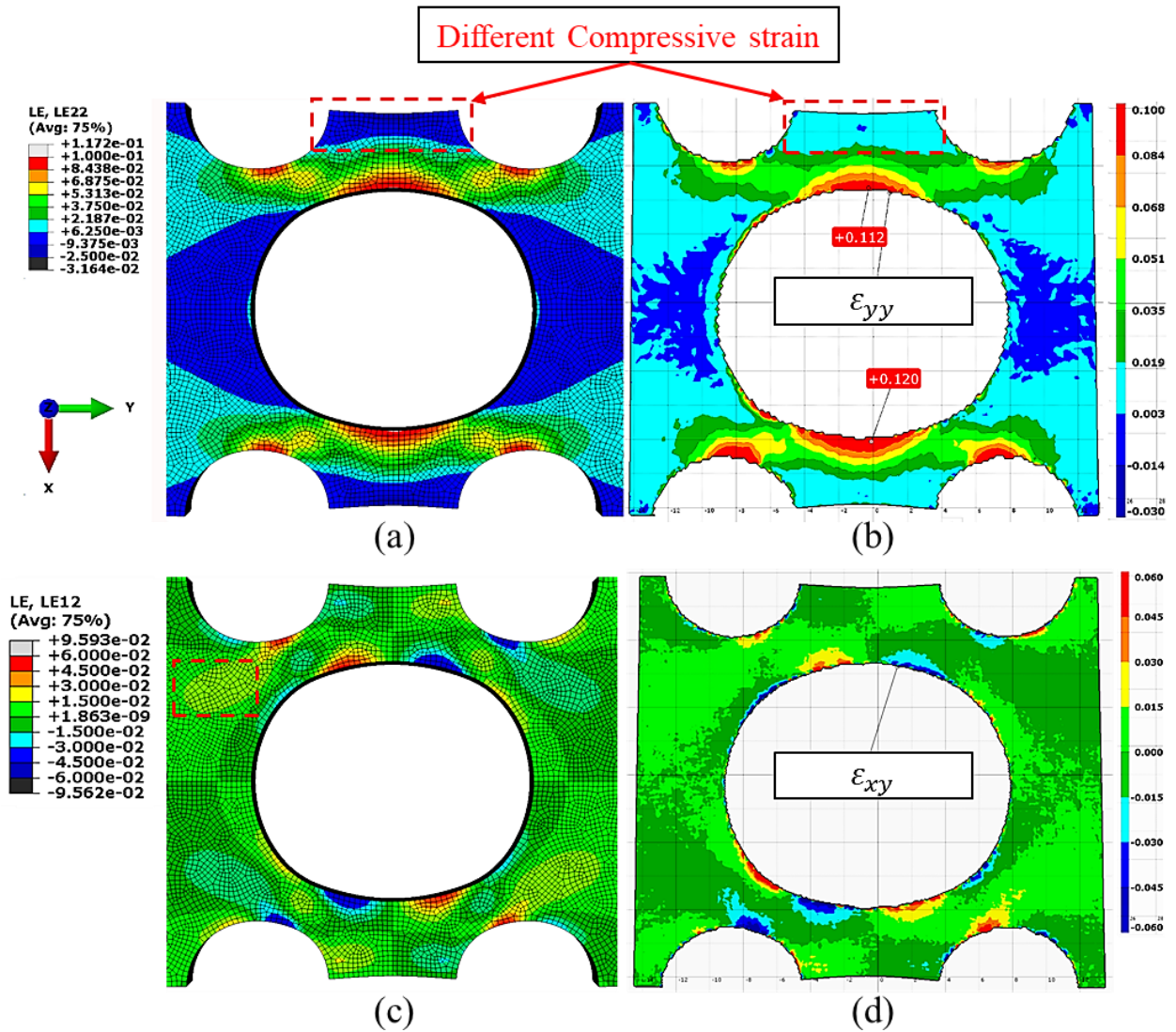


Figure 5.13. Comparisons of the strain field of the symmetric specimens for validation tests and the FE models simulations: (a) ϵ_{yy} of the FE model simulation; (b) ϵ_{yy} of the validation test (DIC); (c) ϵ_{xy} of the FE model simulation; (d) ϵ_{xy} of the validation test (DIC).

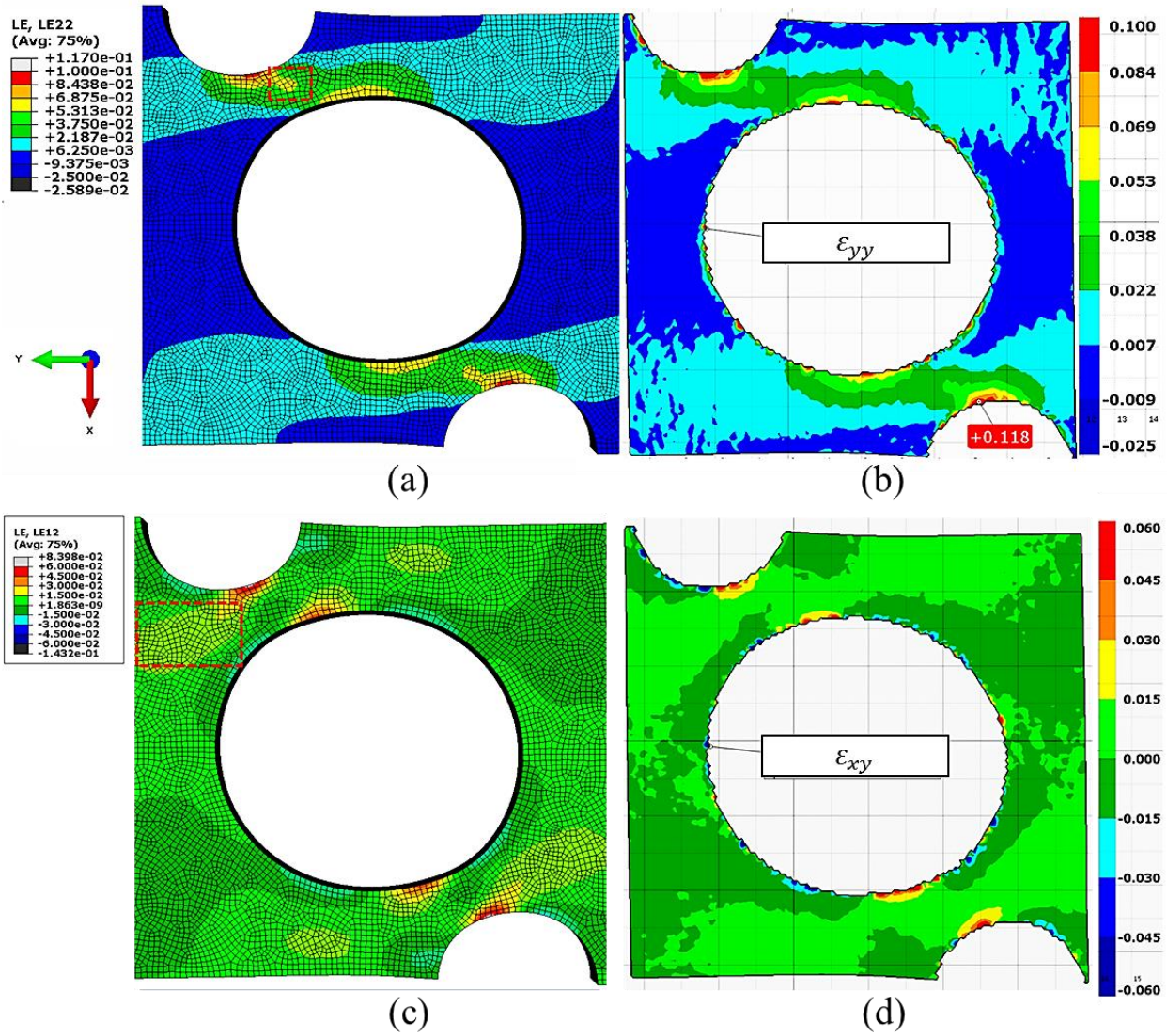


Figure 5.14. Comparisons of the strain field of the asymmetric specimens for validation tests and the FE models simulations: (a) ϵ_{yy} of the FE model simulation; (b) ϵ_{yy} of the validation test (DIC); (c) ϵ_{xy} of the FE model simulation; (d) ϵ_{xy} of the validation test (DIC).

Chapter 6 Discussion

In this chapter, a general discussion of the mechanical characterization results of the studied epoxy material is provided, focusing on the strain rate dependent response of the material. Moreover, the elastic-plastic constitutive model used for the epoxy material is discussed, including the limitations.

6.1 Mechanical Characterization

A summary of all the tensile and compressive characterization results at different strain rates reveals some key features of the strain rate sensitivity for the studied epoxy (Figure 6.1). First, the tensile and compressive stress-strain behaviour is clearly dissimilar because of the different exhibited failure strains and the post-yield responses. During compressive loading, the studied epoxy showed notable strain softening and strain re-hardening behaviour after yielding (Figure 6.1). The quasi-static tensile response also revealed strain softening, while strain re-hardening was not observed since the test specimens fractured prior to reaching this region. However, in the strain range of 0-10%, the general trend of the all the stress-strain curves (tension and compression) are similar at different strain rates (Figure 6.2). The similar trend of the stress-strain response is an important assumption for many elastic-plastic constitutive models because these models use a linear logarithmic relation to scale up the plastic stress-strain curve at the lowest strain rate to incorporate the strain rate effect, including the constitutive model used in the current study.

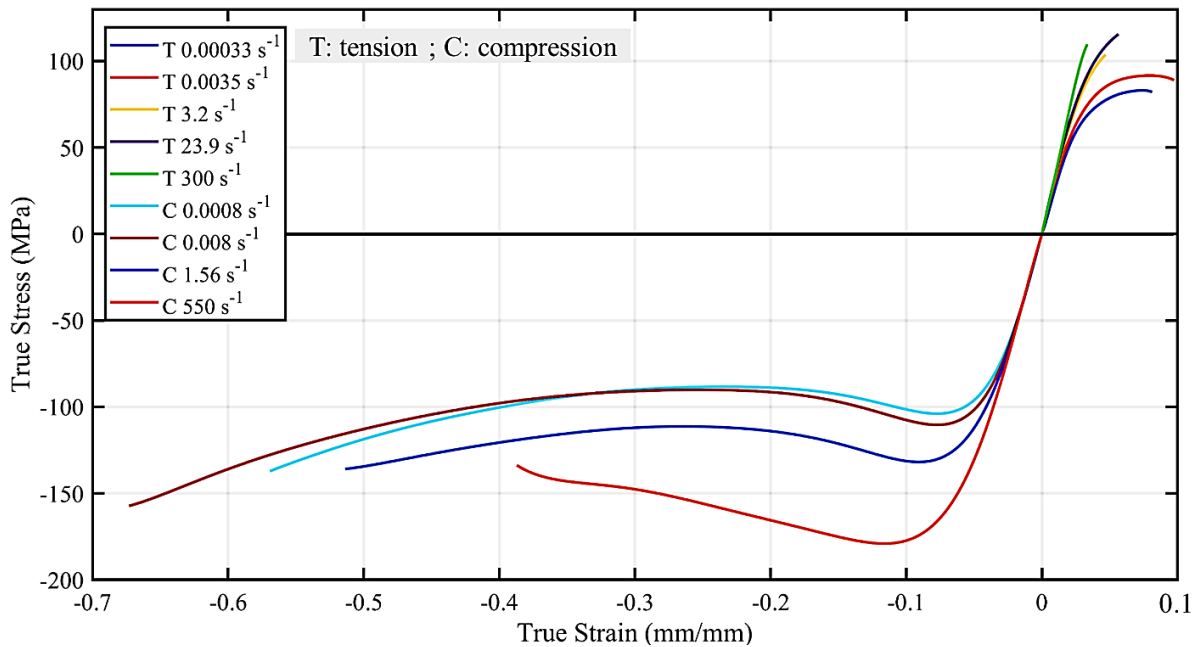


Figure 6.1. Average true stress-strain plots for all the compressive and tensile tests at different strain rates.

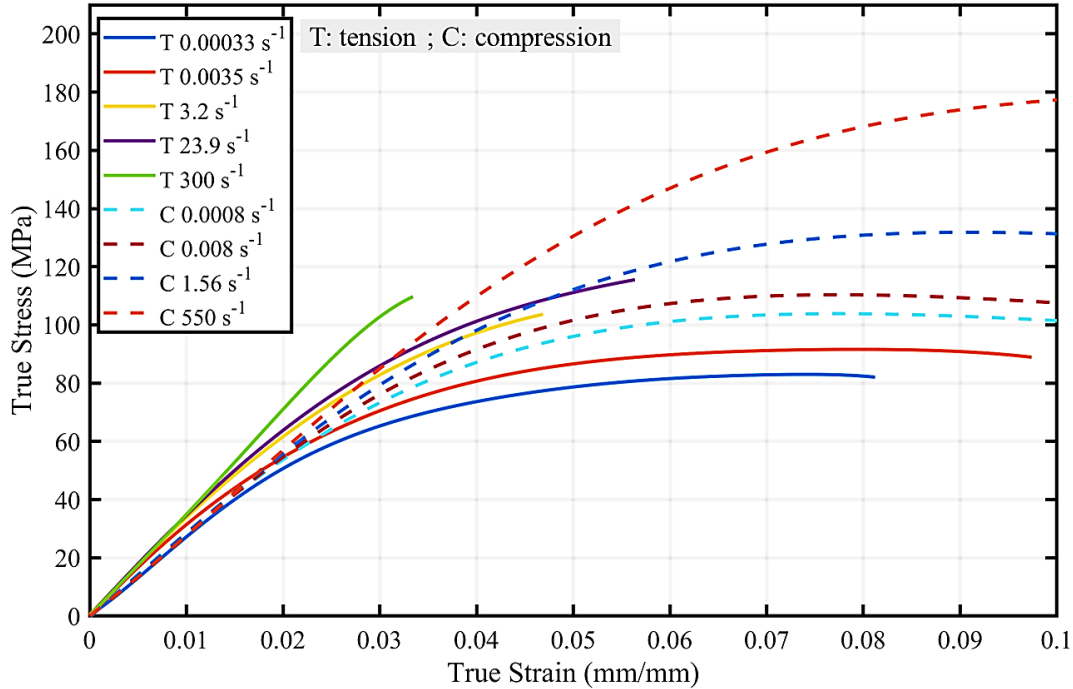


Figure 6.2. Representative true stress-strain plots of all the compression and tensile tests at different strain rates (up to 10% strain).

Second, the epoxy exhibited asymmetric yielding between tension and compression. The compressive yield strengths were noticeably higher than the tensile yield strengths at similar strain rates. As shown in Figure 6.2, for the quasi-static tests, the compressive yield strength is about 30% higher than the tensile value at similar strain rates (0.00033 s^{-1} for tension versus 0.0008 s^{-1} for compression). The difference of yield strengths between tension and compression indicates the presence of pressure dependence in this epoxy material, where higher hydrostatic pressures in compression lead to higher yield strength (see detail in Section 2.1.6).

Third, the tensile elastic modulus was more sensitive to the change of strain rates than the compressive elastic modulus, which is in agreement with several previous studies [36, 51, 54]. The linear elastic regions of the compressive stress-strain curves are almost overlapping, which indicates a small variation of the elastic modulus with strain rates (Figure 6.2). The linear elastic regions of the tensile stress-strain curves reveal that there was notable strain rate dependency on the tensile elastic modulus, with an increase in elastic modulus of 34% at the highest strain rate considered relative to lowest the quasi-static strain rate. As discussed in Section 2.1.6, during linear elastic deformation the response of the epoxy material includes a nonlinear viscoelastic component due to minor intermolecular interaction and movement in the side groups. The viscoelastic component of deformation can be significantly influenced by the strain rate, as

was the case for tension. The strain rate dependent elastic modulus was an important characteristic to consider when identifying the constitutive model for the epoxy material. Most elastic-plastic constitutive models assume a constant elastic modulus.

The mechanical characterization results revealed the strain rate sensitivity and the hydrostatic pressure dependence of the deformation response of the studied epoxy material. However, there are three points that should be noted. First, some of the tension test specimens fractured at lower than expected strains, especially the specimens of the lower intermediate strain rate test. Ideally, a lower fracture strain should be associated with a higher strain rate. However, in the real test, the fracture strain was heavily affected by many factors, including epoxy processing defects, test specimen machining defects, test equipment and test setup. In this research, the tensile intermediate strain-rate test machine might be the main reason for the cause of lower fracture strain. As mentioned in Section 4.2.2, the test equipment was a common challenge for the mechanical characterization of glassy polymers at the intermediate strain rates. Second, compression tests were not performed at high intermediate strain rates (i.e., strain rates between 10 and 100 s⁻¹) due to the limitation of the testing frames used. Intermediate strain-rate test data was particularly important because there was not enough information for epoxy material in this strain rate region in the literature. Normally, a specially designed test machine was required to conduct tests at the intermediate strain rate region. Third, for the shear tests, the specimen geometry used in this study was not suitable for the higher strain rate tests (i.e., strain rates > 1 s⁻¹) because the specimens fractured prematurely due to the tensile stress. Thus, only the quasi-static shear test data was completed in this study.

Some factors might influence the mechanical characterization results in the current study. First, the sample materials for the current study were fabricated using two different methods, and these two types of material samples might have slightly different mechanical responses. Second, the machining defects on the edge of the specimen could affect the test results, particularly the failure strain of the tensile specimen and the validation test results. The strength of the material should not be affected by the machining defect because the quasi-static tensile test data agreed with the corresponding data provided by the resin supplier. Third, the different specimen geometries used at different strain rates might introduce some variation for the tension and compression tests. However, it was difficult to eliminate this difference because of the different test requirements for the different strain rate tests considered.

The mechanical properties of the studied snap-cure epoxy were compared to that of a conventional epoxy to assess the relative performance. The selected epoxy material was RTM6 (Hexcel Corporation), which is

a standard-cure epoxy that is widely used to fabricate FRP composite with an RTM processes. RTM6 epoxy has a similar highly cross-linked molecular structure with that of the studied snap-cure epoxy, with a curing cycle of approximately 10 hours. Two different studies focused on the mechanical characterization of the RTM6 epoxy material have been reported [40, 51]. The true compressive failure strains of RTM6 were approximately 68% at 0.0001 s^{-1} strain rate (calculated based on the crosshead displacements) [40] and approximately 39% at 0.01 s^{-1} strain rate (measured by a laser extensometer) [51]. Recall that for the snap-cure epoxy the compressive failure strains were approximately 57% and 67% at 0.0008 and 0.008 s^{-1} strain rates, respectively. The reported compressive yield strength of RTM6 was approximately 125 MPa at 0.0001 s^{-1} strain rate [40] and approximately 140 MPa at 0.01 s^{-1} strain rate [51], whereas values for the snap-cure epoxy were 104 MPa and 110 MPa at 0.0008 and 0.008 s^{-1} strain rates, respectively. At similar quasi-static strain rates, the compressive yield strength of RTM6 was higher than the snap-cure epoxy, but the average failure strain of RTM6 was lower than the snap-cure epoxy. Therefore, the overall mechanical performance of the studied snap-cure epoxy material was similar when compared with a highly cross-linked standard-cure epoxy material.

6.2 Constitutive Modeling

As discussed in Section 2.3.1, the metal elastic-plastic constitutive model used in this study divides the deformation into two components: linear elastic and Johnson-Cook plastic. For the linear elastic part, the stresses are linearly proportional to the strain, and there is no strain rate dependence in this region. As the stresses reached the assumed yield strength (Johnson-Cook material parameter A or 19.2MPa from the model calibration), the plastic stress-strain relation described by the Johnson-Cook hardening was added to the linear relation to determine the progress of strain rate dependent plastic deformation. In Abaqus, the Johnson-Cook hardening works with the Von Mises yield criterion, which means the yield function is only dependent on the deviatoric stress or shear stress, without considering the hydrostatic stress.

The true stress-strain curves for the tensile experiments and single element tests at different strain rates are plotted to investigate the prediction capability of the built-in metal elastic-plastic constitutive model in Abaqus for the deformation of the studied epoxy material (Figure 6.3). Overall, the elastic-plastic constitutive model was able to describe the deformation and the strain rate dependent behaviours of the studied epoxy material under tensile loading conditions. The validation test results in Section 5.6 revealed that the studied elastic-plastic constitutive model was able to estimate more complex stress conditions. For the simulations that focus on the compressive loading conditions, the material parameters for the current

constitutive model may need to be recalibrated using the compression test data due to the different yield behaviours in tension and compression. The isotropic Von Mises yield criterion used in the studied elastic-plastic constitutive model was not able to capture asymmetric yielding.

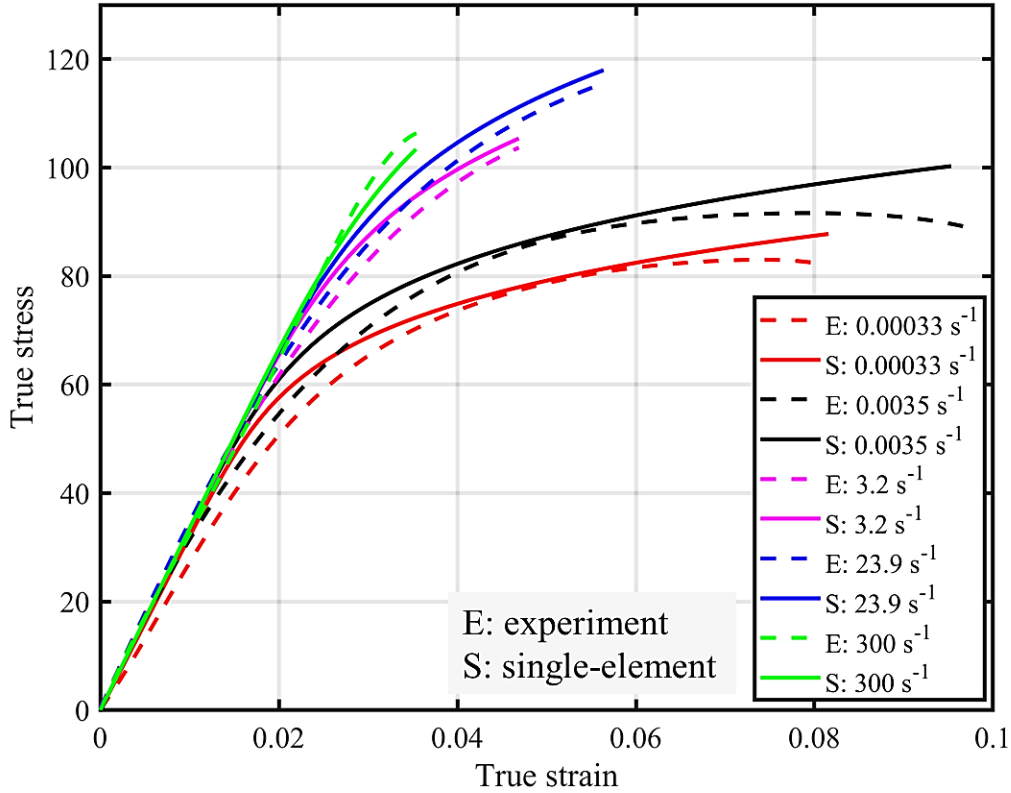


Figure 6.3. Representative true stress-strain plots for all the tensile experiments and single element tests at different strain rates.

There are several limitations in using the available elastic-plastic constitutive model to predict the deformation of studied epoxy material. First, the elastic modulus was considered as a constant for both tensile and compressive stress conditions in the constitutive model (typical for elastic-plastic constitutive models). For the compression conditions, this assumption might be valid. However, the tension test results indicated that the elastic modulus of the epoxy material exhibits a clear strain-rate dependence during tensile loading conditions (Figure 6.2). Thus, the studied material model could induce deviations in the elastic deformation region for tensile stress conditions. Second, the elastic-plastic constitutive model adopts the isotropic Von Mises yield criterion, which assumes yield strengths to be the same in tension and compression, but this assumption does not hold for the studied epoxy material. As discussed in Section 6.1, the compressive yield strengths were significantly higher than the tensile yield strengths for the same strain rate, and the hydrostatic pressure played an important role in the yield behaviours of the studied epoxy

material. Thus, the current material parameters that were calibrated based on the tensile test data might not be suitable to simulate compression driven yielding deformation. Third, the Johnson-Cook plasticity cannot describe the large deformation (strain softening and strain re-hardening) behaviours of the epoxy materials.

Despite the limitations in predicting large material deformation, the presented constitutive model may be suitable for the investigated epoxy material when constrained by high-stiffness reinforcing fibers in an FRP composite material. Using a unidirectional (UD) fiber-reinforced/epoxy composite material as an example, there are five basic loading modes that should be considered: longitudinal tensile, transverse tensile, longitudinal compressive, transverse compressive, and in-plane shear (Figure 6.4). For the longitudinal tensile loading mode the failure strain of the UD composite is governed by the fibers and is typically $<2.5\%$, while for the transverse tensile loading mode failure of the UD composite is governed by the fiber/matrix interface with failure strains typically $<1\%$ [122]. It should be noted that local strains in the matrix may exceed the failure strains of the UD composite. Nevertheless, the studied constitutive model can accurately predict the deformation of the epoxy within these strain ranges. For the longitudinal compressive loading, fiber micro-buckling (i.e., kink band formation) is typically observed, where local (constrained) shear deformation of the epoxy matrix causes local instability of the fibers and brittle failure of the epoxy. Transverse compressive failure normally initiates at the fiber/matrix interfaces, and is driven by local shear stresses [123]. Finally, in-plane shear deformation is also governed by local shear deformation of the constrained epoxy matrix.

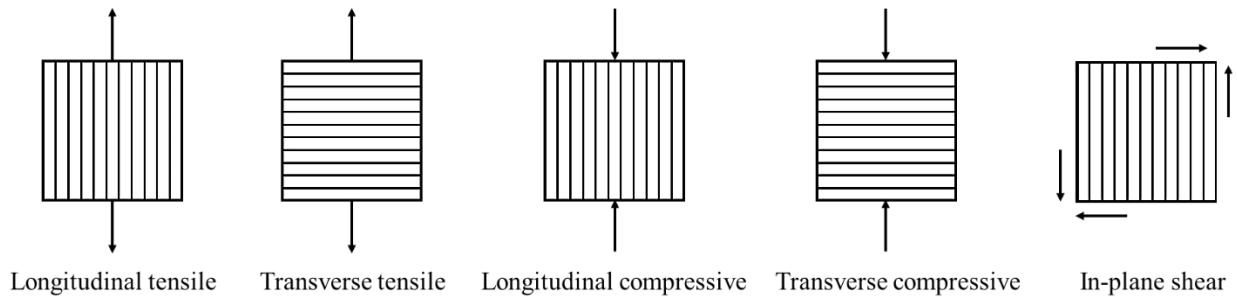


Figure 6.4. Five basic loading modes for UD composites

Chapter 7 Conclusions and Future Work

7.1 Conclusions

The overarching goal of this study was to support the development of a robust high-fidelity virtual micromechanical tool to be used within a multiscale modeling framework for predicting the performance of CFRP materials and energy-absorbing structures. The main research objectives comprised of characterizing the mechanical response and identifying a suitable strain rate dependent constitutive model for a snap-cure epoxy material. A series of uniaxial mechanical tests were conducted to characterize the strain rate dependent tensile, compressive, and shear stress-strain behaviour of the epoxy material under a variety of strain rates, ranging from quasi-static to dynamic strain rates, which was the major component of this study. Based on the mechanical characterization results, the existing elastic-plastic constitutive model in a commercial finite element solver was identified and calibrated to verify suitability for the studied epoxy material.

The major findings for the mechanical characterization of the studied snap-cure epoxy are summarized as follows:

- 1) The studied snap-cure epoxy exhibited a large deformation for compressive quasi-static strain rates, where the stress-strain response can be divided into different stages: elastic, plastic yield, strain softening, and strain re-hardening. These four deformation stages agree with other high cross-linked epoxies and many glassy thermoplastics at a temperature well below their T_g . The tensile and high strain rate compressive stress-strain behaviours showed different post-yield responses because of the different failure strains.
- 2) The tensile elastic modulus increased by 34% over the range of strain rates investigated, demonstrated a strong strain rate dependence, while the compressive elastic modulus showed little difference over the tested strain rates.
- 3) The tensile and compressive post-yield responses showed noticeable strain rate dependence, where yield strength increased by 31% and 81% over the range of strain rates investigated, respectively.
- 4) Pressure-dependent plastic deformation was identified by a difference in compression and tension yield strength. The compressive yield strength was 46% higher than the tensile yield strength at the similar quasi-static strain rates, attributed to the higher hydrostatic pressure in compression.
- 5) Brittle fracture of all the tensile specimens was confirmed by the assessment of the fracture surfaces, where all the tensile specimens demonstrated similar fracture patterns at the tested strain rates.

A Johnson-Cook plasticity model was identified as a suitable model to represent the studied epoxy in a computational model and implemented in a commercial finite element software (Abaqus). Based on the single element verification simulations performed, the chosen constitutive model was able to accurately describe the deformation response and the strain rate dependence of the studied epoxy material under tensile loading conditions, as well as the shear deformation at quasi-static strain rates. The validation of the material constitutive model with independent experiments revealed that the Johnson-Cook constitutive model was able to describe the overall strain response of the validation tests and to identify high strain gradients within the tested specimens with non-uniform multiaxial stress states. The limitations of the constitutive model include an inability to capture the strain rate-dependent tensile elastic modulus and the pressure-dependent yield behaviour of the studied epoxy material.

7.2 Future work

Although the current study was able to reveal and represent many critical characteristics of the snap-cure epoxy material, additional research is needed to further assess the mechanical responses of the material in complex loading scenarios and to address the limitations of the current classical metal elastic-plastic constitutive model. First, the fabrication of the epoxy panels by HP-RTM should be improved to reduce the observed defects, and the machining defects of the test specimens can be minimized by using a direct-cast process. Second, strain-rate dependent shear responses of the epoxy can be investigated over a range of strain rates. Potential viscoplastic material models for epoxy materials might require these shear responses for calibration (e.g., Goldberg's model). Third, the pressure dependence of the epoxy that causes different yielding behaviors in tension and compression can be characterized by triaxial tests. By incorporating the current data sets with triaxial test results, some elastic-plastic constitutive material models can be calibrated to predict the pressure-dependent yield behavior of the epoxy (e.g., Drucker-Prager plasticity). Finally, based on the literature, the mechanical responses of the epoxy may demonstrate a temperature dependence, which can be investigated in further study. Overall, the classical metal elastic-plastic constitutive model in the current research was an initial investigation of the material models for the snap-cure epoxy. A high-fidelity thermo-viscoelastic-viscoplastic constitutive material model that might provide improved predictions can be investigated in future studies of the snap-cure epoxy.

Bibliography

- [1] The International Council on Clean Transportation (ICCT), "Global PV figure data 20200527," 27 May 2020. [Online]. Available: <https://theicct.org/file/global-pv-figure-data-20200527xlsx-0>. [Accessed 4 June 2020].
- [2] K. Shanmugam, V. Gadhamshetty, P. Yadav, D. Athanassiadis, M. Tysklind and V. K. Upadhyayula, "Advanced High-Strength Steel and Carbon Fiber Reinforced Polymer Composite Body in White for Passenger Cars: Environmental Performance and Sustainable Return on Investment under Different Propulsion Modes," *ACS sustainable chemistry & engineering*, vol. 7, no. 5, pp. 4951-4963, 2019.
- [3] W. Joost, "Reducing Vehicle Weight and Improving U.S. Energy Efficiency Using Integrated Computational Materials Engineering," *the Journal of the Minerals*, vol. 64, no. 9, p. 1032–1038, 2012.
- [4] A. Elmarakbi, "Overview of Composite Materials and their Automotive Applications," in *Advanced composite materials for automotive applications : structural integrity and crashworthiness*, Chichester, John Wiley & Sons, 2014, pp. 3-28.
- [5] A. Brighton, M. Forrest, M. Starbuck, D. Erdman and B. Fox, "Strain Rate Effects on the Energy Absorption of Rapidly Manufactured Composite Tubes," *Journal of Composite Materials*, vol. 43, no. 20, p. 2183–2200, 2009.
- [6] G. GARDINER, "CompositesWorld," 7 October 2016. [Online]. Available: <https://www.compositesworld.com/articles/is-the-bmw-7-series-the-future-of-autocomposites>. [Accessed 20 June 2020].
- [7] O. Faruk, J. Tjong and M. Sain, *Lightweight and Sustainable Materials for Automotive Applications*, Boca Raton: CRC Press, 2017.
- [8] A. Cherniaeva, Y. Zeng, D. Cronin and J. Montesano, "Quasi-static and dynamic characterization of unidirectional non-crimp carbon fiber fabric composites processed by HP-RTM," *Polymer Testing*, pp. 365 - 375, 2019.

- [9] D. H.-J. Lukaszewicz, "Automotive Composite Structures for Crashworthiness," in *Advanced composite materials for automotive applications : structural integrity and crashworthiness*, Chichester, John Wiley & Sons, 2014, pp. 99-127.
- [10] X. Morelle, "Mechanical characterization and physics-based modeling of highly-crosslinked epoxy resin (Ph.D. dissertation)," Université catholique de Louvain, Louvain-la-Neuve, 2015.
- [11] J. LLorca, C. González, J. M. Molina-Aldareguía, J. Segurado, R. Seltzer, F. Sket, M. Rodríguez, S. Sádaba, R. Muñoz and L. P. Canal, "Multiscale Modeling of Composite Materials: a Roadmap Towards Virtual Testing," *Advanced Materials*, vol. 23, no. 44, p. 5130–5147, 2011.
- [12] S. Ghosh, "Adaptive Concurrent Multilevel Model for Multiscale Analysis of Composite Materials Including Damage," in *Multiscale Modeling and Simulation of Composite Materials and Structures*, New York, Springer, 2008, pp. 83-163.
- [13] Z. Xia and W. Curtin, "Multiscale Modeling of Tensile Failure in Fiber-Reinforced Composites," in *Multiscale Modeling and Simulation of Composite Materials and Structures*, New York, Springer, 2008, pp. 37-82.
- [14] H. Lee, *Handbook Of Epoxy Resins*, New York: Mcgraw-Hill, 1967.
- [15] S. Yamini and R. J. Young, "The mechanical properties of epoxy resins," *Journal of Materials Science*, pp. 1823-1831, 1980.
- [16] C. A. May and Y. Tanaka, *Epoxy Resins: Chemistry and Technology*, New York: Marcel Dekker, Inc., 1973.
- [17] P. F. Bruins, *Epoxy Resin Technology*, New York: Wiley-Inter-science, 1968.
- [18] J. H. Hodgkin, G. P. Simon and R. J. Varley, "Thermoplastic toughening of epoxy resins: a critical review," *Polymers advanced technologies*, vol. 9, no. 1, pp. 3-10, 1998.
- [19] W. G. Potter, *Epoxide Resins*, London: Iliffe Books, 1970.
- [20] M. A. Boyle, C. J. Martin and J. D. Neuner, "Epoxy Resin," in *ASM Handbook*, ASM International, 2001, pp. 78-89.

- [21] P. C. Alfred Rudin, *The Elements of Polymer Science And Engineering*, Academic Press, 2013.
- [22] M. Chanda, *Introduction to Polymer Science and Chemistry: A Problem-Solving Approach*, Second Edition, Boca Raton: CRC Press, 2013.
- [23] B. ELLIS, *Chemistry and Technology*, Dordrecht : Springer, 1993.
- [24] I. Varma and V. Gupta, "Thermosetting Resin—Properties," in *Comprehensive Composite Materials*, Elsevier Ltd., 2000, pp. 1-56.
- [25] A. D. M. S. £. S. J. Stabik, "Viscosity measurements of epoxy resin filled with ferrite powders," *Archives of Materials Science and Engineering*, vol. 38, no. 1, pp. 34-40, 2009.
- [26] S. C. Lin and E. M. Pearce, *High-performance thermosets. Chemistry, properties and applications.*, Munich, Vienna, New York: Carl Hanser Verlag, 1993.
- [27] J. Robins and C. D. Wright, "FAST CURING EPOXY RESIN COMPOSITIONS". United States Patent 4,668,736, 26 May 1987.
- [28] L. S. Penn and T. T. Chiao, "EPOXY RESINS," in *Handbook of Composites*, Boston, Springer, 1982, pp. 57-88.
- [29] A. B. Strong, *Fundamentals of Composites Manufacturing: Materials, Methods, and Applications*, Dearborn: Society of Manufacturing Engineers, 2007.
- [30] B. Ellis, M. S. Found and J. R. Bell, "Effects of cure treatment on glass transition temperatures for a BADGE–DDM epoxy resin," *Journal of Applied Polymer Science*, vol. 59, no. 10, pp. 1493-1505, 1996.
- [31] S. Black, "Automotive composites: Thermosets for the fast zone," *Composites Woild*, 30 5 2020.
- [32] T. A. Morley, R. Koeniger, M. Reimers, P. Cate, N. Jelic and Z. Sikman, "Novel Epoxy Resin System for Making Carbon Fiber Composites". International Patent WO2016/209864A1, 29 12 2016.

- [33] HEXION, "Epoxy Systems for Automotive Structural Components," HEXION, 2019. [Online]. Available: <https://www.hexion.com/en-GB/applications/composites/automotive/structural/>. [Accessed 07 08 2020].
- [34] HUNTSMAN, "Araldite® composite solutions provide fast curing where high productivity is required," HUNTSMAN, 2020. [Online]. Available: <https://www.huntsman-transportation.com/automotive-composites/body-in-white.html>. [Accessed 07 08 2020].
- [35] DOW, "VORAFORCE™ Ultra-fast Cure Composite Epoxy Systems Overview," DOW, [Online]. Available: <https://www.dow.com/en-us/document-viewer.html?randomVar=7779359788288566453&docPath=/content/dam/dcc/documents/en-us/mark-prod-info/299/299-52386-01-voraforce-ultrafast-cure-composite-epoxy-systems-overview.pdf>. [Accessed 07 08 2020].
- [36] S. Tamrakar, R. Ganesh, S. Sockalingam, B. Z. Haque and J. W. G. Jr., "Experimental Investigation of Strain Rate and Temperature Dependent Response of an Epoxy Resin Undergoing Large Deformation," *Journal of Dynamic Behavior of Materials*, no. 4, pp. 114-128, 2018.
- [37] O. Sindt, J. Perez and J. F. Gerard, "Molecular architecture-mechanical behaviour relationships in epoxy networks," *Polyme*, vol. 37, no. 14, pp. 2989-2997,, 1996.
- [38] A. C. Grillet, J. Galy, J.-F. Gérard and J.-P. Pascault, "Mechanical and viscoelastic properties of epoxy networks cured with aromatic diamines," *Polymer*, vol. 32, no. 10, pp. 1885-1891, 1991.
- [39] E. Urbaczewski-Espuche, J. Galy, J. Gerard, J. Pascault and H. Sautereau, "Influence of chain flexibility and crosslink density on mechanical properties of epoxy/amine networks," *Polymer Engineering and Science*, vol. 31, no. 22, pp. 1572-1580, 1991.
- [40] X. P. Morelle, J. Chevalier, C. Bailly, T. Pardoën and F. Lani, "Mechanical characterization and modeling of the deformation and failure of the highly crosslinked RTM6 epoxy resin," *Mechanics of Time-Dependent Materials*, vol. 3, no. 21, pp. 419-454, 2017.
- [41] R. K. Goldberg, G. D. Roberts and A. Gilat, "Incorporation of mean stress effects into the micromechanical analysis of the high strain rate response of polymer matrix composites," *Composites: Part B*, no. 34, p. 151–165, 2003.

- [42] W. Chen, F. Lu and M. Cheng, "Tension and compression tests of two polymers under quasistatic and dynamic loading," *Polymer Testing*, no. 22, pp. 113 - 121, 2002.
- [43] O. A. HASAN and M. C. BOYCE, "A Constitutive Model for the Nonlinear Viscoelastic Viscoplastic Behavior of Glassy Polymers," *POLYMER ENGINEERING AND SCIENCE*, vol. 35, no. 4, p. 331–344, 1995.
- [44] R. N. Haward and G. Thackray, "The Use of a Mathematical Model to Describe Isothermal Stress-Strain Curves in Glassy Thermoplastics," *Proceedings of the Royal Society of London. Series A, Mathematical and Physical Sciences*, vol. 302, no. 1471, pp. 453-472, 1968.
- [45] L. E. G. Han E.H. Meijer, "Mechanical performance of polymer systems: The relation between structure and properties," *Progress in Polymer Science*, no. 30, pp. 915-938, 2005.
- [46] M. Alger, *Polymer Science Dictionary*, London: Springer, 1996.
- [47] R. Brown, *Handbook of Polymer Testing: Physical Methods*, New York: CRC Press, 1999.
- [48] A. S. Argon, "A theory for the low-temperature plastic deformation of glassy polymers," *The Philosophical Magazine: A Journal of Theoretical Experimental and Applied Physics*, vol. 28, no. 4, pp. 839-865, 1973.
- [49] C. Buckley, J. Harding, J. Hou, C. Ruiz and A. Trojanowski, "Deformation of thermosetting resins at impact rates of strain. Part I: Experimental study," *Journal of the Mechanics and Physics of Solids*, no. 49, p. 1517 – 1538, 2001.
- [50] S. Behzadi and F. R. Jones, "Yielding Behavior of Model Epoxy Matrices for Fiber Reinforced Composites: Effect of Strain Rate and Temperature," *Journal of Macromolecular Science, Part B, Physics*, vol. 44, no. 6, p. 993–1005, 2005.
- [51] R. Gerlach, C. R. Siviour, N. Petrinic and J. Wiegand, "Experimental characterisation and constitutive modelling of RTM-6 resin under impact loading," *Polymer*, vol. 49, no. 11, pp. 2728 - 2737, 2008.
- [52] J. D. Littell, C. R. Ruggeri, R. K. Goldberg, G. D. Roberts, W. A. Arnold and W. K. Binienda, "Measurement of Epoxy Resin Tension, Compression, and Shear Stress–Strain Curves over a Wide

- Range of Strain Rates Using Small Test Specimens," *Journal of Aerospace Engineering*, vol. 21, no. 3, pp. 162 -173, 2008.
- [53] J. L. Jordan, J. R. Foley and C. R. Siviour, "Mechanical properties of Epon 826/DEA epoxy," *Mechanics of Time-Dependent Materials*, no. 12, pp. 249-272, 2008.
- [54] B. Werner and I. Daniel, "Characterization and modeling of polymeric matrix under multi-axial static and dynamic loading," *Composites Science and Technology*, no. 102, pp. 113-119, 2014.
- [55] X. Poulain and R. G. A.A. Benzerga, "Finite-strain elasto-viscoplastic behavior of an epoxy resin: Experiments and modeling in the glassy regime," *International Journal of Plasticity*, no. 62, pp. 138 -161, 2014.
- [56] L. Struik, "Some problems in the non-linear viscoelasticity of amorphous glassy polymers," *Journal of Non-Crystalline Solids*, Vols. 131-133, pp. 395-407, 1991.
- [57] Jatin, V. Sudarkodi and S. Basu, "Investigations into the origins of plastic flow and strain hardening in amorphous glassy polymers," *International Journal of Plasticity*, no. 56, pp. 139 - 155, 2014.
- [58] E. M. Arruda and M. C. Boyce, "Evolution of plastic anisotropy in amorphous polymers during finite straining," *International Journal of Plasticity*, vol. 9, no. 6, pp. 697-720, 1993.
- [59] E. T. J. Klompen, T. A. P. Engels, L. E. Govaert and H. E. H. Meijer, "Modeling of the Postyield Response of Glassy Polymers: Influence of Thermomechanical History," *Macromolecules*, vol. 38, no. 16, pp. 6997-7008, 2005.
- [60] H. Melick, L.E.Govaert and H.E.H.Meijer, "On the origin of strain hardening in glassy polymers," *Polymer*, vol. 44, no. 8, pp. 2493-2502, 2003.
- [61] D. J. A. Senden, J. A. W. v. Dommelen and L. E. Govaert, "Strain hardening and its relation to bauschinger effects in," *Journal of Polymer Science Part B: Polymer Physics*, vol. 48, no. 13, p. 1483–1494, 2010.
- [62] H. RN and T. G., "Use of a mathematical model to describe isothermal stress-strain curves in glassy thermoplastics," *Proceedings of the Royal Society of London. Series A*, vol. 302, no. 1471, pp. 453-472, 1968.

- [63] C. R. Siviour and J. L. Jordan, "High Strain Rate Mechanics of Polymers: A Review," *Journal of Dynamic Behavior of Materials*, vol. 2, pp. 15-32, 2016.
- [64] M. C. Boyce, D. M. Parks and A. S. Argon, "Large inelastic deformation of glassy polymers. part I: rate dependent constitutive model.," *Mechanics of Materials*, vol. 7, no. 1, pp. 15-33, 1988.
- [65] A. S. ARGON, *The Physics of Deformation and Fracture of Polymers*, New York: Cambridge University Press, 2013.
- [66] K. D. Pae and S. K. Bhateja, "The effects of hydrostatic pressure on the mechanical behavior of polymers.," *Journal of Macromolecular Science*, vol. 13, no. 1, p. 1-75, 1975.
- [67] E. J. PARRY and D. TABOR, "Pressure dependence of the shear modulus of various polymers," *Journal of Materials Science*, vol. 9, pp. 289 - 292, 1974.
- [68] H. Kolsky, "An investigation of the mechanical properties of materials at very high rates of loading," *Proceedings of*, no. 62, p. 676-700, 1949.
- [69] S. Walley, J. Field, P. Pope and N. Safford, "A study of the rapid deformation behaviour of a range of polymers," *Philosophical Transactions of the Royal Society of London*, vol. 328, p. 1-33, 1989.
- [70] S. Chou, K. Robertson and J. Rainey, "The effect of strain rate and heat developed during deformation on the stress-strain curve of plastics," *Experimental Mechanics*, vol. 13, p. 422-432, 1973.
- [71] A. Gilat, R. K. Goldberg and G. D. Roberts, "Strain Rate Sensitivity of Epoxy Resin in Tensile and Shear Loading," *JOURNAL OF AEROSPACE ENGINEERING*, vol. 20, no. 2, pp. 75-89, 2007.
- [72] H. Kuhn and D. Medlin, *ASM Handbook, Volume 8 : Mechanical Testing and Evaluation*, ASM International, 2000.
- [73] B. Song, C. J. Syn, C. L. Grupido, W. Chen and W. Lu, "A Long Split Hopkinson Pressure Bar (LSHPB) for Intermediate-rate Characterization of Soft Materials," *Experimental Mechanics*, vol. 48, no. 6, p. 809-815, 2008.
- [74] G. T. (. Gray III, "Classic Split-Hopkinson Pressure Bar Testing," in *ASM Handbook Volume 8: Mechanical Testing and Evaluation*, ASM International, 2000, p. p462-476.

- [75] P. Follansbee, "The Hopkinson Bar, Mechanical Testing," in *ASM Handbook*, American Society for Metals, 1985, p. 198–203.
- [76] C. Salisbury, "*Spectral analysis of wave propagation through a polymeric Hopkinson Bar*" M.S. thesis, Waterloo, Ontario, Canada: Department of Mechanical and Mechatronics Engineering, University of Waterloo, 2001.
- [77] Q. Liu and G. Subhash, "Characterization of viscoelastic properties of polymer bar using iterative deconvolution in the time domain," *Mechanics of Materials*, vol. 38, pp. 1105-1117, 2006.
- [78] C. V. Sligtenhorst, D. S. Cronin and G. Brodland, "High strain rate compressive properties of bovine muscle tissue determined using a split Hopkinson bar apparatus," *Journal of Biomechanics*, vol. 39, no. 10, pp. 1852-1858, 2006.
- [79] C. P. Salisbury and D. S. Cronin, "Mechanical Properties of Ballistic Gelatin at High Deformation Rates," *Experimental Mechanics*, vol. 49, p. 829–840, 2009.
- [80] C. Salisbury and D. Cronin, "Deformation Mechanics of a Non-linear Hyper-viscoelastic Porous Material, Part I: Testing and Constitutive Modeling of Non-porous Polychloroprene," *Journal of Dynamic Behavior of Materials*, vol. 1, p. 237–248, 2015.
- [81] A. Benatar, D. Rittel and A. Yarin, "Theoretical and experimental analysis of longitudinal wave propagation in cylindrical viscoelastic rods.," *Journal of the Mechanics and Physics of Solids*, vol. 51, p. 1413–1431, 2003.
- [82] D. A. Gorham, "A numerical method for the correction of dispersion in pressure bar signals," *Journal of Physics E: Scientific Instruments*, vol. 16, no. 6, p. 477–479, 2000.
- [83] C. Bacon, "An experimental method for considering dispersion and attenuation in a viscoelastic Hopkinson bar," *Experimental Mechanics*, vol. 38, p. 242–249, 1998.
- [84] R. J. Wasley, K. G. Hoge and J. C. Cast, "Combined Strain Gauge—Quartz Crystal Instrumented Hopkinson Split Bar," *Review of Scientific Instruments*, vol. 40, no. 7, pp. 889-894, 1969.
- [85] W. Chen, F. Lu and B. Zhou, "A quartz-crystal-embedded split Hopkinson pressure bar for soft materials," *Experimental Mechanics*, vol. 40, pp. 1-6, 2000.

- [86] W. Chen, B. Zhang and M. J. Forrester, "A split Hopkinson bar technique for low-impedance materials," *Experimental Mechanics*, vol. 39, pp. 81- 85, 1999.
- [87] D. J. Frew, M. J. Forrester and W. Chen, "Pulse shaping techniques for testing brittle materials with a split hopkinson pressure bar," *Experimental Mechanics*, vol. 42, p. 93–106, 2002.
- [88] D. J. Frew, M. J. Forrester and W. Chen, "Pulse shaping techniques for testing elastic-plastic materials with a split Hopkinson pressure bar," *Experimental Mechanics*, vol. 45, no. 2, pp. 186 - 195, 2005.
- [89] H.Zhao, G.Gary and J.R.Klepaczko, "On the use of a viscoelastic split hopkinson pressure bar," *International Journal of Impact Engineering*, vol. 19, no. 4, pp. 319-330, 1997.
- [90] B.J.Briscoe and R.W.Nosker, "The influence of interfacial friction on the deformation of high density polyethylene in a split hopkinson pressure bar," *Wear*, vol. 95, no. 3, pp. 241-262, 1984.
- [91] A.Trautmann, C.R.Siviour, S.M.Walley and J.E.Field, "Lubrication of polycarbonate at cryogenic temperatures in the split Hopkinson pressure bar," *International Journal of Impact Engineering*, vol. 31, no. 5, pp. 523-544, 2005.
- [92] J. S. Bergstrom, *Mechanics of Solid Polymers: Theory and Computational Modeling*, Norwich: William Andrew, 2015.
- [93] E. M. A. a. M. C. Boyce, "three-dimensional constitutive model for the large stretch behavior of rubber elastic materials.," *Journal of the Mechanics and Physics of Solids*, vol. 41, no. 2, p. 389–412, 1993.
- [94] E. V. D. G. P.D.Wu, "On improved network models for rubber elasticity and their applications to orientation hardening in glassy polymers," *Journal of the Mechanics and Physics of Solids*, vol. 41, no. 3, p. 427–456, 1993.
- [95] T. A. Tervoort, E. T. J. Klompen and L. E. Govaert, "A multi-mode approach to finite, three-dimensional, nonlinear viscoelastic behavior of polymer glasses," *Journal of Rheology*, vol. 40, no. 5, pp. 779-797, 1996.

- [96] R. K. Goldberg, "Implementation of Fiber Substructuring Into Strain Rate Dependent Micromechanics Analysis of Polymer Matrix Composites," National Aeronautics and Space Administration, Washington, D.C., 2001.
- [97] S. R. Bodner and Y. Partom, "Constitutive Equations for Elastic-Viscoplastic Strain-Hardening Materials," *J. Appl. Mech.*, vol. 42, no. 2, pp. 385-389, 1975.
- [98] Abaqus, "Abaqus 6.13 Online Documentation," 2 April 2013. [Online]. Available: <http://dsk.ippt.pan.pl/docs/abaqus/v6.13/books/usb/default.htm>. [Accessed 20 February 2020].
- [99] K. Hashiguchi, *Elastoplasticity Theory*, Heidelberg: Springer, 2014.
- [100] D. C. DRUCKER and W. PRAGER, "SOIL MECHANICS AND PLASTIC ANALYSIS OR LIMIT DESIGN," *Quarterly of applied mathematics*, vol. 10, no. 2, p. 157–165, 1952.
- [101] J. Lubliner, *Plasticity Theory*, Mineola: Dover Publications, 2013.
- [102] I. M. Smith, D. V. Griffiths and L. Margetts, *Programming the Finite Element Method*, Chichester: John Wiley & Sons, 2013.
- [103] L. Kachanov, *Fundamentals of the Theory of Plasticity*, Amsterdam: Dover Publications Inc., 2004.
- [104] C. Gonzalez and J. LLorca, "Mechanical behavior of unidirectional fiber-reinforced polymers under transverse compression: Microscopic mechanisms and modeling," *Composites Science and Technology*, vol. 67, p. 2795–2806, 2007.
- [105] L. P. Canal, J. Segurado and J. LLorca, "Failure surface of epoxy-modified fiber-reinforced composites under transverse tension and out-of-plane shear," *International Journal of Solids and Structures*, vol. 46, p. 2265–2274, 2009.
- [106] E. Totry, C. González and J. LLorca, "Prediction of the failure locus of C/PEEK composites under transverse compression and longitudinal shear through computational micromechanics," *Composites Science and Technology*, vol. 68, p. 3128–3136, 2008.
- [107] A. Melro, P. Camanho, F. A. Pires and S. Pinho, "Micromechanical analysis of polymer composites reinforced by unidirectional fibres: Part I – Constitutive modelling," *International Journal of Solids and Structures*, vol. 50, p. 1897–1905, 2013.

- [108] N. Tschoegl, "Failure surfaces in principal stress space," *Journal of Polymer Science, Part C: Polymer Symposia*, vol. 32, p. 239–267, 1971.
- [109] b. M. A. B. A. R. M. P. P. C. L. G. W. K. L. Xiaoming Bai a, "High-fidelity micro-scale modeling of the thermo-visco-plastic behavior of carbon fiber polymer matrix composites," *Composite Structures*, vol. 134, p. 132–141, 2015.
- [110] S. M. Lee, Reference Book for Composites Technology, Volume I, Lancaster: CRC Press, 1989.
- [111] HEXION, "Technical Data Sheet," Internal document, Duisburg, 2015.
- [112] C. Fais, "Lightweight automotive design with HP-RTM," *Reinforced Plastics*, pp. 29-31, 2011.
- [113] D. S. C. Luis F. Trimino, "Evaluation of Numerical Methods to Model Structural Adhesive Response and Failure in Tension and Shear Loading," *Journal of Dynamic Behavior of Materials*, pp. 122-137, 2016.
- [114] P. V. J. D. J. Peirs, "Novel Technique for Static and Dynamic Shear Testing," *Experimental Mechanics*, p. 729–741, 2012.
- [115] MatchID, "Model validation based on numerical deformation-Validate models & simulations," 2020. [Online]. Available: <http://www.matchid.eu/en/solutions/model-validation>. [Accessed 07 08 2020].
- [116] K. P. Menard and B. W. Bilyeu, Dynamic Mechanical Analysis of Polymers and Rubbers, John Wiley & Sons, 29 September 2008.
- [117] G. WISANRAKKIT and J. K. GILLHAM, "The Glass Transition Temperature (T_g) as an Index of Chemical Conversion for a High -T_g Amine/Epoxy System: Chemical and Diffusion-Controlled Reaction Kinetics," *Journal of Applied Polymer Science*, vol. Vol. 41, pp. 2885-2929, 199.
- [118] M. Semeliss, g. Wong and M. Turtle, "The Yield and Post-Yield Behavior High-Density Polyethylene," NASA-Langley Research Center Grant No. NAG-I-974, 1990.
- [119] R.-M. AC, Fractography and failure mechanics of polymers and composites, London: Elsevier Applied Science, 1989.

- [120] X. M. ·. J. C. ·. C. B. ·. T. Pardoen, "Mechanical characterization and modeling of the deformation and failure of the highly crosslinked RTM6 epoxy resin," *Mech Time-Depend Mater*, vol. 21, p. 419–454, 2017.
- [121] J. K. Dienes, "On the Analysis of Rotation and Stress Rate in Deforming Bodies," *Acta Mechanica*, vol. 32, p. 217–232, 1979.
- [122] B. McCleave, "Cracking Behaviour of Glass Fibre-Reinforced Polymers under Combined Compression-Shear Cyclic Loading," University of Waterloo, Waterloo, 2018.
- [123] P. Robinson, E. Greenhalgh and S. Pinho, *Failure Mechanisms in Polymer Matrix Composites: Criteria, Testing and Industrial Applications*, Cambridge: Woodhead Publishing, 2012.
- [124] J. Bergström, in *Mechanics of Solid Polymers-Theory and Computational Modeling*, Norwich, NY, William Andrew, 2015, p. 520.
- [125] LS-DYNA, "LS-DYNA supports," 2005. [Online]. Available: <https://www.dynasupport.com/tutorial/computational-plasticity/the-equations-for-isotropic-von-mises-plasticity>. [Accessed 06 03 2020].
- [126] Abaqus, "Abaqus verification guide," 2 April 2103. [Online]. Available: <http://dsk.ippt.pan.pl/docs/abaqus/v6.13/books/ver/default.htm>. [Accessed 10 03 2020].
- [127] George T. (Rusty) Gray III, "Classic Split-Hopkinson," in *ASM Handbook*, ASM International, 2000, p. p462–476.
- [128] C. R. Siviour and J. L. Jordan, "High Strain Rate Mechanics of Polymers: A Review," *Journal of Dynamic Behavior of Materials*, pp. 15-32, 2016.
- [129] DS SIMULIA, "Abaqus 6.14," 23 4 2014. [Online]. Available: <http://ivt-abaqusdoc.ivt.ntnu.no:2080/v6.14/books/usb/default.htm>. [Accessed 13 6 2020].
- [130] B. Fiedlera, M. Hojoa, S. Ochiaia, K. Schulteb and M. Andoc, "Failure behavior of an epoxy matrix under different kinds of static loading," *Composites Science and Technology*, no. 61, p. 1615–1624, 2001.

Appendices

Appendix A - DMA Test Setup

A.1 DMA Strain Sweep

Table A.1. Test parameters used for the strain sweep tests.

| Frequency (Hz) | Preload (N) | Amplitude | Number of amplitude point |
|----------------|-------------|-----------------------|---------------------------|
| 10 | 0.05 | 0 to 75 μm | 50 |

The protocol used for the strain sweep tests was:

- 1) Ramp up at a rate of 3 °C/min from ambient temperature to 35 °C
- 2) Equilibrate at 35 °C
- 3) Isothermal for 5 min
- 4) Amplitude ramp up from 0 to 75 μm logarithmically
- 5) End of cycle

A.2 DMA Temperature Sweep

Table A.2. Test parameters used for the temperature sweep tests.

| Frequency (Hz) | Preload (N) | Applied strain (%) | Temperature incensement (°C/min) | Temperature range (°C) |
|----------------|-------------|--------------------|----------------------------------|------------------------|
| 10 | 0.05 | 0.035 | 3 | 35 to 150 |

The protocol used for the temperature sweep tests was:

- 1) Ramp up at a rate of 3 °C/min from ambient temperature to 35 °C
- 2) Equilibrate at 35 °C
- 3) Isothermal for 5 min
- 4) Ramp 3.00 °C/min to 150 °C
- 5) Cool down
- 6) Equilibrate at 30 °C
- 7) End of cycle

Appendix B - T-PSHPB and C-PSHPB Calibrations

B.1 Static Bar-calibration for T-PSHPB and C-PSHPB

A static bar-calibration procedure was performed to determine the strain-voltage coefficients or strain calibration parameters, and the parameters would be used by the CHSB software to perform the post-process of the test data (Figure B.1).

The image shows two side-by-side panels for 'Incident Bar' and 'Transmitted Bar' calibration. Each panel contains the following fields:

- Calibration File:** C:\Users\y77zeng\Desktop\Plastic\Resin\SPTPB (with a 'Browse' button)
- Bar Name:** Acrylic Incident Dec 1 2017 Biocore Project (left) / Acrylic Transmitted Dec 2017 Biocore Project (right)
- Geometry:**
 - Diameter: 0.0254 m
 - Length: 2.4384 m
 - Gauge to Interface Distance: 1.301 m (left) / 1.331 m (right)
- Material Properties:**
 - Density: 1178 kg/m³
 - Elastic Modulus: 3470000000 N/m²
 - Poisson's Ratio: 0.38
- Strain Calibration Parameter:** Strain = -0.001541 V (left) / Strain = -0.001502 V (right). This field is highlighted with a red box.
- Appended Data:**
 - Propagation Coefficient Included:
 - Frequency Filter: 0 Hz

Figure B.1. An image of the CHSB software window showing calibration parameters

During a static calibration, static forces (ramp up from 0 to 500 N with 20 N increment) were applied to the incident bar or the transmitter bar (Figure B.2). A load cell (1,000-lbf capacity, OMEGA LC412-1k)

was attached to the calibrated bar to measure the applied forces, and a numeric digital panel mount meter (MROHHSG electro) displayed the force value. A Fluke voltage meter read the amplified voltage values coming from the strain gauge on the bars.

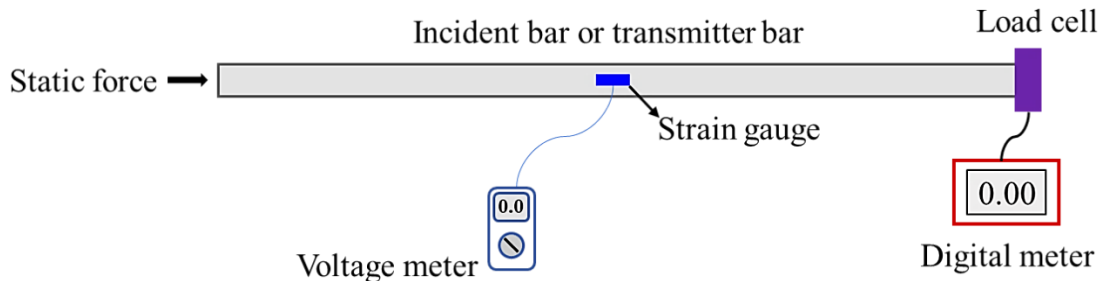


Figure B.2. A schematic diagram of the static bar-calibration.

The applied forces and the corresponding strain voltage were recorded for each increment. Then the strain-voltage coefficients of the T-PSHPB or C-PSHPB can be calculated from the calibration data. Normally, this coefficient should not change from test to test, but it would be better to double-check this value if the equipment is not in use for a while.

B.2 Dynamic Bar-calibration for T-PSHPB and C-PSHPB

A dynamic bar-calibration was performed to calculate the wave propagation coefficient. As discussed in Section 2.2.2, the CHSB software required the strain data on the specimen end to perform data post-process, but the T-PSHPB and C-PSHPB measured the strains or waveforms located in the middle of the incident or transmitter bars to avoid the signal-overlapping problem. Thus, it was required to shift the measured waveforms from the strain gauge location to the bar-specimen interface, and this process was performed in the CHSB software. To correct the wave disperse and attenuate during the shift, the CHSB software required dynamic calibration data to determine the wave propagation coefficient.

During a dynamic bar-calibration, a striker bar impacts the end of the incident bar or transmitter bar at the test velocity (another end of the bar free moving) (Figure B.3). A strain wave was generated by the impact, and the data acquisition system of the T-PSHPB and C-PSHPB apparatus recorded the amplified incident and reflected signals from the strain gauge. Then the CHSB software can calculate the wave propagation coefficient using the incident and reflected signals. Since the wave propagation coefficient was

related to the impact velocity, one dynamic calibration was normally required for each set of tests. Ideally, the forward propagated incident wave and the backward propagated reflected wave should be opposite with each other after both waves shift to the bar-specimen interface location (Figure B.4).

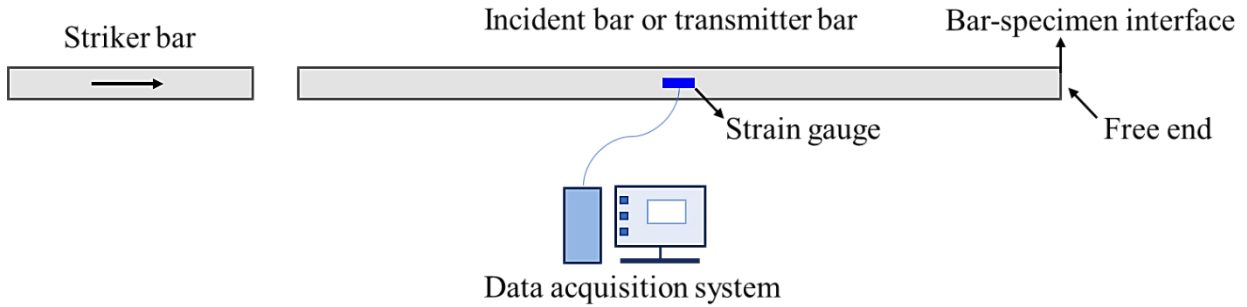


Figure B.3. A schematic diagram of the dynamic C-PHPB bar-calibration.

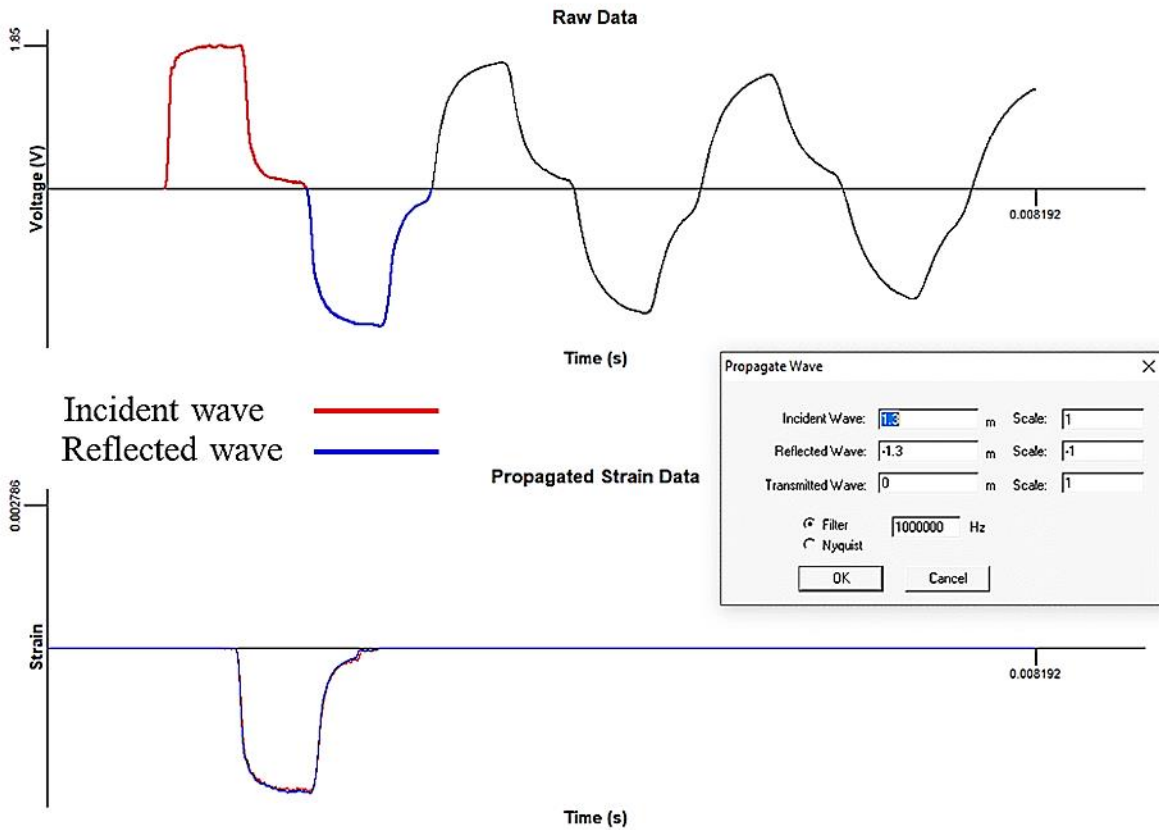


Figure B.4. Images of the CHSB software window showing the wave propagations

B.3 End-to-end Dynamic Calibration for C-PSHPB

After the dynamic bar-calibrations, an end-to-end dynamic calibration can be conducted for the C-PSHPB apparatus to verify the condition of the contact surfaces and alignment of the incident and transmitter bars, as well as the wave propagation coefficient. During the calibration, the incident bar and transmitter bar contacted end to end without the specimen, and the striker bar impacted the open end of the incident bar at the test velocity (Figure B.5). A strain wave was generated by the impact, and the data acquisition system of the C-PSHPB apparatus recorded the amplified incident and reflected signals from the strain gauge of the incident bar, as well as the transmitted signal from the strain gauge of the transmitter bar. Then the incident, reflected, and transmitted signals can be shifted to the contact location using the CHSB software with the calibrated wave propagation coefficient. With good bar alignment and surface contact, the majority of the impact wave propagated from the incident bar into the transmitter bar and can be recorded as a transmitted wave, while the reflected wave was minimal (Figure B.6).

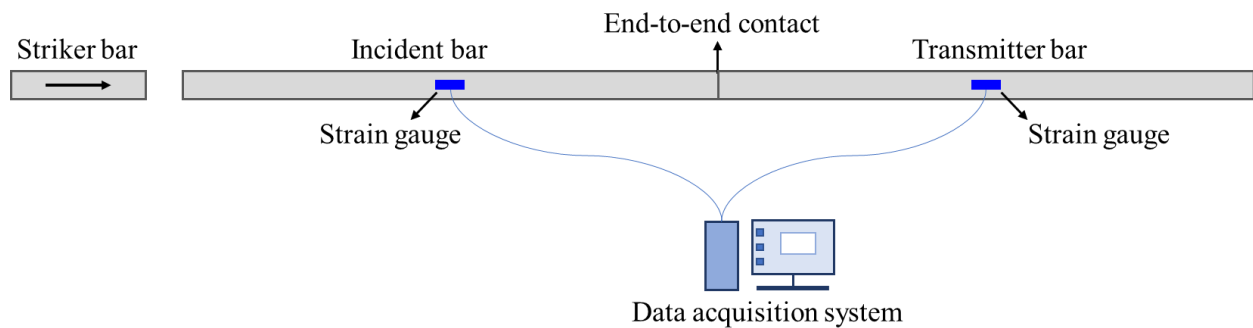


Figure B.5. A schematic diagram of the end-to-end dynamic calibration for the C-PSHPB apparatus.

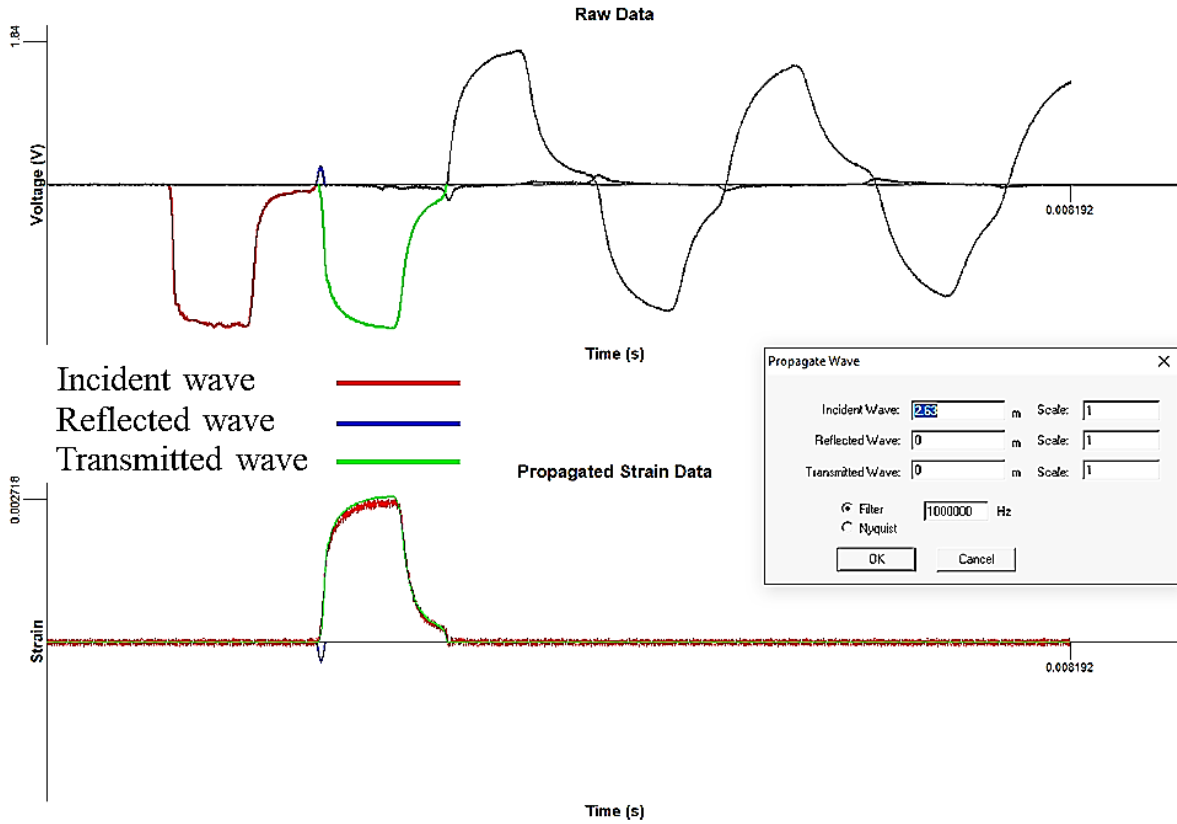


Figure B.6. Images of the CHSB software window showing the result of an end-to-end dynamic calibration